RESEARCH ARTICLE

# Main results of the third international PIV Challenge

M. Stanislas · K. Okamoto · C. J. Kähler ·
J. Westerweel · F. Scarano

**Abstract** This paper presents the main results of the third international PIV Challenge which took place in Pasadena (USA) on the 19th and 20th of September 2005. This workshop was linked to the PIV05 International Symposium held at the same place the same week. The present contribution states the objectives of the challenge, describes the test cases and the algorithms used by the participants, and presents the main results together with some discussion and conclusions on the accuracy and robustness of various PIV and PTV algorithms. As the entire amount of results obtained cannot be detailed, this contribution is written as a guide for the use of the full database of images and results which is available at http://www.pivChallenge.org.

M. Stanislas (✉)
Laboratoire de Mécanique de Lille, UMR 8107,
Cité Scientifique, 59655 Villeneuve d'Ascq Cedex, France
e-mail: pivnet-sig32@univ-lille1.fr
URL: www.pivChallenge.org

K. Okamoto
Department of Quantum Engineering Systems Science,
The University of Tokyo, 7-3-1 Hongo, Tokyo 113-8656, Japan

C. J. Kähler
Institut für Strömungsmechanik, TU Braunschweig,
Bienroder Weg 3, 38106 Braunschweig, Germany

J. Westerweel
Laboratory for Aero and Hydrodynamics,
Delft University of Technology, Leeghwaterstraat 21,
2628 CA Delft, The Netherlands

F. Scarano
Delft University of Technology,
Aerospace Engineering Department,
Kluyverweg 1, 2629 HS Delft, The Netherlands

## 1 Introduction

In September 2001, the first international PIV Challenge took place in Göttingen (Germany), linked to the PIV01 Symposium. This workshop, which was the result of several different cooperative projects, both in Europe and Japan, was a great success. A total of 15 different teams participated in the analysis and about 50 participants were present at the workshop to discuss the results. These results were synthesised by Stanislas et al. (2003) and are available on the Challenge website: http://www.pivChallenge.org. Two years later, in September 2003, due to the interest raised by the first edition, the second international PIV Challenge took place in Busan (Korea), linked to the PIV03 Symposium. This workshop was again a good success with 15 contributing teams around the world who did analyse the PIV image database proposed for the challenge and about 60 participants to the workshop. The main results and conclusions were again published by Stanislas et al. (2005) and are also available on the challenge web site. The main conclusions of this second workshop can be summarised as follows.

Compared to the first Challenge, the fact of providing series of images has made it possible to carry out a statistical analysis of the results, which increased the reliability of the conclusions with respect to the observations based on a single recording in the first Challenge.

From case A, based on real PIV images of a jet in stagnant surrounding, the largest relative differences could be appreciated only in regions of nearly stagnant flow, where the particle image displacement was approximately 0.1 pixels (px). It also came out that the PIV and PTV results—in a strict sense—did not comply with mass conservation according to the jet entrainment velocity, showing that there is still room for improvement of PIV

interrogation algorithms. Also, it was noted that no significant difference in PIV interrogation performance was evidenced between the 'standard' PIV interrogation algorithm (using multi-pass interrogation with discrete-offset window shifting and three-point Gaussian sub-pixel interpolation) and 'advanced' PIV interrogation algorithms, like image deformation and 'optical flow' methods. This was attributed to the fact that the particle images in Case A were rather small (about 1-px), so that the advantages of image deformation technique were counter-balanced by the image degradation associated to the interpolation of the images.

From case B, based on synthetic images of a turbulent channel flow, a detailed statistical characterisation was performed by comparison with DNS. Differences between the different algorithms were put in evident near the wall. For turbulence intensities, a clear advantage was shown by advanced algorithms using multi-grid, multi-pass and window (or image) deformation. Interestingly, the 'optical flow' technique did very well in regions of strong velocity gradient, but seems more sensitive to out-of-plane loss-of-correlation. Another clear point was that advanced algorithms are quite sensitive to the implementation and programming strategy. The results obtained on the turbulence spectrum were demonstrative of the fact that a lot can be gained on the assessment of turbulence by the use of ingenious algorithms. These results also clearly demonstrate that the PIV noise has the same characteristics as a white noise.

The PTV approach showed a clear advantage for the measurement in the very near wall region, since the displacement of individual particle images could be measured. However, the RMS error was relatively large because of the particle location error.

Finally, case C, based on a patchwork of different cameras, made the improvement brought by the state-of-the-art methods clearly visible. Since then, this test case was analysed in more detail by Hain et al. (2007).

Globally, most of the state-of-the-art methods were present and most of the commercially available PIV methods too. The global agreement between the different methods was quite good, but the differences that appear in some specific regions of the flow were significant and showed that certain algorithms perform better than others in the same regions. In particular, the noise level provided by the different algorithms is significantly different. Also, the advantage of the 'advanced algorithms', was clear on the synthetic images of case B in the region of strong gradient and in case C. It was not so obvious on the real images of case A. Unfortunately there was not a single algorithm that had the best performance everywhere.

The final conclusion of the workshop was that it was worth preparing a third Challenge, with test cases that allow a more advanced analysis of the spatial resolution of the algorithms and with the inclusion of stereoscopic PIV data in order to evaluate the different reconstruction techniques. This third Challenge is the purpose of the present paper.

On the European side this activity was supported by the PivNet 2 European network (Task 5) and the ERCOFTAC Special Interest Group on PIV (SIG 32), while on the Japanese side the activity was supported by the Japanese Standard Image Project of the Visualization Society of Japan.

## 2 Organisation

The third Challenge was organised following the same structure as the first two editions. A scientific committee was in charge to supervise the scientific aspects while a steering committee was in charge of the practical organisation. The scientific committee for this Challenge is given in Table 1, while the steering committee was composed of the authors of the present paper. The local organisation was taken in charge by the Caltech team of Pr. Gharib who is warmly acknowledged here for the kind and efficient support provided.

The Challenge web site (http://www.pivChallenge.org) was used for the distribution and collection of images and data. The Challenge was organised around five test cases,

**Table 1** Scientific committee of the PIV Challenge

| Name | Country | Address |
| --- | --- | --- |
| Pr T. Kobayashi | Japan | Institute of Industrial Science, University of Tokyo (Japan) |
| Pr Nishio | Japan | Kobe University of Mercantile Marine (Japan) |
| Pr K. Okamoto | Japan | University of Tokyo, Nuclear Eng. Res. Lab. (Japan) |
| Pr R.J. Adrian | USA | University of Illinois at Urbana Champaign, Theoretical and Applied Mechanics Laboratory (USA) |
| Dr C. Kähler | Europe | Technical University Braunschweig (Germany) |
| Pr J. Westerweel | Europe | Delft University of Technology, Laboratory for Aero and Hydrodynamics (The Netherlands) |
| Pr M. Stanislas | Europe | Laboratoire de Mécanique de Lille France |

which will be presented in detail below. The results from the contributors were presented and discussed during the Pasadena workshop on September 19th and 20th 2005. The aim was to undertake a detailed and quantitative comparison of the merits of the different evaluation algorithms and software that are available or under development at the contributors, to analyse single exposed PIV and PTV records.

### 2.1 Procedure

A database of PIV records was provided for analysis to the 'contributors'. All images in this database were single exposed and suitable for cross correlation analysis. They were provided in the TIFF image format as 'sets' of two images, referenced 1 and 2 for each exposure.

This database was organised in two packages. The full analysis of the first package was mandatory to be considered as a 'contributor' at the final workshop. The first package, devoted to the assessment of PIV algorithms accuracy and spatial resolution, together with time resolved PIV, was composed of 3 test cases that are given in Table 2. The second package, focussed on stereo PIV, contained two cases detailed in Table 3. The images were distributed on February the 28th 2005. All the results by contributors were due on April the 30th 2005.

The comparison of the results obtained by the different contributors was performed and presented at the workshop by the steering committee. Data were provided by the contributors as:

- the post-processed displacement fields,
- the coordinates at which the displacements are determined,
- a flag matrix giving the location of the points where no correlation was obtained and where spurious vectors were removed.

For the first package, all results were given in pixel units with the origin at the centre of the lower left corner pixel of the image (i.e. (0.5, 0.5) pixels from the lower left corner of the image). For the second package, calibration images were provided for stereo reconstruction and the results where provided in physical units.

## 3 Algorithms

A total of 23 contributors participated to the Challenge utilizing both PIV and PTV (see Table 4). Most participants were using PIV and the participants proposing PTV techniques had fairly different algorithms.

In order to be able to compare the different features of the evaluation methods applied to the analysis of the Challenge images, the main implementations will be

**Table 2** Test cases of first package of the second PIV Challenge

| Case no. | Description | Provider | Image type | Number of sets |
|---|---|---|---|---|
| A | Sets of images to check spatial resolution | Stanislas | Synthetic | A1(100), A2(100), A3(100), |
| | A1 to A3: 1,024 × 1,024 on 8 bits, tiff format with a 8 bytes header. | Scarano | | |
| | A4: 2,000 × 2,000 on 16 bits, tiff format with a 8 bytes header | Wieneke | | A4(1) |
| B | Time resolved PIV in a channel flow | Kähler | Synthetic | B(100) |
| | 1,440 × 688 on 8 bits, tiff format 164 bytes header | | | |
| C | Time resolved PIV in jet flow. | Okamoto | Real | C(100) |
| | 512 × 512 bmp format no header | | | |

**Table 3** Test cases of second package of the second PIV Challenge

| Case no. | Description | Provider | Image type | Number of sets |
|---|---|---|---|---|
| D | Stereo PIV accuracy assessment | Stanislas | Synthetic | D1(1),D1TCR(11), |
| | 1,024 × 1,024 on 8 bits, tiff format with 8 bytes header | | | D1TDT(11)D1C(10) |
| | | | | D2(1),D2TCR(11), |
| | | | | D2TDT(11),D2C(10) |
| | | | | D3(1),D3TCR(11), |
| | | | | D3TDT(11)D3C(10) |
| | | | | D4(1),D4TCR(11), |
| | | | | D4TDT(11),D4C(10) |
| E | Stereo PIV in a pipe flow | Westerweel | Real | E(100), ET(5) |

**Table 4** List of contributors

| Team acronym | Company and address | Contact name | PIV PTV |
|---|---|---|---|
| FOI | FOI, Bromma (Sweden) | K. Sjors | PIV |
| DUTAE | Delft University of Technology, Aerospace Engineering (Netherlands) | F. Scarano | PIV |
| PURDUE | Purdue University, West Lafayette (USA) | S. Wereley | PIV |
| | University of Mississippi, Oxford (USA) | L. Gui | |
| CORIA-LEA | CORIA UMR CNRS 6614 Rouen (France) | B. Lecordier | PIV |
| | LEA UMR CNRS 6609 Poitiers (France) | L. David | |
| URS 1-CIRA | University of Rome La Sapienza (Italy) | G.P. Romano | PIV |
| | CIRA, Capua (Italy) | F. De Gregorio | |
| URS 2 | University of Rome, La Sapienza (Italy) | M. Moroni | PTV |
| LAVIS | LaVision GmbH Göttingen (Germany) | B. Wieneke | PIV |
| VKI | Von Karman Institute, Rhode St Genese (Belgium) | M. Riethmuller R. Theunissen | PTV |
| OSAK | Osaka Sangyo University (Japan) | K. Ohmi | PTV |
| UDN | Universita di Napoli "Federico II" Napoli, Italy | G. Cardone T. Astarita | PIV |
| IOT | Institute of Thermophysics, Siberian Branch of RAS, Novosibirsk, Russia | D. M. Markovich | PIV |
| DLR | Institute of Propulsion Technology German Aerospace Center (DLR) Köln (Germany) | C. Willert | PIV |
| KMU | Division of Mechanical and Information Engineering, Korea Maritime University, Busan (Korea) | D.H. Doh | PTV |
| CLIPS-LIMSI | CLIPS-IMAG CNRS, Grenoble (France) | G. Quenot | OF |
| | LIMSI UPR CNRS 3251 Orsay (France) | F Lusseyrand | |
| CEMAGREF | CEMAGREF, Rennes (France) | J. Carlier | OF |
| TUDr | TU Darmstadt, Strömungslehre und Aerodynamik, Darmstadt (Germany) | H. Nobach | PIV |
| GPIV | Barcelona (Spain) | G. van der Graaf | |
| ILA | Intelligent Laser Applications GmbH, Juelich (Germany) | S. Kallweit | PIV |
| ESI | Energy Systems Institute, Russian Academy of Science, Irkutsk (Russia) | V. Zubtsov A. Mikheev | EPTV |
| YATS | YATS, Rome (Italy) | M. Miozzi | PTV |
| TSI | TSI Incorporated, Shoreview, MN (USA) | Wing T. Lai | PIV |
| TAMU | Department of Nuclear Engineering, Texas A&M University, Texas (USA) | Y. A. Hassan | PIV |

briefly described in the following section. For details the reader is addressed to the references listed at the end.

### 3.1 FOI

The team from FOI (Sweden) uses a MatLab-based evaluation program with a low-pass Gaussian filter for the images to eliminate high-frequency noise. The algorithm uses a multi-grid cross-correlation approach. A three-point Gaussian peak fit is used for the determination of the particle image displacement with sub-pixel accuracy. A specific validation algorithm has been designed. No publication is available on the FOI algorithm.

## 3.2 DUTAE

The evaluation program window deformation iterative multi-grid (WIDIM) primarily developed at VKI (Scarano and Riethmuller 2000) has been further improved since the previous Challenge (Stanislas et al. 2003) at Delft University of Technology, Aerospace Engineering Department (The Netherlands) (Scarano 2002). The first step included in WIDIM is an iterative multi-grid window deformation method. It allows a de-coupling between the spatial resolution and the dynamic range by using an iterative evaluation procedure with integrated window refinement. The refinement is possible as the in-plane loss-of pairs is compensated almost completely by means of local window shifting and deformation. The deformation is performed symmetrically with respect to the measurement position in order to obtain a second order accurate estimate of the particle image displacement. The image deformation technique is implemented to compensate for the loss-of-pairs due to in-plane velocity gradients. Image interpolation at sub-pixel positions is performed by the cardinal sine scheme function. The image deformation field is obtained by a linear interpolation of the velocity field. The data validation is performed with the normalized median test (Westerweel and Scarano 2005). For the stereo analysis, DUTAE uses a one-step dewarping and deformation procedure on the images, which at the same time allows to analyse the images at uniform magnification and avoids multiple interpolation (Scarano et al. 2005). Two positions of the calibration grid are used to compute the mapping functions. A disparity map is computed from one set of first exposures. The analysis of time correlated PIV data is mostly performed as a post-processing approach. After that a suitable time separation between exposures is chosen a second order polynomial regression is applied to the time resolved data.

## 3.3 Purdue

The software package EDPIV applied by Purdue University (USA) (Wereley and Gui 2002) can also be characterized as an iterative second order accurate central difference interrogation (CDIC), which supports continuous window shifting and image deformation methods. The evaluation time can be reduced by FFT acceleration techniques. The peak fitting is a standard three-point Gaussian fit. For difficult images, a $3 \times 3$ smoothing filter with an appropriately sized unsharp mask is used to form a band-pass filter eliminating both high and low frequency noise in the image. Four or five iterations are necessary to achieve an accurate evaluation with this method.

## 3.4 CORIA/LEA

Since the last Challenge (Stanislas et al. 2003), CORIA, at Rouen University (France), has developed a multi-grid, multi-pass iterative approach including a whole-symmetric image deformation method. The evaluation of velocity fields at each step of the deformation is based on FFT and includes a continuous window shifting technique (Lecordier and Trinité 2004). It is also possible to rotate the interrogation window in order to align it with the local velocity vector. For the peak fitting, a 2D Gaussian algorithm on a $3 \times 3$ points matrix is used. For the stereo processing, this team works with LEA at University of Poitiers (David et al. 2005), which uses a pin hole model with five calibration grid positions. The interrogation grid is back projected in the camera planes. The disparity map is computed on 50 sets of first exposures and allows to define iteratively the real equation of the measurement plane.

## 3.5 URS-1/CIRA

The software developed by University of Rome 'la Sapienza' together with CIRA (Italy) is a pyramid-based grid refinement (multigrid) method which implements advanced image processing and post-processing techniques for PIV using a standard FFT correlation algorithm (Marrazzo et al. 2004). Data post-processing is performed during iterations on each grid within the recursive window-offset procedure. Special emphasis has been placed on the enhancement of the number of tracer particles detected in two successive image pairs and of the spatial resolution of the method. To do this, sub-window image deformation using weight functions has been considered; sub-window weight function deformation would give results of a similar quality with much less computer time if compared with full image deformation (Di Florio et al. 2002). Concerning image post-processing, attention has been given to erroneous vector (outlier) detection and replacement. The outlier detection scheme used, based on a twelve point algorithm, combined with an horizontal and vertical spreading procedure all over the field (at least four points for validation) and with the iterative outlier replacement scheme based on a 25 point D-filter (Nogueira et al. 1997) gives the best solution and is suitable to many different image conditions.

## 3.6 URS-2

No information was provided on this software.

## 3.7 LAVIS

The LaVision Company (Germany) is using its standard commercial package available in version 7 of Davis and based on the method proposed by Scarano and Riethmuller (2000). This is a multi-pass algorithm with adaptive window deformation. Preprocessing based on filtering was applied to certain images. Cyclic FFT was used to compute the spatial correlation. The peak fitting algorithm is the standard three-point Gaussian fit. A local median filter was used to remove spurious vectors. For stereo processing, LaVision uses a pinhole model, with a simultaneous reconstruction and PIV processing. Five calibration grid positions are used to compute the pin hole model and the disparity map is computed on 100 sets of first exposure images.

## 3.8 VKI

In the von Karman Institute (Belgium) algorithm, the particle extraction is based on the intensity level threshold (Stitou and Riethmuller 2001). The threshold value is determined using the local intensity distribution. The particle tracking is again a hybrid of a cross-correlation and a tracking method. Initially the velocity distributions at grid points are calculated using the WIDIM cross-correlation method (Scarano and Riethmuller 2000). Based on the velocity at the interrogation grid, the particle matching is carried out. A double three-point Gaussian fit is used to determine the particle image positions. To reduce the probability of mismatching, each particle-image displacement is compared with those in its direct neighbourhood.

## 3.9 OSAK

The algorithm of Osaka University (Japan) is a so called pure particle tracking technique (Ohmi and Hang Yu 2000). They extract the particle location using an adaptive threshold technique in combination with low-pass filtering. Then, based on the particle-image location, they tracked the particle image using a so-called relaxation algorithm while taking into consideration the displacement magnitude and angle.

## 3.10 UDN

The University of Naples (Italy) has developed an algorithm based on a multi-grid iterative procedure with deformation of both images (Astarita and Cardone 2005;

Astarita 2006). The interpolation of the images is performed by using a high accuracy B-Spline interpolation scheme. Different weighting functions can be applied to the interrogation window and in the final iteration direct correlation is used to speed up the process. The peak in the cross-correlation map is interpolated by using a standard Gaussian fit over the nearest five points. A local median test is used to remove the outliers. The same settings (e.g. interrogation windows dimension), that enables to have a good spatial resolution, have been used for practically all the different challenge cases (some images of case B have been processed with more conservative settings).

## 3.11 IOT

The Institute of Thermophysics of Novosibirsk (Russia) used an in-house developed software package: 'Actual-Flow'. Multi-pass multi-grid approach with continuous window shifting and no window deformation was used in 2D2C algorithm. The peak fitting algorithm was the standard three-point Gaussian fit. Validation and smoothing of the predictor field between iterations were based on a $3 \times 3$ median and moving average filter respectively. Resample of a predictor field for multi-grid scheme was done by bilinear interpolation. Validation procedure was applied to the output vector field using $3 \times 3$ median or adaptive moving average filters. Calculation of 2D3C velocity fields was made using calibration based procedure with vector resampling scheme (Soloff et al. 1997). Calibration was performed with 3rd order polynomial mapping function for three positions of the calibration grid. Mapping function correction in the form of rotations and translation of a calibration target plane was done by iterative procedure with disparity map calculation over 10 pairs of first exposures.

## 3.12 DLR

Institute of Propulsion Technology of the Deutsches Zentrum für Luft, und Raumfahrt (Germany) used preprocessing based on high-pass filtering and/or dynamic histogram equalization (Willert 2004, 2006; Raffel et al. 2007). The algorithm was based on a multi-pass multi-grid method with image deformation inspired from that of the CORIA-1 algorithm. A special feature is the down-sampling of the image instead of using larger interrogation windows. This down-sampling is performed by summing up the intensities of neighbouring pixels. Interpolation is based on a cubic B-spline. The peak fitting is a 2D Gaussian fit on a $7 \times 7$ matrix. For stereo reconstruction, DLR uses an image mapping technique with a ratio of first order polynomials. Five calibration grid positions are used to compute the mapping functions. Disparity map is computed on one set of first exposures.

### 3.13 KMU

Korean Maritime University has developed a Gaussian masking algorithm for PIV. This algorithm is used used to enhance the accuracy of PIV calculation with sub-pixel resolution. Three types of sub-pixel interpolation methods can be used: Center, Parabolic and Gaussian. A genetic algorithm was also used for PTV (Doh et al. 2002). Notable fact is that spurious vectors were not eliminated in the results of SPIV. Namely, raw vectors were compared with others.

### 3.14 CLIPS/LIMSI

The algorithm used by CLIPS-IMAG in Grenoble (France) and LIMSI-CNRS in Orsay (France) is an orthogonal dynamic programming algorithm (ODP-PIV), developed by Quénot et al. (1998). It is based on the search of a transformation that relates the second image to the first by assuming that the intensity is conserved during the displacements and that the displacement of each image point (pixel) is small, rectilinear, uniform and continuous. In a hierarchical processing scheme the global image-to-image transformation is found by minimizing the L1 or L2 Minkowski distance between the images. After a successful evaluation, this method provides a displacement vector for each pixel. For stereo processing, CLIPS/LIMSI uses a pinhole camera model with a single calibration grid position. The algorithm allows recovering the grid misalignment with respect to the light sheet.

### 3.15 CEMAGREF/INRIA

The CEMAGREF of Rennes (France) is developing, together with the INRIA center of Rennes, a PIV algorithm based on Optical Flow. The proposed method is a novel optical flow method specifically dedicated to image sequences depicting fluid flow phenomena (Corpetti et al. 2002, 2006). It is based on the generic formulation proposed by Horn and Schunck (1981). To handle large displacements, the continuity equation is used in an integrated way. In the iterative process, this new form is linearised around the previous estimate and embedded with a multi resolution scheme. Various regularization parameters and penalty functions have to be set and optimized before analysis.

### 3.16 TUDr

To combine the benefits of correlation-based and whole-field methods, the Technical University of Darmstadt has developed a hybrid PIV method utilizing a densely sampled hypothetical velocity field. The hypothetical field is optimized in a multi-step correction loop, which utilizes the hypothetical velocity field for the image deformation and thereby derives a correction field. This method is of the multigrid multistep type with image deformation. One specificity is in the fact that for velocity interpolation, weighted averaging is performed considering the velocity and velocity gradient.

### 3.17 GPIV

This is an Open Source Software project issued under the GNU Public License and developed by G. Van der Graaf (http://www.gpiv.sourceforge.net). The software includes more than 40 command-line programs and scripts and a GTK/Gnome Graphic User Interface program. The code works on computers running the GNU/Linux Operating System on many different hardware platforms. For the Challenge, the interrogations were performed with: multi grid, multi pass, adaptive Interrogation Area dimensions and discrete zero-offsetting following the central differential scheme. After each pass, the estimators at the refined grid were obtained by bi-linear interpolation with shifted knots in order to improve accuracy and stability of the algorithm. Sub-pixel estimation has been performed with the three point Gaussian interpolation.

### 3.18 ILA

Intelligent Laser Applications GmbH is a well known company providing PIV equipment. The VidPIV processing software is internally developed since 1999. The cross correlation uses standard FFT-based algorithms to calculate the particle displacement. A symmetric phase only filtering (SPOF) can be used to increase the SNR (Wernet 2005). Linear or quadratic window deformation can be applied, together with subpixel window shifting by using B-Splines. The algorithm is multi pass and multi grid. Evaluation of stereo PIV images is done with polynomial mapping function. Typically two-level targets are used to generate the necessary z-shift of the calibration markers. The recombination of the two 2D displacement fields from the two camera planes uses a least square fitting. A disparity map is computed on one set of first exposures.

### 3.19 ESI

The Energy System Institute of Irkutsk (Russia) has developed a novel PTV technique which is a combination of three major quite independent components: Laplacian image filtering to detect individual particle images and theirs groups; a new algorithm, which relies on the accurate recovery of location, diameter and intensity provided by each individual tracer particle image spot in overlapping

environment; pairs matching based on tracer particle random size variety. The aim of this algorithm is to better cope with overlapping particle images in case of high tracer density.

## 3.20 Yet another tracking software (YATS)

It represents a time resolved correlation based tracking method (Miozzi 2004) solving the optical flow equation in a local framework (Lukas and Kanade 1981). The algorithm defines the best correlation measure as the minimum of the sum of squared differences (SSD) of pixels intensity corresponding to the same interrogation windows in two subsequent frames. After a linearization, the SSD minimization problem is iteratively solved in a least-square style, by adopting two different models of motion in consecutive steps. In the first step, a pure translational window motion is considered. In the second step, the scheme is refined by considering an affine window deformation, in which accurate image deformation parameters are given directly by the algorithm solution (Miozzi 2005). Velocity computation is then considered only where the solutions of the linear system corresponding to the minimization problem exist (i.e. where image intensity gradients are not null both in $x$ and $y$ directions: good features to track). This approach maximizes the signal-to-noise ratio and makes the algorithm able to investigate challenging flow conditions like wave-structure impacts (Lugni et al. 2006) and two-phase boundary layer flows. Moreover, in-plane loss-of-pairs is avoided by adopting a pyramidal image representation and sub-pixel image interpolation is performed adopting a bi-cubic scheme. Time resolved velocity and velocity gradients are obtained, in a lagrangian frame of reference, i.e. along each reconstructed trajectory. YATS algorithm is fully parallelized, both on shared and distributed memory, on win32 and Linux OS.

## 3.21 TSI

The TSI company (USA) used their standard commercial INSIGHT 3G software employing deformation grid, deformation spot mask, FFT correlation and Gaussian peak search. Background image subtraction was also employed for some test cases. The stereo reconstruction uses the Soloff technique. A disparity map can be computed and used to correct for grid misalignment.

## 3.22 TAMU

The Texas A&M University (USA) has developed a specific PTV algorithm with the following characteristics: particle identification is based on particle mask correlation and grey scale thresholds, particle centroid location is

achieved with sub pixel accuracy, path tracking of particles is achieved through correlation using the whole range of greyscales, multi-shaped regions with different image analysis parameters, easy to use interface.

It can be concluded that a wide variety of algorithms were presented, coming both from PIV providers and from leading PIV development teams. Among those, several algorithms, including multi-pass, multi-grid and image deformation methods, were present. In the present paper, following the current practice of the PIV community, these algorithms will globally be called 'advanced algorithms', although a more precise nomenclature would be useful (algorithms including window deformation techniques could be called second order as compared to first order window shifting techniques and 0th order correlation techniques without shift), it is beyond the scope of the present paper. Table 4 summarizes the main features of these algorithms together with some typical parameters used by the participants for the analysis of the Challenge images.

As far as PTV is concerned, the participation was not so numerous, although fairly different and complementary algorithms were represented. Table 4 summarises the PTV algorithms.

# 4 Case A

The aim of test case A was to try to assess the spatial resolution of the different PIV algorithms. Due to the development in complexity of the algorithms, it is often difficult to assess the real spatial resolution, looking just at the interrogation window size (when there is one, see optical flow techniques for example). Thanks to the speed of computers, PIV interrogation software can use all kind of filters inside the interrogation window (linear, Gaussian...). Moreover, most advanced algorithms use image deformation. All this makes the real spatial resolution difficult to quantify. Test cases A1–4 where designed for that purpose. Cases A1 to A3 where specifically designed by LML to investigate the spectral response of the algorithms. Case A4 was in fact proposed by two well known contributors to the PIV Challenge: F. Scarano and B. Wieneke. It was designed as a patchwork of small fields, each of which allowing to assess one aspect of the spatial resolution performances.

The synthetic PIV images for the three cases A1–3 were generated using the synthetic image generator (SIG) from the Europiv2 project (Lecordier and Westerweel 2004). The simulated recording configuration is shown in Fig. 1. The camera is looking at 90° to the light sheet plane. Particle images are $1{,}024 \times 1{,}024$ px on 8 bit. The parameters were selected to have good quality PIV images,
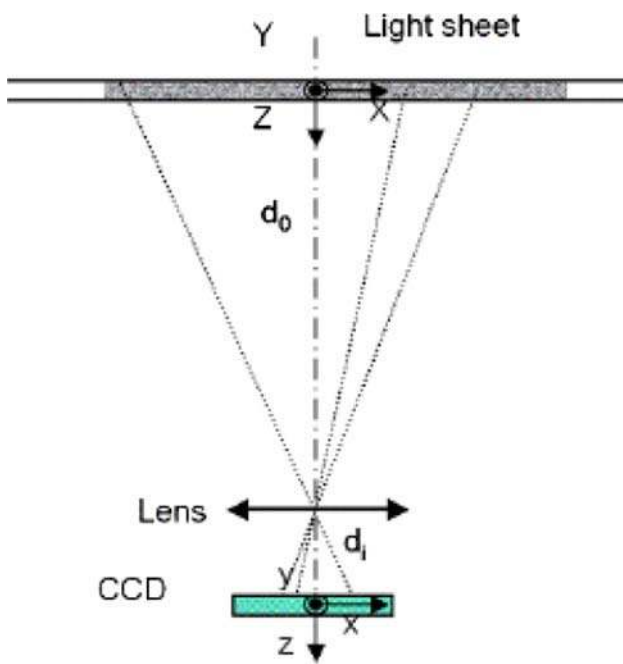
**Fig. 1** Recording set-up for cases A1 to A3

in order to assess the performances of the software itself. The particle image diameter is about 3 px and the particle density is about 0.16 particles/px (i.e. 40 particles in a window of 16 × 16 px) in cases A1 and A3, with a uniform random spatial distribution. This concentration was set quite high to allow the analysis down to about 8 × 8 px interrogation windows. For case A2, the concentration was increased to 0.32 particles/px, in order to resolve the small scales better. Figure 2 gives a representative example of image from case A1.

The velocity fields used to generate the particle displacements for cases A1, A2 and A3 are based on three different spectra shown in Fig. 3 and computed from regular grid numerical simulations. The simulation grid for
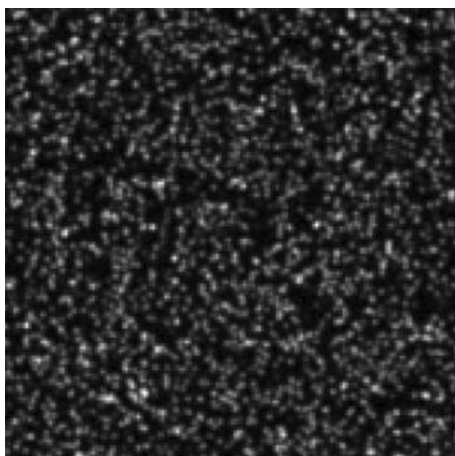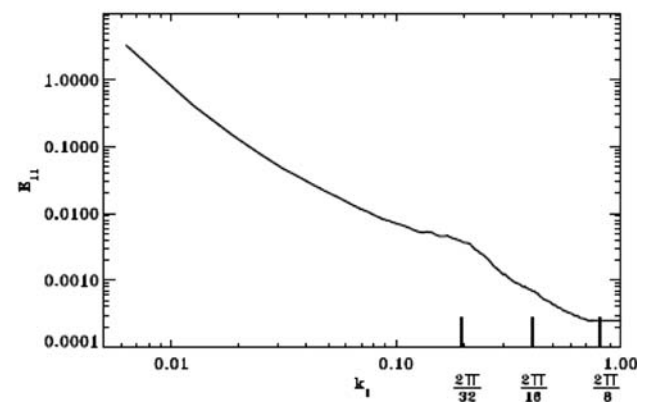


**Fig. 2** Sample of PIV image of 150 × 150 $px^2$ from case A1
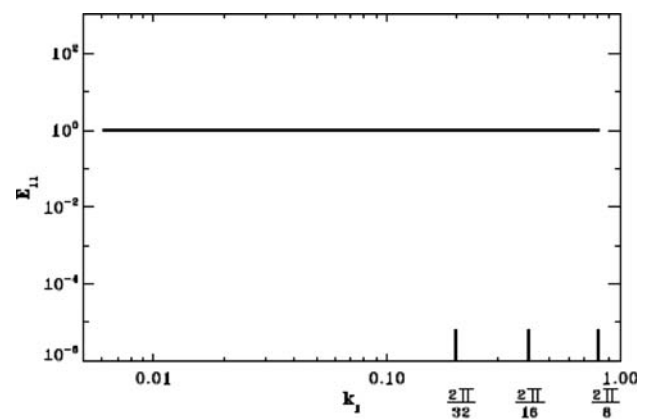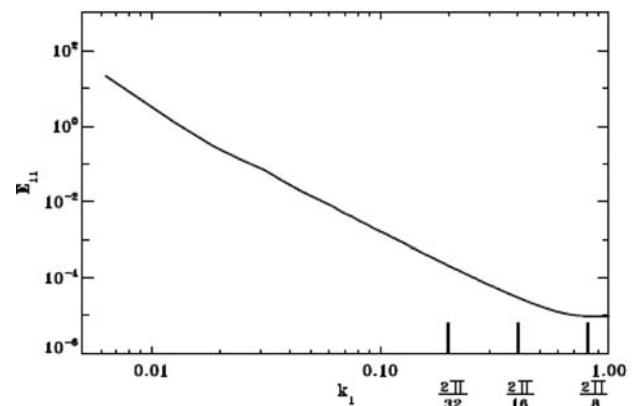


**Fig. 3** Spectrum of test cases **a** A1, **b** A2, **c** A3 as a function of the wave number in $px^{-1}$

cases A1 and A2 was 2,048 × 2,048 nodes and 768 × 768 nodes for case A2. The particles velocity was computed using a bilinear interpolation. Case A1 is a velocity field which spatial fluctuations have white noise structure that corresponds to a flat spectrum (Fig. 3a). Case A2 is a synthetic turbulence with a spectrum showing a strong

slope of about −3 (Fig. 3b). Case A3 is extracted from a stratified turbulent flow from a Direct Numerical Simulation. It shows an almost linear spectrum, with a small bump at the high frequency end (Fig. 3c). In all cases, spectra are nearly the same in the $x$ and $y$ directions.

In order to perform a quantitative comparison, for each case (A1 to A3), tables were assembled giving the mean and RMS values of the signal from the reference DNS and from the contributors (Tables 5, 6, 7). The bias and the RMS errors with respect to the DNS solution are also provided in these tables (both absolute and relative values for RMS). Besides, spectra and probability density function (PDF) of the $u'$ velocity component (representative also the behaviour of $v'$) are plotted for each case.

Special computations were performed for PDF graphs for GPIV in case A1 and OSAK in cases A2 and A3. In these cases, the initial PDF is a dense comb due to the fact that the data were rounded off, so it does hide the other curves on the graph. The comb has been removed. The PDF absolute value has then no meaning for these contributors.

**Table 5** Parameters for the analysis of Cases A1

| PIVc05 group | Participant | | Analysis | | | |
|---|---|---|---|---|---|---|
| | No. | Team acronym | Type | Window size (px) | Grid size (px) | Evaluation algorithm |
| 1 | 15 | CEM-IN | OF | | 1 | Multi-grid |
| 1 | 14 | CLI-LI | OF | 8 | 4 | Multi-pass with adaptative window sizing |
| 1 | 4 | CORIA | PIV | 16 | 8 | Multi-pass with adaptative window deformation |
| 1 | 12 | DLR | PIV | 16 | 4 | Multi-grid with adaptative image deformation |
| 1 | 2 | DUTAE | PIV | 15 | 4 | Multi-pass with adaptative window deformation |
| 2 | 1 | FOI | PIV | 16 | 6 | Single pass |
| 2 | 17 | GPIV | PIV | 8 | 4 | Multi-pass with adaptative window sizing |
| 2 | 18 | ILA | PIV | 16 | 8 | Multi-pass with adaptative image deformation |
| 2 | 11 | IOT | PIV | 16 | 4 | Multi-grid |
| 2 | 13 | KMU1 | PIV | 35 | X | Single pass |
| 2 | 7 | LAVIS | PIV | 16 | 4 | Multi-pass with adaptative image deformation |
| 3 | 3 | PURDUE | PIV | 24 | 12 | Multi-pass with adaptative window deformation |
| 3 | 21 | TSI | PIV | 32 | 8 | Multi-pass with adaptative image deformation |
| 3 | 16 | TUDr | PIV | 16 | 16 | Multi-pass with individual pixel shifting |
| 3 | 10 | UDN | PIV | 32 | 4 | Multi-pass with adaptative image deformation |
| 3 | 5 | URS1 | PIV | 32 | 16 | Multi-grid |
| | | | Mean number of particles per image | | | |
| 4 | 19 | ESI | PTV | 21 k | | Laplacian particle localization; displacement, size and angle |
| 4 | 9 | OSAK | PTV | 18 k | | Gaussian matched filter and dynamic threshold binarization; displacement |
| 4 | 22 | TAMU | PTV | 50 k | | threshold and average removal;correlation |
| 4 | 6 | URS2 | PTV | 5 k | | gaussian filter; intensity gradients |
| 4 | 8 | VKI | PTV | 58 k | | none displacement |
| 4 | 20 | YA-IN | PTV | 59 k | | optical flow based feature tracking |

**Table 6** Interpolation window size used for the PTV contributors

| Participant | A1 | | | A2 | | | A3 | | |
|---|---|---|---|---|---|---|---|---|---|
| | Grid size | Window size | Mean num. part./ window | Grid size | Window size | Mean num. part./ window | Grid size | Window size | Mean num. part./ window |
| ESI | 16 | 32 | 21 | 32 | 64 | 59 | 12 | 24 | 22 |
| OSAK | 16 | 32 | 18 | 8 | 16 | 10 | 12 | 24 | 22 |
| TAMU | 8 | 16 | 12 | 8 | 16 | 14 | 8 | 16 | 14 |
| URS2 | 32 | 64 | 20 | 16 | 64 | 51 | 32 | 64 | 55 |
| VKI | 8 | 16 | 14 | 8 | 16 | 15 | 8 | 16 | 14 |
| YA-IN | 8 | 16 | 14 | 8 | 16 | 14 | 8 | 16 | 14 |

**Table 7** Reference spatial resolution used for each contributor for Case A1 (grid spacing)

| Contributor | Spatial resolution (px$^2$) | Contributor | Spatial resolution (px$^2$) |
|---|---|---|---|
| CEM-INS | 1 × 1 | PURDUE | 12 × 12 |
| CLI-LI | 4 × 4 | TSI | 8 × 8 |
| CORIA | 8 × 8 | TUDr | 16 × 16 |
| DLR | 4 × 4 | UDN | 4 × 4 |
| DUTAE | 4 × 4 | URS1 | 16 × 16 |
| FOI | 6 × 6 | ESI | 32 × 32 |
| GPIV | 4 × 4 | OSAK | 32 × 32 |
| ILA | 8 × 8 | TAMU | 16 × 16 |
| IOT | 4 × 4 | URS2 | 64 × 64 |
| KMU1 | 12 × 12 | VKI | 16 × 16 |
| LAVIS | 4 × 4 | YA-IN | 16 × 16 |

For case A4, set-up by Scarano and Wieneke, a single image test case was built, with the objective of assessing interrogation algorithms performances in different situation in one shot. This compact benchmark case was designed

for the quantitative determination of the spatial resolution of evaluation methods. The particle image displacement field is based on one-dimensional sinusoids, two-dimensional sinusoids and parallel flow in proximity of solid walls. Several wavelengths are present. The first two cases allow drawing conclusions on the spatial frequency response of the interrogation algorithm by means of the cut-off spatial frequency. The last case is introduced to evaluate the well-known problem of velocity measurements close to solid walls, which is often attempted in order to evaluate the surface flow properties, the shear stress in particular.

The image used, which is shown in Fig. 4, includes four different test cases:

1. *Boundary layers* On the upper-left 1,000 × 1,000 corner the displacement relative to parallel wall flow is proposed. The flow exhibits the maximum gradient at the wall. Six different values of the thickness parameter are chosen from the very small value of 2 px to the rather affordable value of 40 px. The flow direction is inclined with respect to the image system



**Fig. 4** Synthetic generated image (two exposures superimposed)
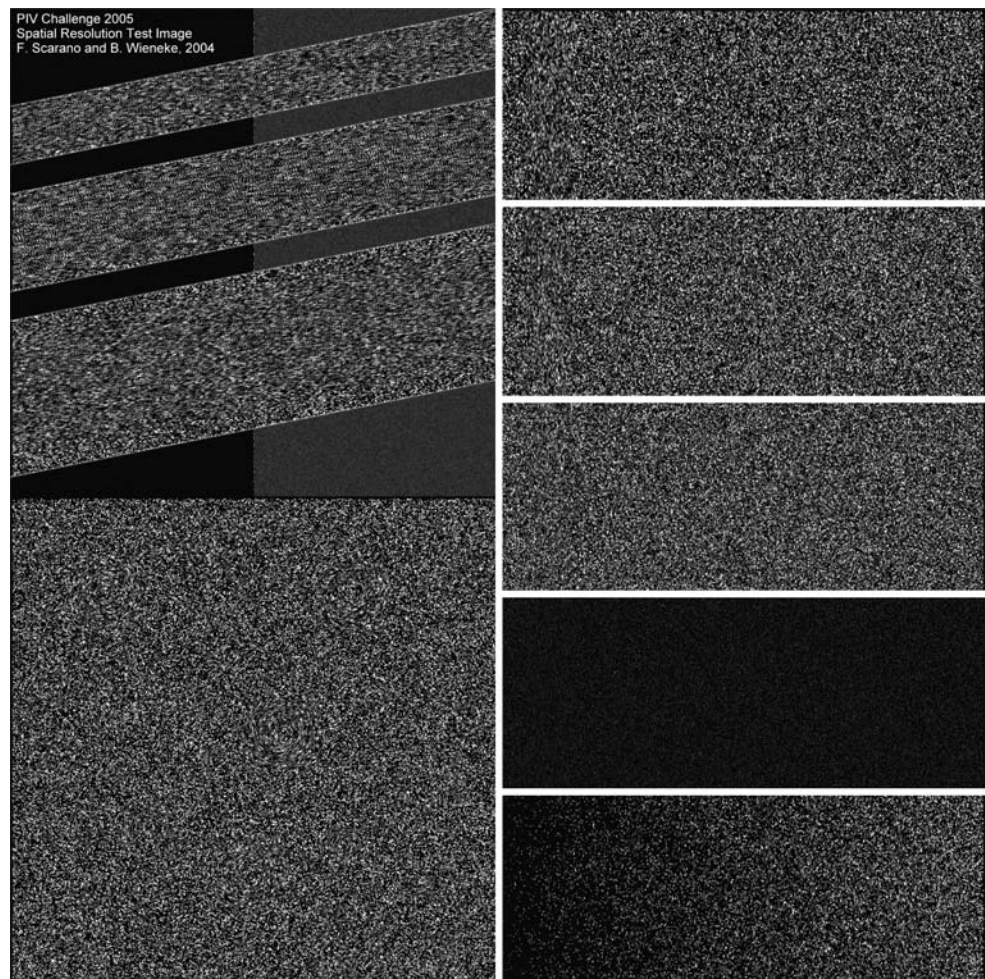
of coordinates, which represents a general situation encountered in wall flow around moderately curved walls. The region outside of the channels has a fixed pattern on the right hand side and no pattern on the left hand side. The sidewalls have a thin bright line of approximately 4 px.

2.  *Two-dimensional sinusoidal fluctuations* The lower-left 1,000 × 1,000 part of the image presents a set of random two-dimensional sinusoidal vortices. The sinusoids have different wavelength varying from 8 to 200 px. The amplitude varies around 2 px.

3.  *Modulated sinusoid test* The right 1,000 × 1,600 side is made of five regions of one-dimensional sinusoidal shear displacement. The sinusoidal displacement has a varying wavelength from 10 to 400 px. Each region of 1,000 × 400 px has slightly different values of the sinusoidal amplitude and the image properties are changed in terms of uncorrelated particles, background noise and particle image diameter. The sinusoids amplitude varies around 2 px.

4.  *Sinusoid with spatially varying seeding density* The bottom right 1,000 × 400 side is a one-dimensional sinusoidal shear displacement. The sinusoidal displacement has a fixed wavelength and slightly varying amplitude. The particle seeding density is varying from 0.1 particles-per-px to zero.

Figure 4 shows the test case image with the different windows corresponding to the above velocity fields and Fig. 5 the corresponding displacement fields. Table 8 summarizes the image properties and Table 9 the displacement field properties of the different parts of the image.
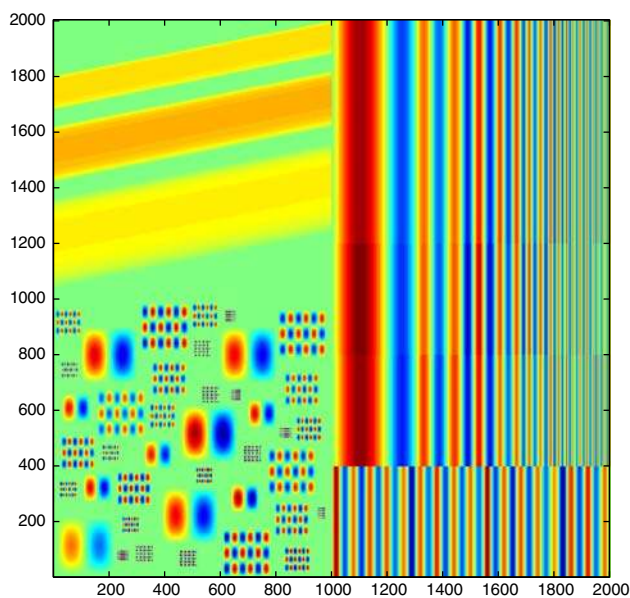


**Fig. 5** Displacement field, *V*-component

## 4.1 Case A1

This test case is particularly difficult as fluctuations of comparable amplitude exist at all scales. It was expected to clearly show the filtering effect of PIV, as a flat spectrum is the Fourier transform of a Dirac. To illustrate this, Fig. 6 shows the PDF of the original DNS signal compared to the same signal filtered with interrogation windows of increasing size. As can be seen, already an 8 × 8 interrogation window modifies significantly the PDF. This function is thus fairly sensitive to the variation of the window size. Hopefully, this is an extreme case, not representative of a real flow situation where one can expect that the amplitude of the fluctuations decrease with the length scale, due to the favourable effect of viscosity.

Table 5 summarises the main characteristics of the algorithms used by the different contributors for case A1. To make the figures more readable, the contributors were organized in 4 groups. Groups 1 to 3 include PIV and optical flow algorithms. Group 4 gathers the PTV algorithms and YATS which is an optical flow algorithm.

Concerning the spectra, there is a problem with the PTV data which are randomly distributed. As one aim of this challenge was to try to quantitatively compare PIV and PTV, it was decided to interpolate the PTV data on a regular grid to be able to compute the power spectrum. In order to assess the effect of this interpolation, different interpolators were compared:

*   Closest: taking the value of the PTV data closest to the grid node,
*   Mean: averaging values from the data that are inside a node centered window,
*   Krig 2D: interpolation using Krig algorithm inside a node centered window.

In the last two cases, the size of window was chosen as a function of the data density (30 vectors per window on average). Figure 7 gives, for case A1, the comparison of the PDF obtained directly from the PTV data and from the data processed with these three interpolators. Based on this comparison, the final choice was the Krig 2D interpolator. It was used for all PTV contributors and for cases A1–3. Only the size of the window was adapted to the density of the data provided by the contributors in order to keep 30 vectors per window on average. The window size used for the different cases is given in Table 6.

Figure 8 gives the power spectra obtained by each contributor, normalized by a 'reference' spectra on the same grid (black line). The size of the grid used is given in Table 7 for each contributor. The 'reference' solution is the exact solution averaged on a window twice the grid separation, corresponding to an overlap of 50%. As expected, the PIV algorithms show a windowing effect in the form of

**Table 8** Image properties

| Region | Seeding density (ppp) | Particle image diameter (px) | px noise (%) | Unpaired particles (%) |
|---|---|---|---|---|
| Boundary layers | 0.1 | 2.0 | 3 | 10 |
| 2-D sinusoids | 0.1 | 2.0 | 3 | 10 |
| 1-D sinusoids I | 0.1 | 2.0 | 0 | 0 |
| 1-D sinusoids II | 0.1 | 2.0 | 3 | 20 |
| 1-D sinusoids III | 0.1 | 2.0 | 3 | 60 |
| 1-D sinusoids IV | 0.1 | 0.6 | 3 | 10 |
| 1-D sinusoids V | 0.0 to >0.1 | 2.0 | 3 | 10 |

**Table 9** Displacement properties

| Region | Wavelength $\Lambda$ (px) | Amplitude (px) | Noise (%) |
|---|---|---|---|
| Boundary layers | 2,4,8,12,24,40 | 3–4 | 0 |
| 2-D sinusoids | 8,12,20,30,40,56,100,200 | 2–2.5 | 0 |
| 1-D sinusoids I | 20,24,28,40,60,80,110,200,400 | 2–3 | 0 |
| 1-D sinusoids II | 20,24,28,40,60,80,110,200,400 | 2–3 | 0 |
| 1-D sinusoids III | 20,24,28,40,60,80,110,200,400 | 2–3 | 0 |
| 1-D sinusoids IV | 20,24,28,40,60,80,110,200,400 | 2–3 | 0 |
| 1-D sinusoids V | 60 | 1.5–3 | 0 |
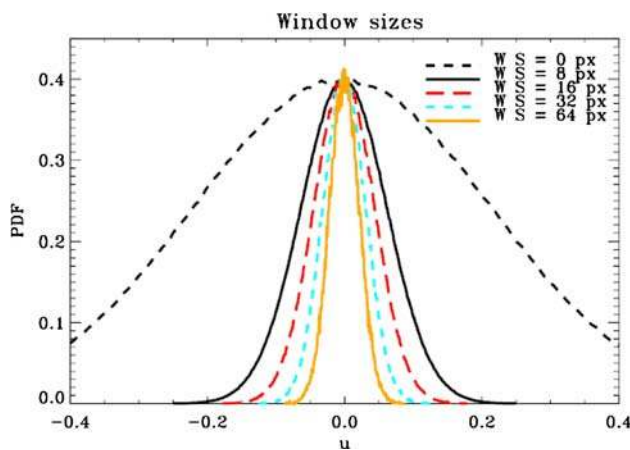


**Fig. 6** Reference pdf of case A1 filtered with windows of different sizes

a sinc function, visible on the high frequency (small scales) side. There are significant differences between the different algorithms (compare for example TSI and UDN). These differences are difficult to interpret just as they stand. It would be of interest to look at the correlation peak shape in this test case and to see how the contributors did the peak fitting. As it is expected that the PIV error is a white noise, the contribution of the signal and of the noise to the spectra cannot be extracted from Fig. 6. In Fig. 9, the spectra of the error (difference between the contributor's solution and the 'reference' solution) is provided. This error spectra is also normalized by the 'reference' solution spectra. In fact, as the different contributors come to different spatial resolution, plotting directly the error spectra on the same graph would make the comparison difficult. Using the proposed normalization brings all error spectra in the same range. One must keep in mind the difference in 'reference' spectra, due to the filtering, which is illustrated in Fig. 10. The level of the spectra increase with increasing the size of the interrogation window. To be complete, Table 7 gives the reference spatial resolution used by the organizers to compute the reference spectrum. The analysis of Figs. 8, 9 and 10 is fairly instructive. First of all, it is clear in Fig. 10 that, as the energy of the original signal is equally distributed over all frequencies, the filtering effect has a significant effect on the level of the spectrum. Consequently, differences in the level of the flat part of the spectrum in Fig. 9 are indicative of differences between real and estimated spatial resolution Now, the comparison of Figs. 8 and 9 clearly shows that all the algorithms introduce a fairly high random noise (even at the lowest frequencies) which increases with frequency and becomes comparable to the signal around the interrogation window size. Most PIV algorithms show the same trend (although with different levels). For TUDr, the spatial resolution is slightly overestimated. FOI is the only PIV algorithm to show a strange behaviour, which is difficult to explain without knowing the package used in more detail. For PTV, two groups of contributors can be distinguished: ESI and URS2, which show a flat error spectrum and the others for which the error spectrum behaviour is comparable to that of PIV. Globally, the spatial resolution has been slightly overestimated for PTV. It is also probable that the PTV algorithms are affected by the high particle image density and the comparable intensity of fluctuations at all
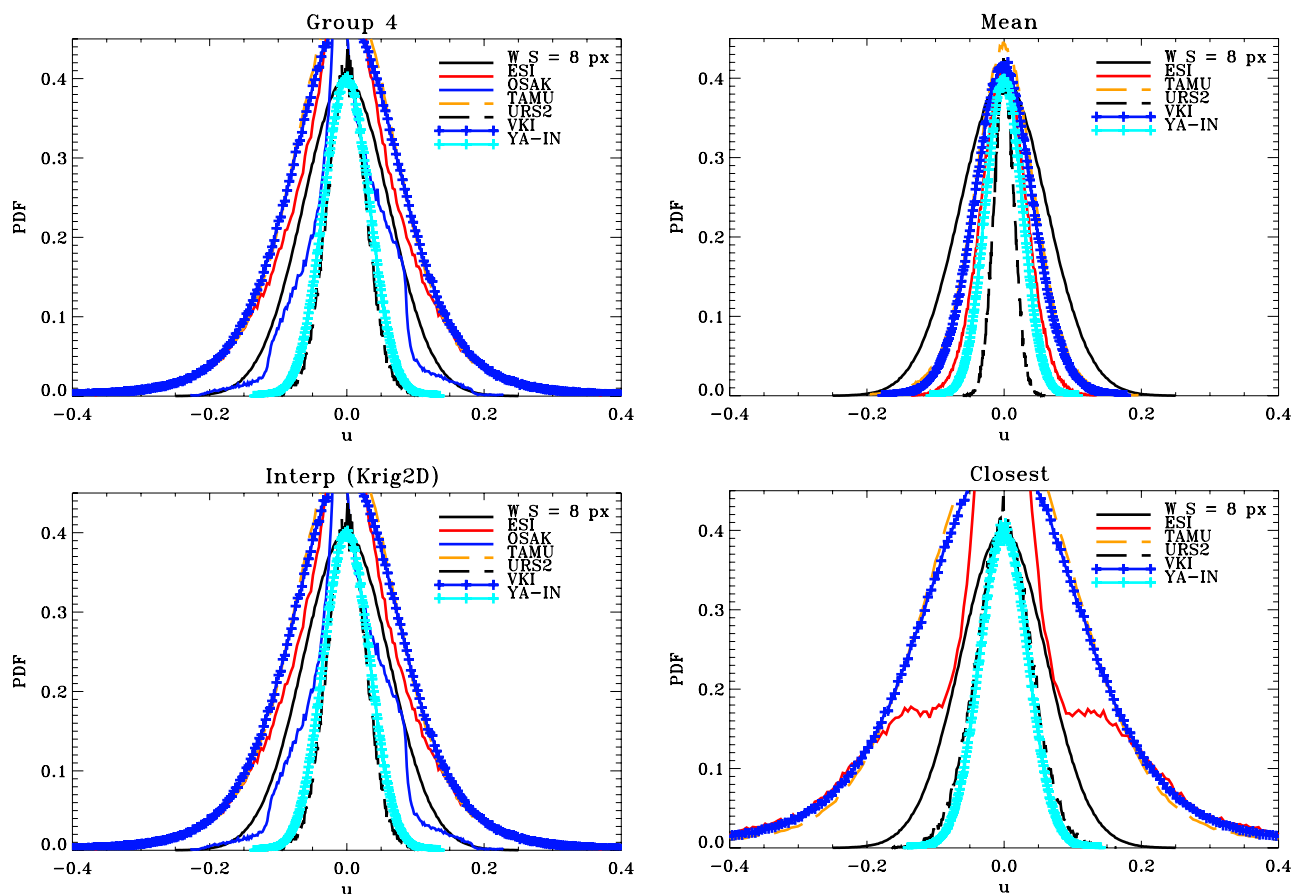
**Fig. 7** Effect of the interpolation scheme on the PDF in case of PTV. **a** Direct pdf of the PTV measurement, **b** pdf of the PTV data interpolated in the PIV grid using Krig2D, **c** pdf of the PTV data averaged on a window centered on the grid point, **d** pdf of the PTV data closest to the PIV grid point

scales which make the neighbourhood algorithms difficult to apply reliably.

To complement the spectral analysis, Fig. 11 gives the PDF of the data provided by the contributors. As a reference, the pdf of the reference solution, filtered with an 8 × 8 window is also plotted in this figure. These results should not be interpreted without looking carefully at the spectrum of Figs. 8 and 9. First of all, it is clear that most algorithms show a spatial resolution which is at best 16 × 16 px (see Fig. 6). The 8 × 8 resolution obtained by UDN looks fairly reliable and the best of the PIV algorithms. The optical flow method used by CEM-IN seems to do a bit better than 8 × 8 based on the PDF. Looking at the spectra, this result is difficult to trust and would need a deeper analysis of the data and of the algorithm to be really conclusive.

Finally, Table 10 gives the mean and RMS velocities averaged over the field and the number of samples, together with the bias and RMS error obtained by comparison with the reference solution and computed also over the field and number of samples. It should be noted that for some teams, it was necessary to remove one line or column

near the border which was containing obvious spurious values. As can be seen, although this test case is in some way very noisy, the mean value of the velocity comes out fairly well. This is a good point for the robustness of the technique as far as the mean flow is concerned. The results are not so favourable for the RMS. Strong differences appear between the contributors. Looking at the results from UDN, which appeared as the best for this test case, the RMS is comparable to the reference solution filtered on a 8 × 8 window (which is the spatial resolution inferred for this team), but the RMS error is of the order of 100%! Hopefully, this test case is not representative of real turbulence where, even if there are fluctuations inside the interrogation window, they are of smaller and smaller amplitude as their spatial scale decrease and they are not fully random.

### 4.2 Case A2

As a difference to case A1, it was tried here to generate a turbulent field with a spectrum showing a strong slope (near to −3) in order to assess the ability of the different
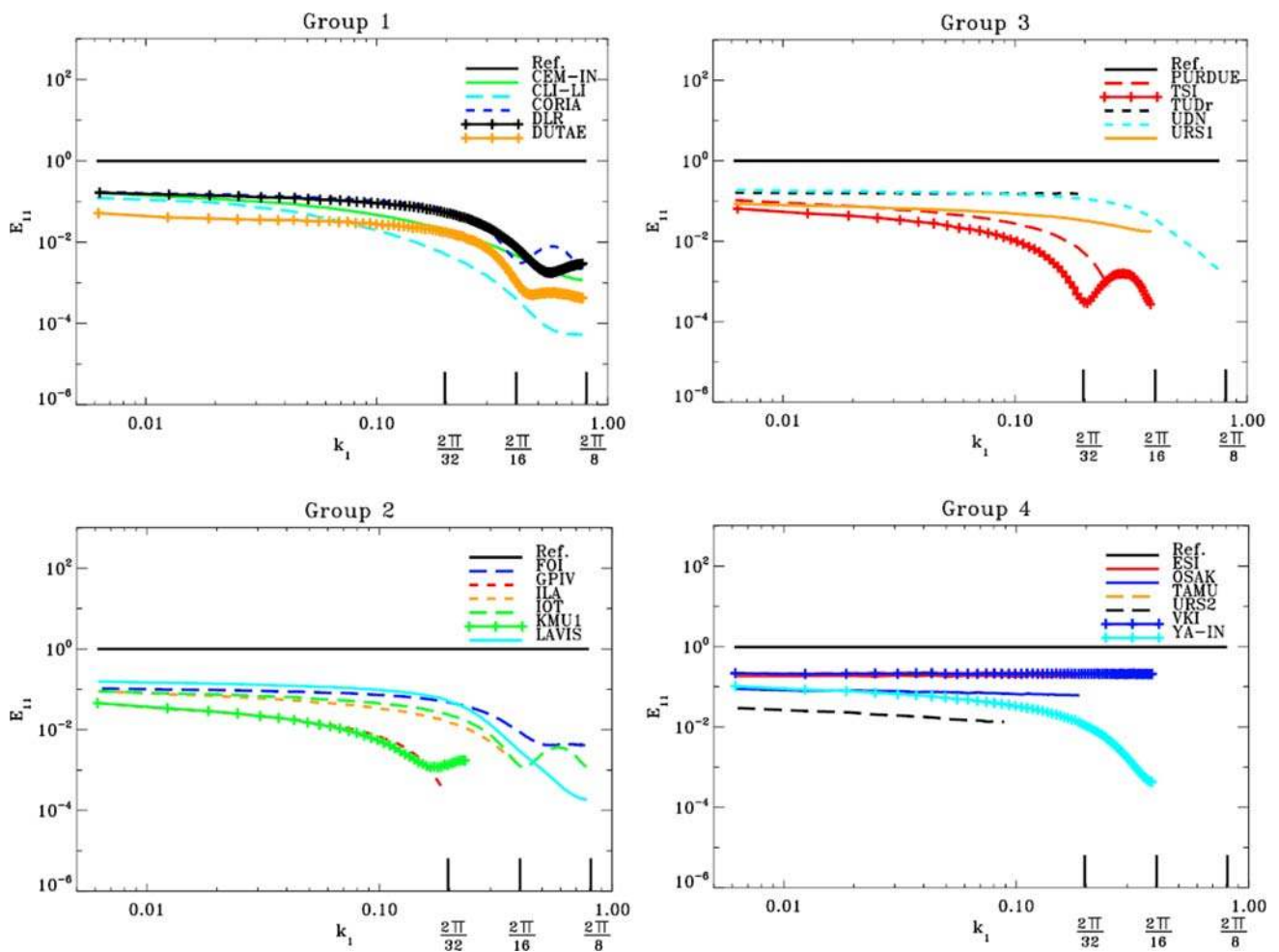
**Fig. 8** Case A1: Power spectrum on the $u'$ component compared to the reference spectrum for the four groups of contributors

algorithms to resolve fluctuations small both in size and intensity.

The analysis parameters provided by the contributors are the same as for case A1 (Table 5), except for Purdue who did not provide the information.

Figure 12 gives the spectra obtained by the contributors, compared to the reference spectrum. Here, no filtering of the reference spectrum and no normalization of the contributor's spectra is needed. The data clearly point out the differences between the algorithms. It is of particular interest to compare the real spatial resolution (when the spectrum separates from the exact solution) with the expected spatial resolution (the wave number corresponding to the right end of each spectrum. Comparing for example DLR and CLI-LI, both expect a spatial resolution of $8 \times 8$ px. DLR reaches $16 \times 16$ while CLI-LI is around 160! In fact, all PIV algorithms show a spatial resolution smaller than the grid spacing. It should be noted that several of them have used more than 50% windows overlap. Globally, the advanced PIV algorithms perform better than

the standard ones (compare GPIV with TSI for example). For these advanced algorithms, the high frequency noise filtering seems to be an important issue (compare DLR with UDN or Lavision for example). As far as optical flow is concerned, a strong difference appears between the two contributors (CLI-LI and CEM-IN). The best of them compares favourably with some advanced PIV algorithms, but the shape of the spectrum is difficult to explain without further tests and a deep insight in the theory of the method. For PTV, globally the spatial resolution is comparable to the less advanced PIV algorithms, although significant differences can be observed between the different teams.

As for case A1, the spectrum of the error (difference between the contributor's results and the exact solution) are plotted in Fig. 13. Here also, no normalisation was needed. First of all, the overall level of this error compared to the signal (Fig. 12) should be noted. This should be done keeping in mind that these are synthetic images of high quality. Most of the results support the conclusions of Fig. 12. The PTV error is higher than the PIV one. It is
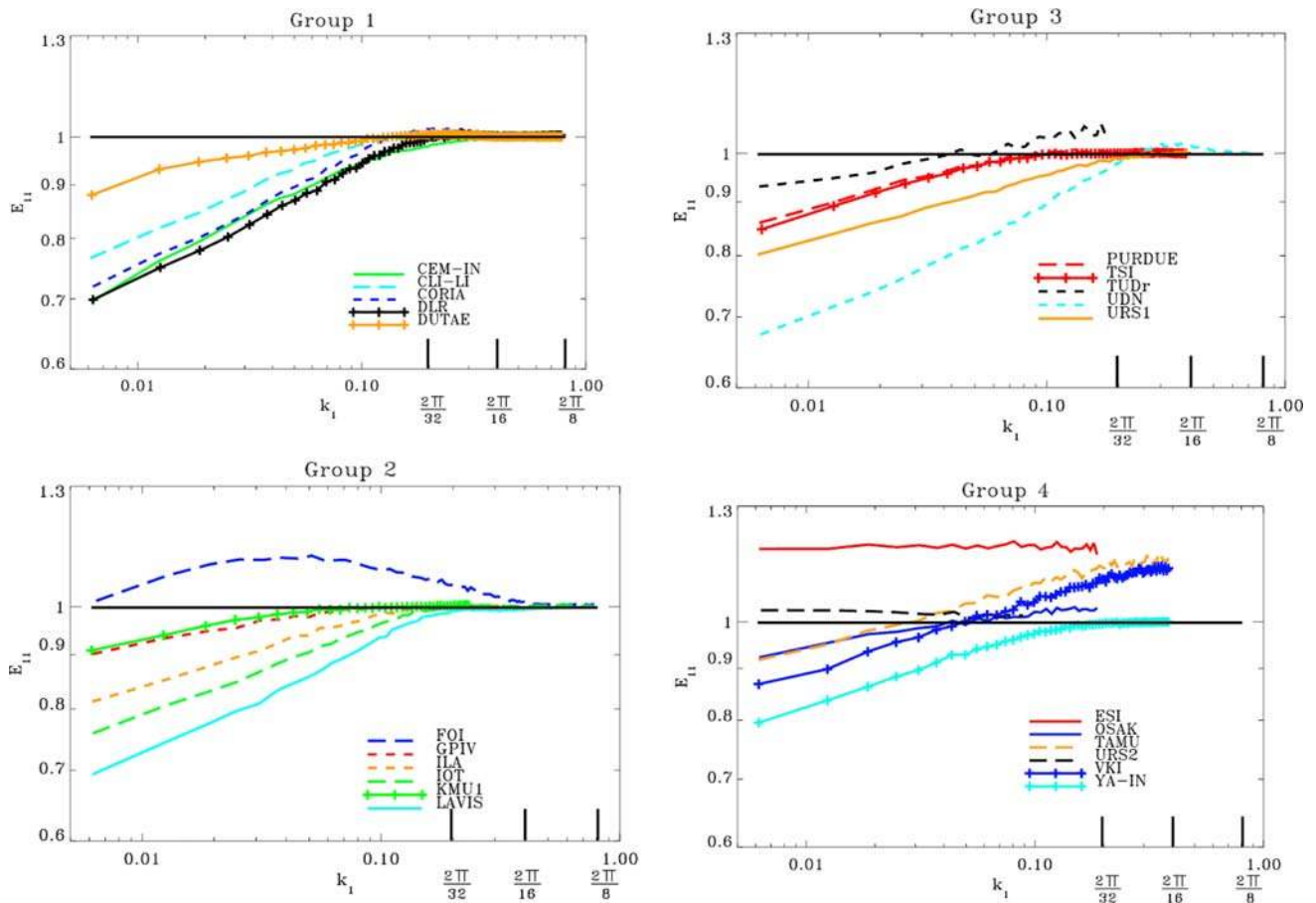
**Fig. 9** Case A1: Power spectrum of the error (between PIV and DNS) for the four groups of contributors
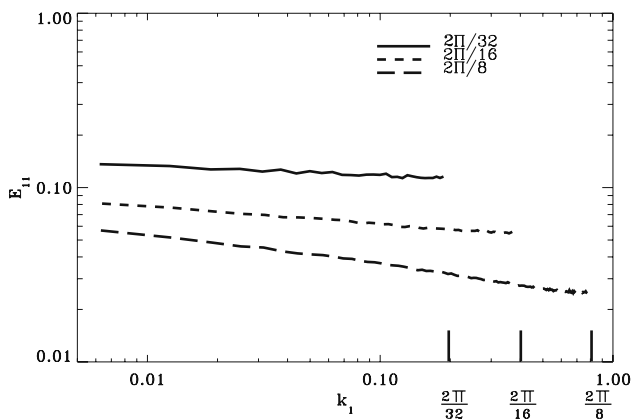


**Fig. 10** Case A1: Exact solution spectra filtered with different window sizes

interesting to notice that there may be a ratio of 10–100 between the errors of different algorithms (see FOI and ILA for example). While most algorithms show a flat error spectrum, the strength of some of them is to be able to reduce the error when the frequency increases (and the amplitude of the signal diminishes) this is surely due to an

appropriate filtering of the data during the iterative procedure.

Figure 14 gives the PDF obtained by the different teams, compared to the exact solution. The analysis of these curves is of interest. First of all, it appears that DLR has obtained its fairly good spectrum by filtering strongly the low amplitude fluctuations. Several groups, who did not filter so strongly and are thus not so good on the spectrum, do get the PDF quite well (DUTAE, UDN, LAVISION). This means that most of the PDF is built in this case by low frequency fluctuations (the spectrum slope is fairly strong) and that the noise which is added by these teams at high frequency is not sufficient to alter significantly the PDF. A spatial resolution of the order of $100 \times 100$ px is enough to catch correctly the pdf. A second point is that some contributors show a more or less strong peak locking (CORIA, FOI, GPIV). The strange behaviour shown by the results of CEM-IN at small amplitude cannot be attributed to standard peak locking as the method used is Optical Flow. YATS-IN which uses a similar approach shows a similar behaviour. For PTV, some algorithms (TAMU and VKI, also ESI to a smaller extent) show an under estimation of small displacements. URS2 filters these small displacements. Obviously, displacements
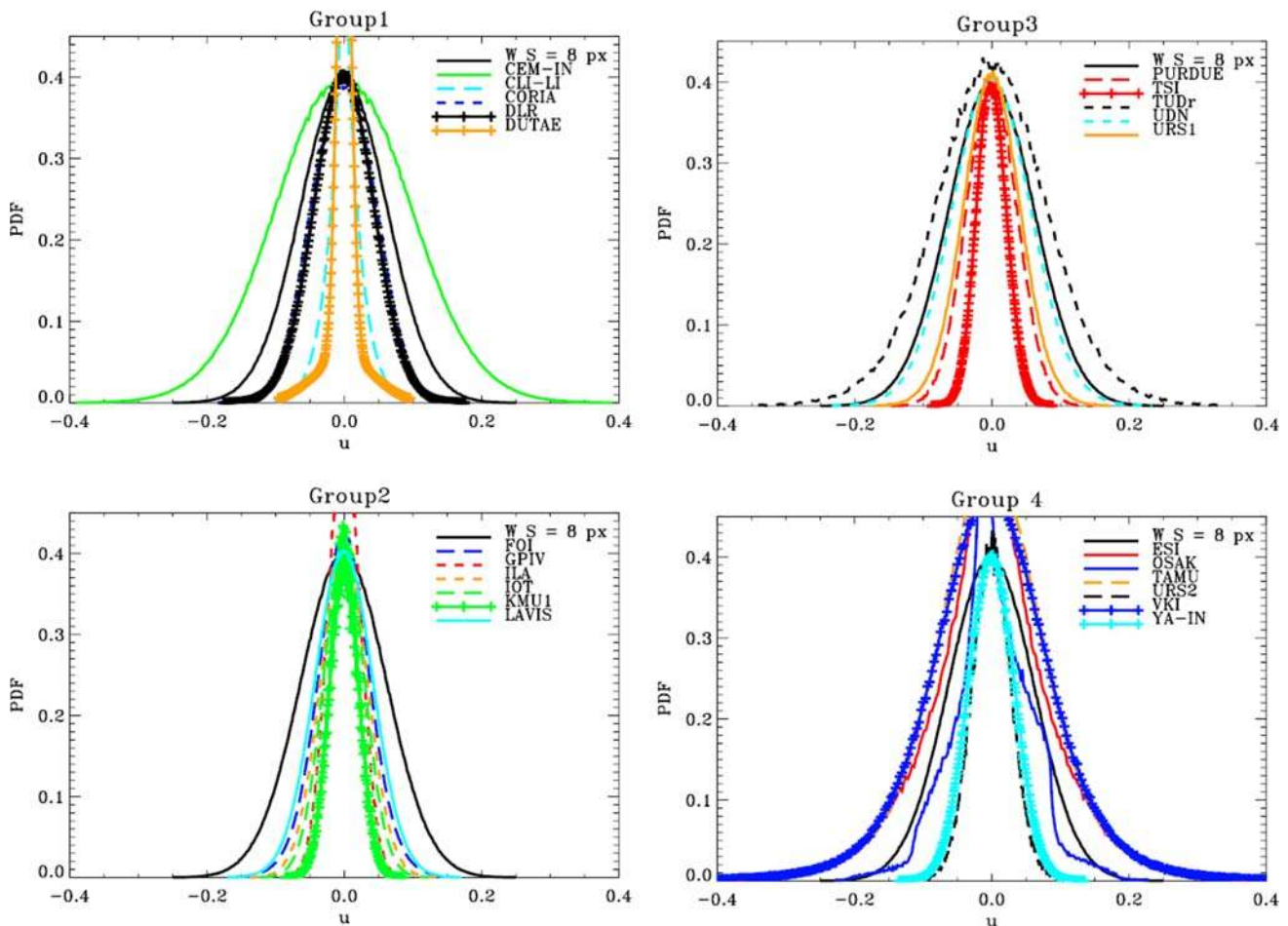
**Fig. 11** Case A1: Probability density function of the $u'$ component compared to the reference for the four groups of contributors

smaller than 1px have posed problems to most of the contributors.

The statistics obtained by the different teams are given in Table 11 in the same manner as in Table 10. Here again, the mean value of the velocity is fairly well assessed by most of the contributors, especially those showing good results in Figs. 12, 13 and 14. In contrast to case A1, the estimate of the RMS fluctuations is more accurate here. Ten teams are within 10% of the RMS value for the $U$-component. The best teams reach a relative RMS error of 5%. This error is particularly bad for PTV algorithms. It is remarkable that the optical flow approach (CEM-IN & CLI-LI) exhibits very small bias error but its RMS error is about twice than the cross-correlation methods.

### 4.3 Case A3

The interest of this test case is in the specific structure of the turbulence used to generate it. This turbulence in a stratified fluid shows a standard turbulence spectrum (decreasing with increasing frequency) but, due to the stratification, a specific instability appears at high wave

number. This instability is detectable in the instantaneous flow fields (Fig. 15) and also as a bump in the spectrum. Based on the turbulent fields available from a DNS (Laval et al. 2003) the PIV field of view was tuned to locate the bump at a wave number approximately $k_1 = 2\pi/32$.

Figure 16 shows the comparison of the spectrum between the different teams and with the reference. Only 7 teams among 22 were able to detect the hidden instability. Among these seven, the best result is clearly obtained by UDN. CORIA, DLR, DUTAE and Lavision, which do quite well are all (more or less) victims of the filtering applied to remove the high frequency noise. Among the optical flow contributors, CLI-LI shows a correct trend with a spectral broadening, while CEM-IN and YA-IN miss it completely.

The spectrum of the error is given in Fig. 17. Again, significant differences appear between the different algorithms. The difference is obviously between algorithms which can reach a level of nearly $10^{-3}$ beyond $2\pi/32$ and those which stay between $5 \times 10^{-3}$ and $10^{-1}$ (compare for example UDN and TSI).

Figure 18 gives the PDF of the data provided, compared with the reference. A specificity of this PDF is that it

**Table 10** Mean and RMS velocities, bias and RMS error for case A1

| | Participant | | Border[a] correction | Velocity | | | | Error | | | | | |
|---|---|---|---|---|---|---|---|---|---|---|---|---|---|
| | No. | Acronym | | Mean | | RMS | | Bias | | RMS | | | |
| | | | | U | V | U | V | U | V | U | | V | |
| | | | | | | | | | | Absolute | Relative | Absolute | Relative |
| Ref.[b] | | | | 0.0000 | 0.0000 | 0.2170 | 0.2171 | | | | | | |
| Ref. PIV[c] | WS = 8 px | | | 0.0000 | 0.0000 | 0.0625 | 0.0626 | | | | | | |
| 1 | 15 | CEM-IN | None | 0.0011 | 0.0002 | 0.0976 | 0.0972 | 0.0012 | 0.0003 | 0.1155 | 1.85 | 0.1151 | 1.84 |
| 1 | 14 | CLI-LI | None | 0.0000 | 0.0000 | 0.0254 | 0.0254 | 0.0000 | 0.0000 | 0.0555 | 0.89 | 0.0543 | 0.87 |
| 1 | 4 | CORIA | None | 0.0000 | 0.0000 | 0.0463 | 0.0463 | 0.0001 | 0.0000 | 0.0559 | 0.89 | 0.0559 | 0.89 |
| 1 | 12 | DLR | None | 0.0000 | 0.0000 | 0.0440 | 0.0440 | 0.0000 | 0.0000 | 0.0524 | 0.84 | 0.0525 | 0.84 |
| 1 | 2 | DUTAE | X:3–250 | 0.0000 | 0.0000 | 0.0240 | 0.0240 | 0.0000 | 0.0000 | 0.0605 | 0.97 | 0.0605 | 0.97 |
| 2 | 1 | FOI | None | 0.0000 | 0.0000 | 0.0397 | 0.0398 | 0.0000 | 0.0000 | 0.0742 | 1.19 | 0.0704 | 1.12 |
| 2 | 17 | GPIV | X:0–246 | 0.0000 | 0.0000 | 0.0234 | 0.0234 | 0.0005 | −0.0002 | 0.0564 | 0.90 | 0.0564 | 0.90 |
| 2 | 18 | ILA | X:3–125 | 0.0000 | 0.0000 | 0.0344 | 0.0345 | 0.0000 | 0.0000 | 0.0539 | 0.86 | 0.0540 | 0.86 |
| 2 | 11 | IOT | None | 0.0000 | 0.0000 | 0.0308 | 0.0308 | 0.0000 | 0.0000 | 0.0539 | 0.86 | 0.0541 | 0.86 |
| 2 | 13 | KMU1 | X:3–77 | −0.0001 | 0.0000 | 0.0213 | 0.0213 | 0.0000 | −0.0002 | 0.0571 | 0.91 | 0.0572 | 0.91 |
| 2 | 7 | LAVIS | X:3–252 | 0.0000 | 0.0000 | 0.0427 | 0.0427 | 0.0000 | 0.0000 | 0.0514 | 0.82 | 0.0515 | 0.82 |
| 3 | 3 | PURDUE | None | −0.0001 | 0.0000 | 0.0369 | 0.0369 | −0.0002 | 0.0000 | 0.0565 | 0.90 | 0.0562 | 0.90 |
| 3 | 21 | TSI | X:2–122 | 0.0009 | 0.0009 | 0.0221 | 0.0220 | 0.0011 | 0.0009 | 0.0568 | 0.91 | 0.0569 | 0.91 |
| 3 | 16 | TUDr | None | −0.0001 | 0.0000 | 0.0851 | 0.0853 | 0.0003 | −0.0003 | 0.0839 | 1.34 | 0.0841 | 1.34 |
| 3 | 10 | UDN | None | 0.0000 | 0.0000 | 0.0583 | 0.0583 | 0.0001 | 0.0000 | 0.0577 | 0.92 | 0.0578 | 0.92 |
| 3 | 5 | URS1 | None | 0.0000 | 0.0000 | 0.0429 | 0.0429 | 0.0000 | 0.0000 | 0.0625 | 1.00 | 0.0626 | 1.00 |
| 4 | 19 | ESI | None | 0.0000 | −0.0002 | 0.0929 | 0.0927 | 0.0003 | −0.0004 | 0.1119 | 1.79 | 0.1110 | 1.77 |
| 4 | 9 | OSAK | None | 0.0130 | −0.0287 | 0.0571 | 0.0616 | 0.0134 | −0.0031 | 0.0698 | 1.12 | 0.0708 | 1.13 |
| 4 | 22 | TAMU | None | 0.0000 | 0.0000 | 0.1026 | 0.1026 | 0.0001 | 0.0000 | 0.1056 | 1.69 | 0.1056 | 1.69 |
| 4 | 6 | URS2 | None | 0.0000 | 0.0002 | 0.0294 | 0.0293 | −0.0007 | −0.0002 | 0.0689 | 1.10 | 0.0700 | 1.12 |
| 4 | 8 | VKI | None | 0.0000 | 0.0000 | 0.0996 | 0.0997 | 0.0000 | 0.0000 | 0.1000 | 1.60 | 0.1002 | 1.60 |
| 4 | 20 | YA-IN | None | 0.0000 | 0.0000 | 0.0338 | 0.0338 | 0.0000 | 0.0000 | 0.0338 | 0.54 | 0.0338 | 0.54 |

[a] Border correction: for some contributors, it was necessary to remove one line or column near the border to get correct statistics

[b] Ref: direct result of the simulation without any filtering on a 4 × 4 px grid

[c] Ref PIV: result of the simulation on the contributor's grid averaged on 8 × 8 px windows

exhibits two peaks. This is captured by most of the contributors (except for those showing a strong peak locking like FOI or GPIV), since the double peak is due to low frequency motions and not to the high frequency instability.

Finally, Table 12 gives the mean and RMS values together with the bias and RMS error. The conclusions are comparable with case A2. A very small bias is reached by several teams and the RMS error is comparable to case A2: less than 0.04 px and of the order of 5% in the best cases.

### 4.4 Case A4

The result of the image interrogation by the different contributors is analysed separately for each region. Data close to the border of each region are not considered since the border size is not identical among participants. It is made sure that no outliers at the borders are included in the analysis. The results are processed in order to deduce the following information:

1. Mean amplitude response $U^* = U_{meas}/U_{exact}$ at every wavelength $\lambda$.
2. Total error summing up the modulation error and the rms uncertainty at each wavelength.
3. Cut-off (co) wavelength $\lambda_{co}$ where the algorithm yields 10% drop from the applied displacement amplitude (at $\lambda = \lambda_{co} => U^* = U_{meas}/U_{exact} = 0.9$).
4. wavelength $\lambda_{ERR}-20\%$ at which the total error (mean+RMS error) reaches 20% of the sinusoid amplitude (at $\lambda = \lambda_{ERR}-20\% => |1-U^*| + RMS(U_{meas}) = 0.2*U_{exact}$)
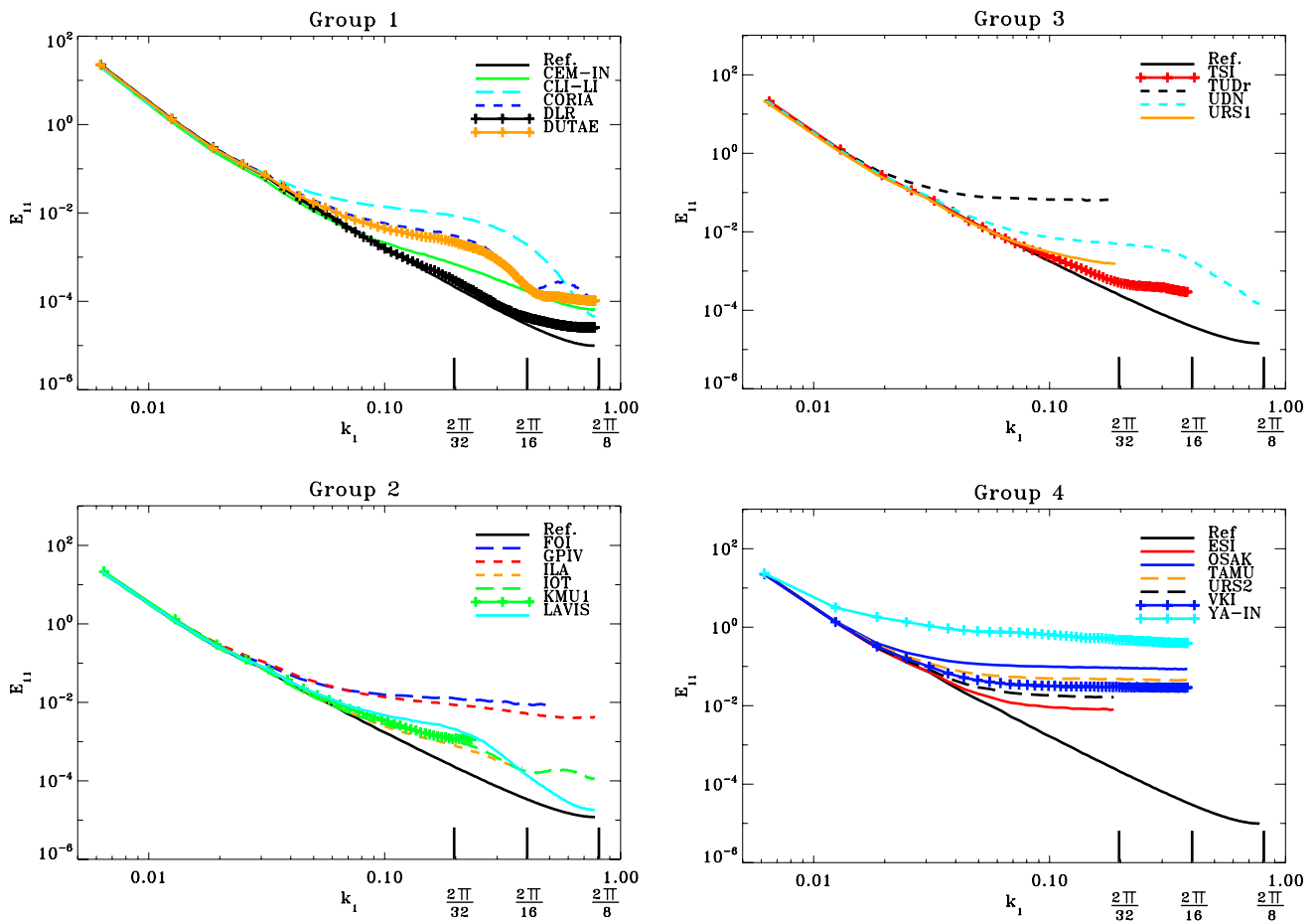
**Fig. 12** Case A2: Power spectrum on the $u'$ component compared to the reference spectrum for the four groups of contributors

Figure 19 shows the difference between the measured displacement field and the applied displacement field for all participants. Only the *V*-component is shown. Most participants perform rather well for the wall-bounded flow in the top-left corner. Also in the top-right region starting from the left side the error is very low for all participants, and increases moving towards the right where the displacement field fluctuates at higher spatial frequency. It was chosen on purpose to keep the amplitude of the sinusoidal fluctuations constant in such a way that the modulation error can be clearly identified from other forms of error (e.g. sub-pixel precision, outliers). Moving downwards more uncorrelated particles are introduced and the noise level increases significantly in the third region. On the bottom-left corner, the two-dimensional sinusoids test can be very easily interpreted: the patches that are made visible plotting the error correspond to the wavelengths that are not resolved by the interrogation. Most interrogations do not show any visible error for the wavelengths of 200 and 100 px. However, depending on the interrogation algorithm and especially on the size of the window and the weighting function, the spatial resolution varies significantly.

### 4.4.1 1-D sinusoidal shearing displacement

The most important result of the test is to yield a quantitative spatial resolution assessment with respect to a 1-D sinusoidal displacement. This is made evaluating the amplitude response coefficient for each wavelength (Schrijer and Scarano 2006). Only the component in the *y*-direction of the displacement vector is nonzero and the sinusoids decrease in wavelength from the left to the right side of the image. The sinusoid amplitude vary between 2 and 3 px depending on the wavelength. A direct visualization of the result obtained by each group is given in Fig. 20, showing the raw displacement profiles measured in the right-uppermost region of the image, where no noise is added in terms of unpaired particle images. Each diagram shows the actual displacement with a black solid line and several profiles obtained at different heights with solid blue lines. Several groups show a very accurate measurement of the displacement for large wavelengths and the difference with respect to the actual displacement is barely visible (CORIA, DLR, DUTAE, LAVISION, UDN, URS2). Conversely a few groups show a significant measurement scatter at these large wavelengths indicating a poor accuracy
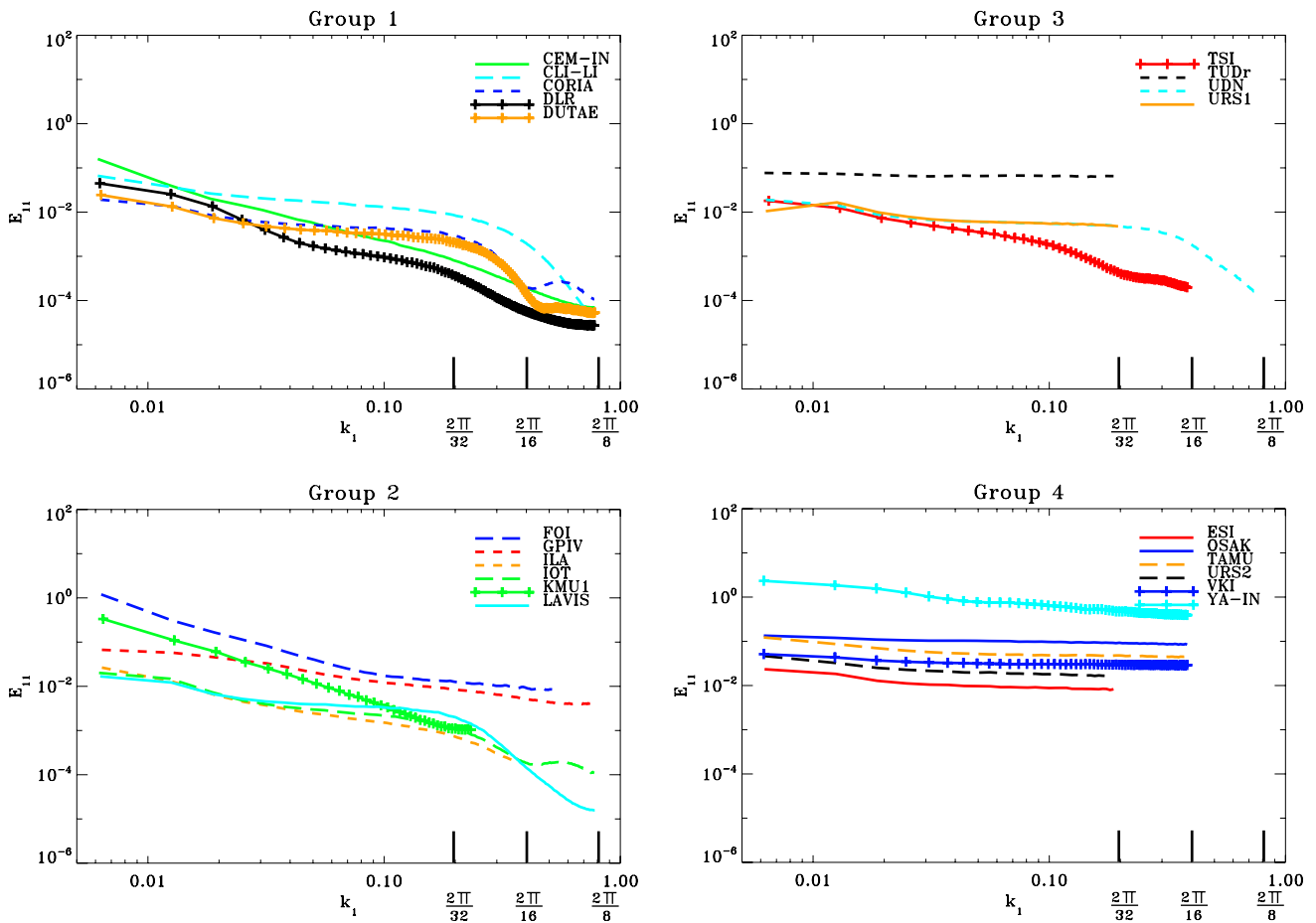
**Fig. 13** Case A2: Power spectrum of the error (between PIV and DNS) for the four groups of contributors

of the interrogation scheme (CEMAGREF, ESI, TAMU, VKI). In most cases the wavelength at which modulation starts to be observed is around $\Lambda = 60$ px. An increasing data scatter is observed at small wavelengths, as expected, due to the large displacement differences along the interrogation area, which lead to correlation peak spread for cross-correlation and to a more uncertain pairing for particle tracking.

The modulation error can be evaluated in a robust way plotting the amplitude ratio $U^*$, defined as an integral property over a half wavelength $\Lambda$. The total error is obtained summing up the modulation effects and the rms fluctuations. The expressions used in the present procedure are given below:

$$U^* = \frac{\int_{x=-\Lambda/4}^{x=+\Lambda/4} U_{\mathrm{meas}} dx}{\int_{x=-\Lambda/4}^{x=+\Lambda/4} U_{\mathrm{exact}} dx};$$

$$\mathrm{ERR} \equiv \frac{\int_{x=-\Lambda/4}^{x=+\Lambda/4} [|1 - U_{\mathrm{meas}}| + \mathrm{rms}(U_{\mathrm{meas}})] dx}{\int_{x=-\Lambda/4}^{x=+\Lambda/4} U_{\mathrm{exact}} dx}$$

The diagrams shown in Fig. 21 top return the normalised mean response as a function of the wavelength of the input

sinusoid. Most contributors return $U^* \approx 1$ at $\Lambda = 400$ px, as expected, meaning that the measurement are not affected by any bias effect. With the present test the $-3$ dB cut-off spatial frequency (corresponding to $U^* = 0.5$) is difficult to evaluate, since for most algorithms a modulation below 50% is not reached even at the lowest spatial wavelength considered (20 px). Moreover when the modulation exceeds about 25%, the random fluctuations become an important component of the total error. It becomes therefore more interesting to analyze the modulation effects monitoring as cut-off wavelength $\lambda_{\mathrm{co}-10\%}$ at which the measurement returns $U^* = 0.9$ (10% systematic error on the measurement). Table 13 sorts the results of the participants with respect to $\lambda_{\mathrm{co}-10\%}$. The first five groups (CORIA, DUTAE, UDN, DLR, LAVIS) all adopt iterative image deformation interrogation and the minimum wavelength resolved ranges between 20 and 30 px.

The total error is evaluated summing up the mean modulation error and the standard deviation of the measured displacement. The results are shown in Fig. 21 bottom. The error term is normalized with the integral of
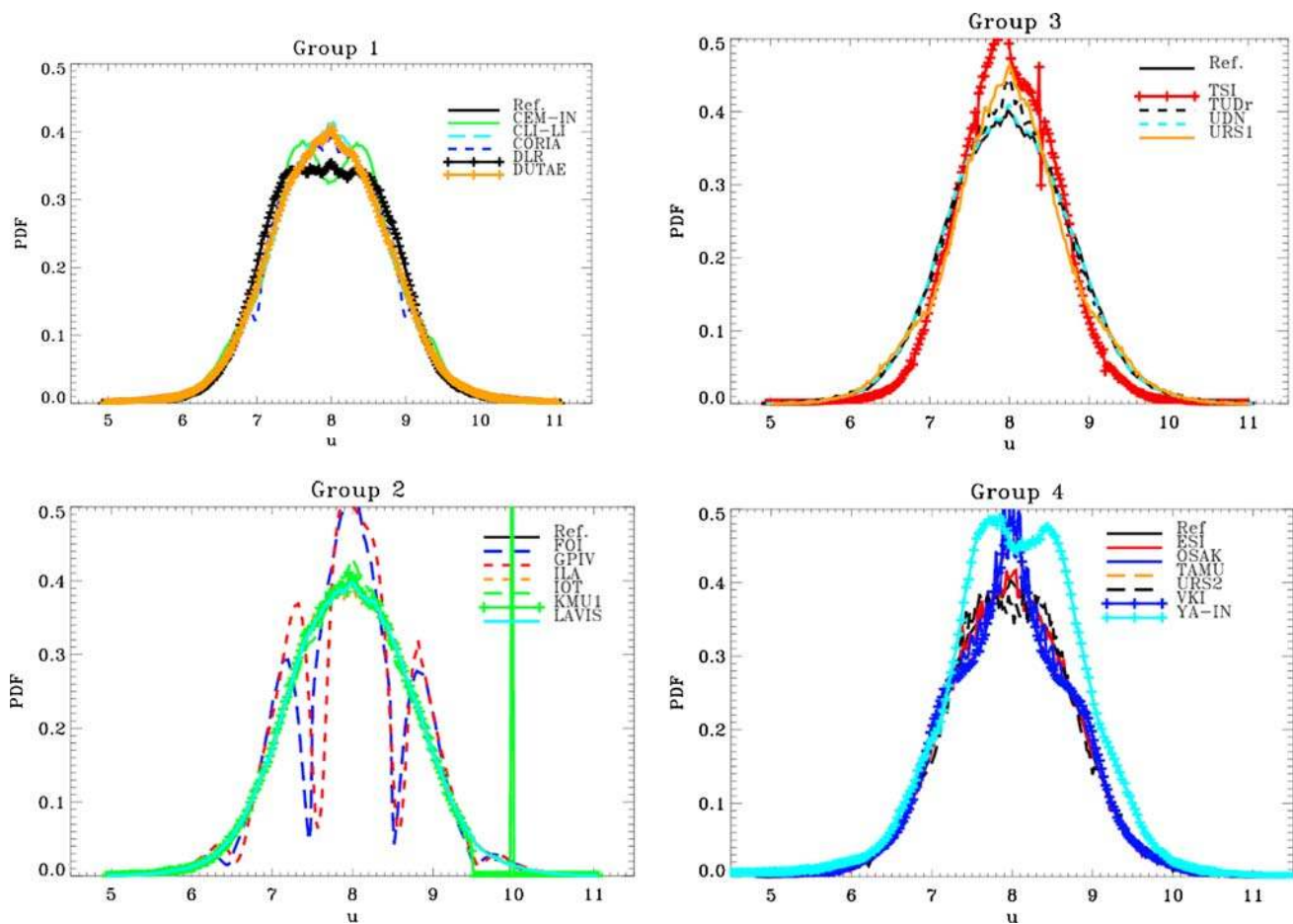
**Fig. 14** Case A2: Probability density function of the $u'$ component compared to the reference for the four groups of contributors

the displacement over a half wavelength. The total error result in terms of $\lambda_{ERR}-20\%$ is summarized in Table 14. Some minor changes are observed in the order among the groups indicating that the modulation and random error are not completely independent.

The case with 20% unpaired particles (the second block of sinusoids from the top right) mimics typical experimental conditions where laser sheet overlap is not optimal and out-of plane motion occurs. The overall result does not change significantly indicating that the spatial resolution is not affected by such noise levels in the measurement. However, the case with 60% unpaired particle images returns an important drop of the spatial resolution dominated by the random component of the error.

### 4.4.2 2-D sinusoidal fluctuations

The 1-D test is generalized to a two dimensional displacement field by means of 2D sinusoidal fluctuations with varying wavelength and slightly varying amplitude. This test represents more closely the situation encountered in real experimental conditions where the flow variations do not exhibit a preferential direction (e.g. isotropic turbulence, vortices). However one should keep in mind that also the 1-D case may be regarded as relevant for fluid flow conditions in that it is representative of shear layers and shock waves. The results are shown in Fig. 22, where it is clear that it is more difficult to measure small 2-D swirling motion than 1-D shear. The cut-off wavelength where the amplitude ratio falls below 90% is for most teams about 50% higher than for the 1-D case. The 10% cut off occurs much earlier for the 2-D case as expected (between 32 and 56 px for most cases). The same occurs for the wavelength at which the total error is 20%. The results synthesized in Table 14 show again that the groups adopting iterative interrogation with window deformation are able to resolve smaller wavelengths. The application of window weighting functions seems to yield an additional advantage for the analysis of this case.

Note: The analysis provided by TAMU is affected by errors associated to the image reader.

**Table 11** Mean, RMS velocities, bias and RMS error for case A2

| Participant | | Border[a] correction | Velocity | | | | Error | | | | | |
|---|---|---|---|---|---|---|---|---|---|---|---|---|
| | | | Mean | | RMS | | Bias | | RMS | | | |
| No. | Acronym | | U | V | U | V | U | V | U | | V | |
| | | | | | | | | | Absolute | Relative | Absolute | Relative |
| Ref | | | 8.0000 | 0.0000 | 0.7605 | 0.7751 | | | | | | |
| 1 | 15 | CEM-IN | None | 8.0058 | 0.0011 | 0.7771 | 0.7930 | 0.0058 | 0.0011 | 0.1600 | 0.21 | 0.1700 | 0.22 |
| 1 | 14 | CLI-LI | None | 8.0005 | −0.0001 | 0.7536 | 0.7701 | 0.0005 | −0.0001 | 0.0900 | 0.12 | 0.0900 | 0.12 |
| 1 | 4 | CORIA | None | 7.9992 | −0.0013 | 0.7634 | 0.7775 | −0.0008 | −0.0013 | 0.0500 | 0.07 | 0.0500 | 0.06 |
| 1 | 12 | DLR | None | 7.9988 | −0.0005 | 0.7682 | 0.7811 | −0.0012 | −0.0005 | 0.0400 | 0.05 | 0.0400 | 0.05 |
| 1 | 2 | DUTAE | X:3–250 | 7.9987 | −0.0006 | 0.7615 | 0.7763 | −0.0013 | −0.0006 | 0.0500 | 0.07 | 0.0500 | 0.06 |
| 2 | 1 | FOI | None | 7.9978 | −0.0025 | 0.7542 | 0.7697 | −0.0022 | −0.0025 | 0.2200 | 0.29 | 0.1600 | 0.21 |
| 2 | 17 | GPIV | X:0–246 | 7.9573 | −0.0023 | 0.7686 | 0.7647 | −0.0427 | −0.0023 | 0.1171 | 0.15 | 0.1146 | 0.15 |
| 2 | 18 | ILA | X:3–125 | 7.9974 | −0.0022 | 0.7606 | 0.7743 | −0.0026 | −0.0022 | 0.0400 | 0.05 | 0.0400 | 0.05 |
| 2 | 11 | IOT | None | 7.9894 | −0.0007 | 0.7578 | 0.7672 | −0.0106 | −0.0007 | 0.0400 | 0.05 | 0.0400 | 0.05 |
| 2 | 13 | KMU1 | X:3–77 | 8.0006 | −0.0029 | 0.7650 | 0.7708 | 0.0006 | −0.0029 | 0.1000 | 0.13 | 0.0700 | 0.09 |
| 2 | 7 | LAVIS | X:3–252 | 7.9986 | −0.0011 | 0.7623 | 0.7768 | −0.0014 | −0.0011 | 0.0400 | 0.05 | 0.0400 | 0.05 |
| 3 | 3 | PURDUE | | | | | | | | | | | |
| 3 | 21 | TSI | X:2–122 | 7.9698 | 0.0097 | 0.7574 | 0.7716 | −0.0302 | 0.0097 | 0.0400 | 0.05 | 0.0400 | 0.05 |
| 3 | 16 | TUDr | None | 7.9974 | −0.0008 | 0.7778 | 0.7919 | −0.0026 | −0.0008 | 0.1600 | 0.21 | 0.1600 | 0.21 |
| 3 | 10 | UDN | None | 7.9982 | −0.0014 | 0.7639 | 0.7782 | −0.0018 | −0.0014 | 0.0600 | 0.08 | 0.0600 | 0.08 |
| 3 | 5 | URS1 | None | 7.9990 | −0.0003 | 0.7520 | 0.7688 | −0.0010 | −0.0003 | 0.0500 | 0.07 | 0.0500 | 0.06 |
| 4 | 19 | ESI | None | 7.9828 | −0.0013 | 0.7614 | 0.7879 | −0.0152 | −0.0006 | 0.0639 | 0.08 | 0.0539 | 0.07 |
| 4 | 9 | OSAK | None | 7.9975 | −0.0006 | 0.7999 | 0.7823 | −0.0020 | −0.0001 | 0.2716 | 0.36 | 0.1422 | 0.18 |
| 4 | 22 | TAMU | None | 7.9977 | −0.0003 | 0.7736 | 0.7951 | −0.0018 | 0.0002 | 0.1988 | 0.26 | 0.1729 | 0.22 |
| 4 | 6 | URS2 | None | 7.9976 | −0.0018 | 0.7620 | 0.7750 | −0.0004 | 0.0001 | 0.0620 | 0.08 | 0.0533 | 0.07 |
| 4 | 8 | VKI | None | 7.9948 | 0.0002 | 0.7746 | 0.7875 | −0.0047 | −0.0003 | 0.1557 | 0.20 | 0.1401 | 0.18 |
| 4 | 20 | YA-IN | None | 7.8734 | −0.0011 | 1.0174 | 0.7642 | −0.1261 | −0.0006 | 0.6948 | 0.91 | 0.0793 | 0.10 |

[a] Border correction: for some contributors, it was necessary to remove one line or column near the border to get correct statistics
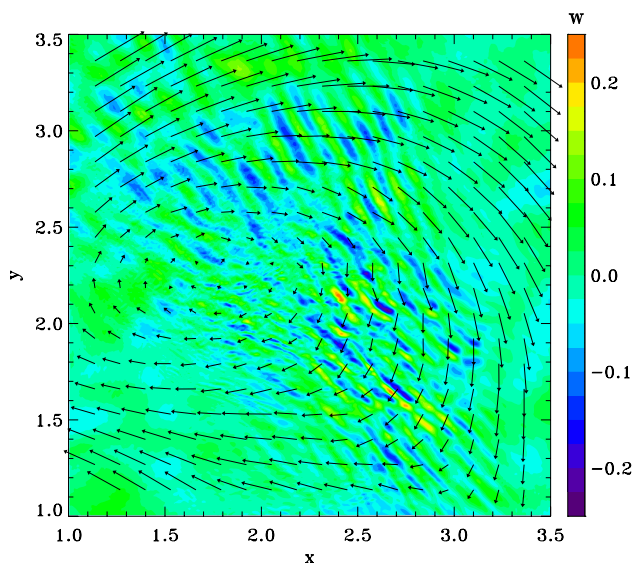


**Fig. 15** Sample of instantaneous velocity field in the *xy* plane for case A3, showing the high frequency instability

### 4.5 Conclusion on case A

The aim of this test case was to assess the spatial resolution of the different evaluation algorithms. For that purpose, two types of images were selected. On one side, sets of synthetic images generated from numerical simulations with different types of spectrum (Cases A1–3). On the other side one patchwork image containing different tests of spatial resolution (Case A4).

In the first case, the aim was to test the ability of the algorithms to resolve the small scales in a turbulent flow. For that purpose, the slope and the shape of the spectrum were varied. Case A1, with a flat spectrum was a very difficult test case. All frequencies contain the same energy. It shows the robustness of the PIV algorithms for the extraction of the mean velocity. This is a well known property of the cross-correlation analysis which is well illustrated there. It also shows the limits as far as the spatial fluctuations are concerned. Since they are fully random in this case, the RMS is not correctly assessed. In fact, this
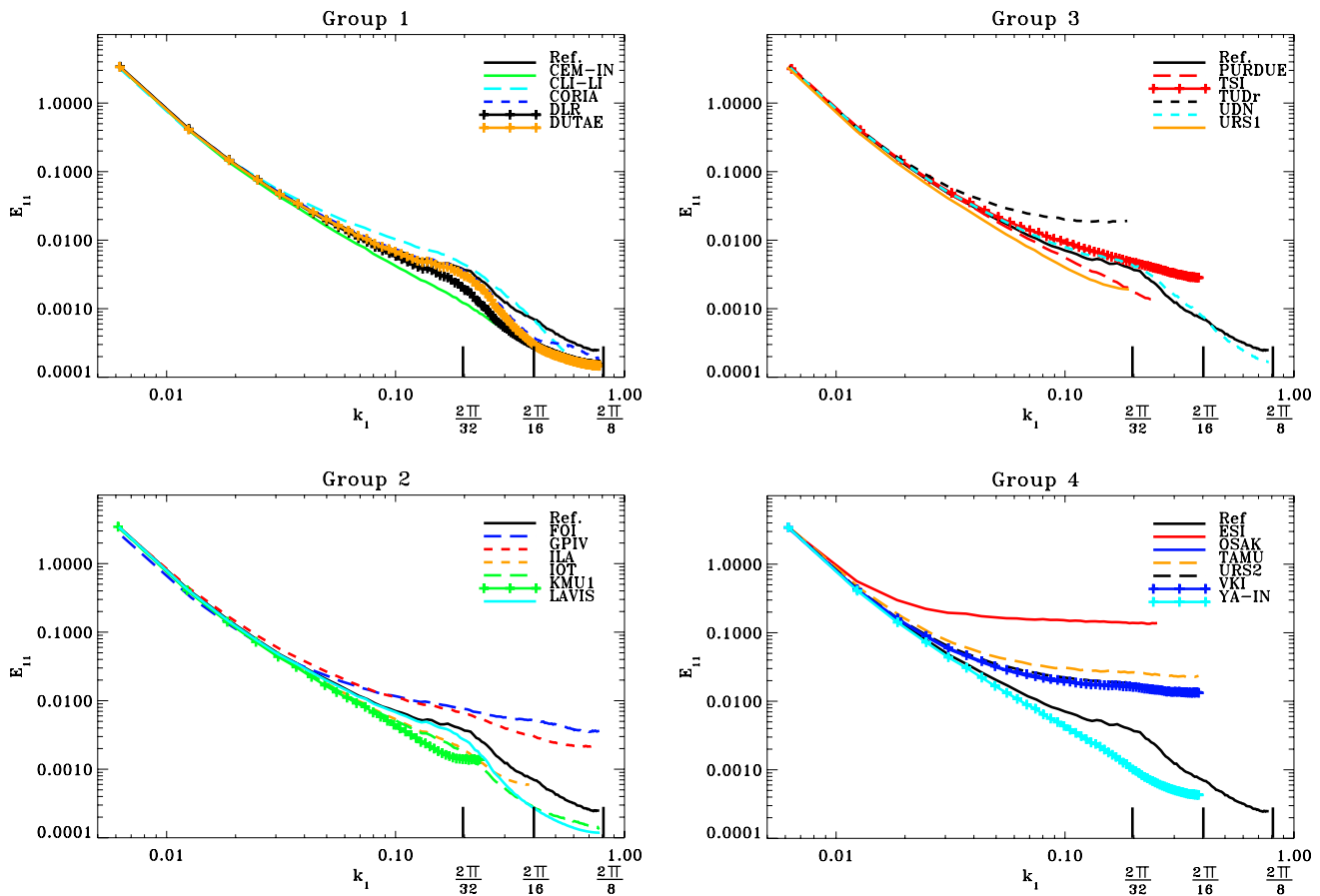
**Fig. 16** Case A3: Power spectrum on the $u'$ component compared to the reference spectrum for the four groups of contributors

test case is more representative of a laminar flow with a lot of noise than of a real turbulent situation. Case A2, with a strong slope of the spectrum, is another challenge. The amplitude of the signal decrease very rapidly with growing wave number. Small differences in the noise level introduced by the algorithms affect directly the spatial resolution. About one order of magnitude difference is observed on the scales resolved between the extreme contributions, corresponding to about three orders of magnitude in energy. Case A3 was aimed at testing the ability of the algorithms to evidence a real physical phenomenon near the limit of the present spatial resolution of PIV. The results are fairly instructive. They give a clear advantage to the advanced algorithms using multi-pass, multi-grid and image deformation strategies. But, obviously, the filtering of high frequency noise still needs to be clarified. A point should be made on optical flow. Different groups around the world are working with correlation PIV for many years now and the theory is fairly established. This is not the case for optical flow where it is still difficult to make a theoretical link between the algorithm and its accuracy. On the paper, Optical flow should be able to do better than correlation in terms of spatial resolution. The

present results show that this is not the case. At best, the optical flow results compare with an intermediate correlation algorithm. Finally, on the 3 test cases, the results of PTV are fairly disappointing. Although care was taken to make the comparison as good and as fair as possible, the noise level is higher and the spatial resolution is less than what is provided by the best correlation tools. Probably, the second is a consequence of the first. For the sake of equity, it should be noted that the test cases were optimised for correlation PIV in terms of particle image size and concentration. This is surely not favourable for PTV. Decreasing the seeding and increasing the particle image size would probably improve the PTV results. This would imply a specific study as there is no theory providing the optimal parameters as in correlation PIV.

As far as test case A4 is concerned, a compact test image on spatial resolution has been introduced to evaluate the algorithms performances. Such synthetic tests allow to evaluate the performance of interrogation techniques in terms of spatial resolution and accuracy with a compact image format and a controlled choice of the imaging and flow parameters. The spatial resolution from the different interrogation methods has been shown with a qualitative
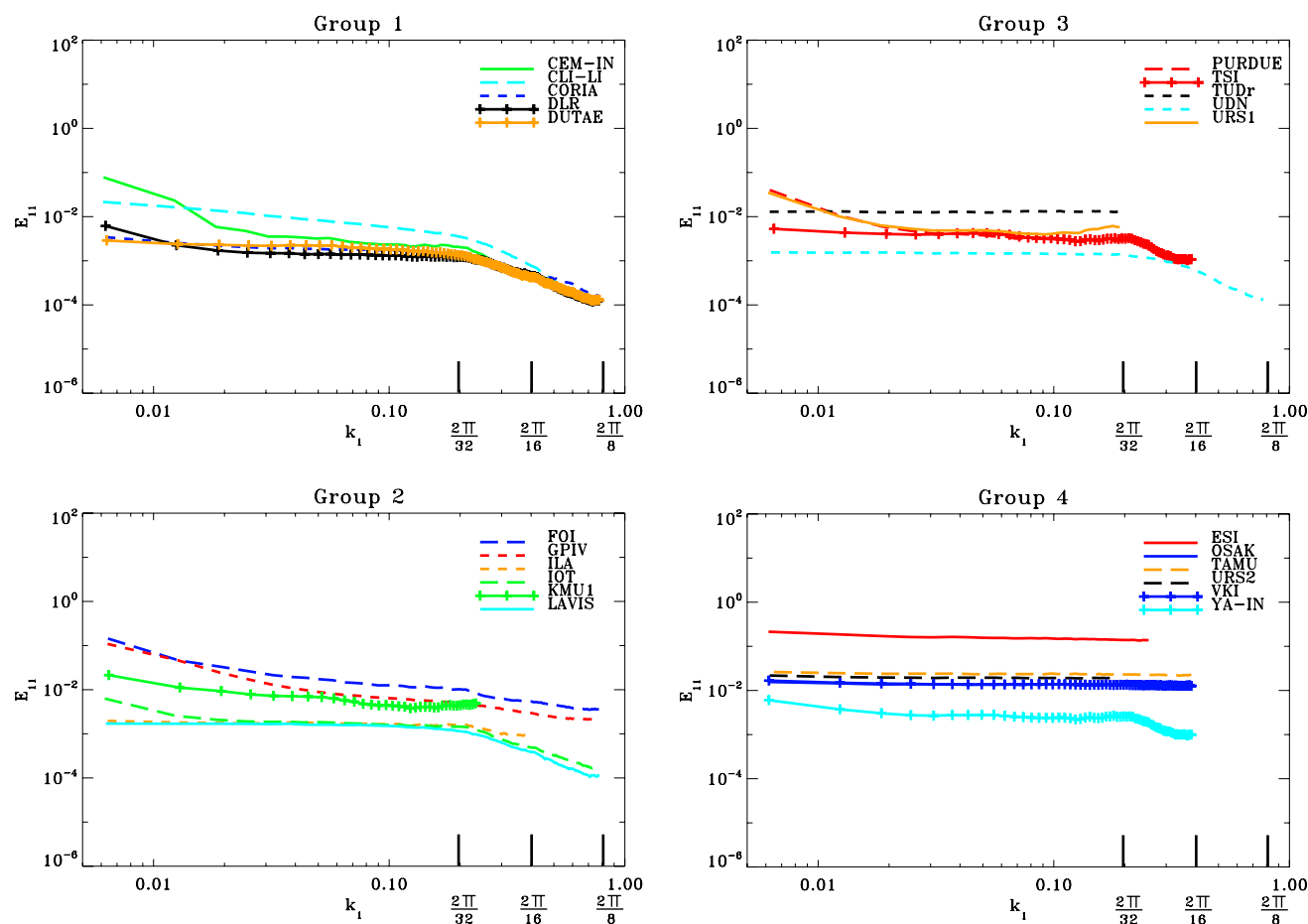
**Fig. 17** Case A3: Power spectrum of the error (between PIV and DNS) for the four groups of contributors

and quantitative approach. The algorithms performing iterative image deformation show the highest performance (CORIA, DLR, DUTAE, LAVIS, PURDUE, UDN). The smallest 1D fluctuation that has been faithfully represented (error below 20%) has a wavelength of about 25 px. This value grows to about 30 px for 2D fluctuations. The optical flow algorithms (CEMAGREF, CLI-LI) are closely following the iterative correlation methods. The particle tracking algorithms (VKI, YATS) although on overall perform relatively well, do not seem to benefit from their potentially higher resolution.

# 5 Case B

Case B of the PIV Challenge 2005, provided by TU Braunschweig, is a synthetic image sequence with equidistant time intervals between the 120 provided exposures (size $1,440 \times 688$ px$^2$). The particle image displacements are estimated by means of a direct numerical simulation (DNS) of a laminar separation bubble (Marxen et al. 2004) so that the synthetic flow is close to reality, see Fig. 23.

The large dynamic velocity range of DVR $\approx 50$ is a special challenge for the evaluation algorithms. In addition the signal to noise ratio is reduced with increasing time according to Fig. 24 in order to simulate different light sheet intensities, different particle diameters (Kähler et al. 2002) and different sensitivities of the recording camera (Hain et al. 2007). The signal to noise ratio in Fig. 24 is calculated by using the assumption that a particle is placed in the middle of the light sheet and also in the centre of a pixel. Due to the fact that this is not true for most of the particles, the mean signal to noise ratio is comparatively smaller.

On average, 25 particle images with a mean diameter of 2.0 px and a diameter standard deviation of 0.4 px are randomly distributed in a $32 \times 32$ px$^2$ interrogation window. The light sheet thickness is 20 px measured at the $e^{-2}$ intensity of the Gaussian shaped intensity distribution. The DNS data points have a distance of 13.04 px in $x$-direction, 10.5 px in $y$-direction and 57.96 px in $z$-direction. Interpolation is done with 4th order in $x$-direction, 6th order in $y$-direction, and linearly in $z$-direction. The interpolation in time is performed with second order accuracy.
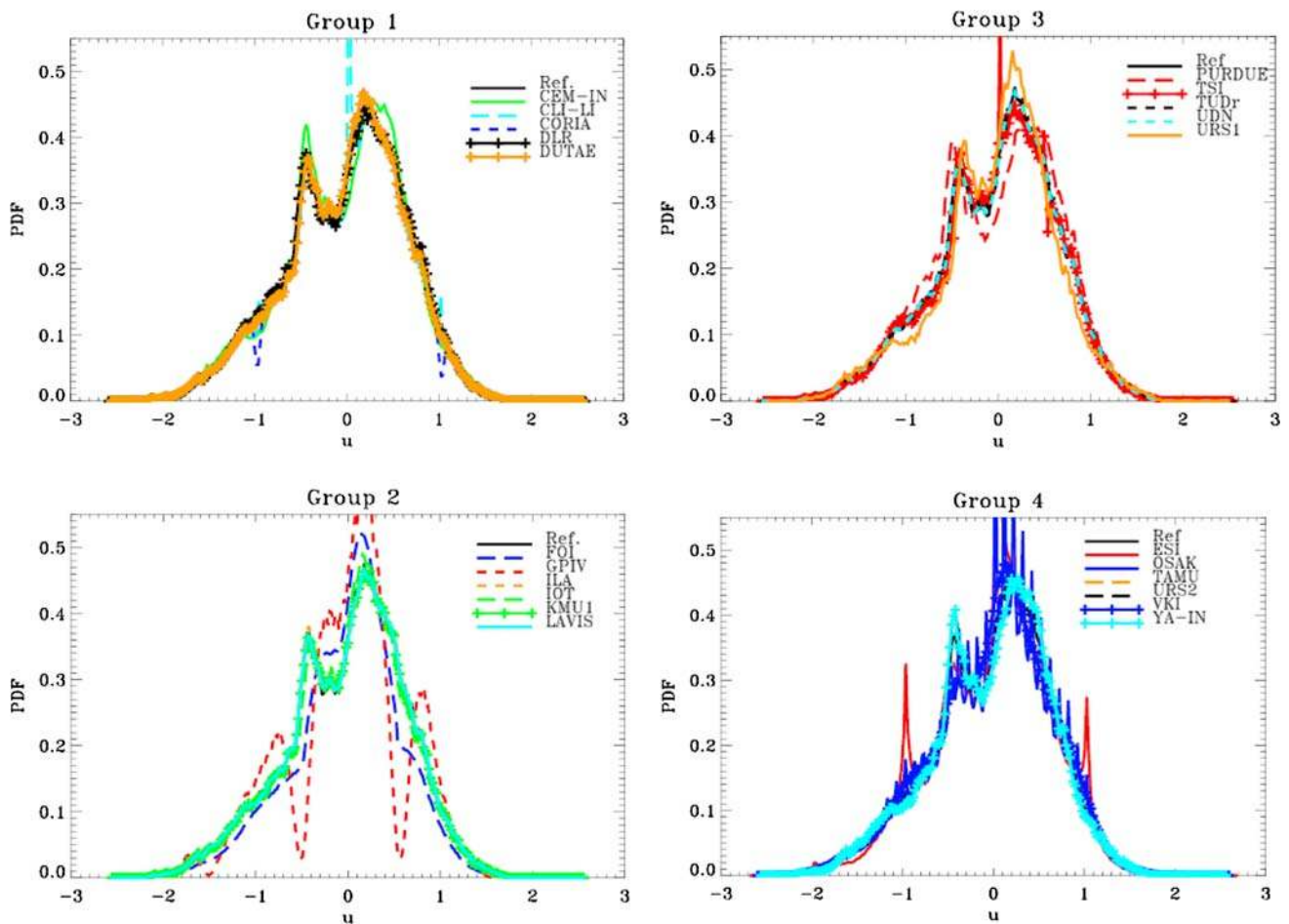
**Fig. 18** Case A3: Probability density function of the $u'$ component compared to the reference for the four groups of contributors

The product $F_I F_O F_\Delta$ (Keane and Adrian 1992; Hain and Kähler 2007) is shown in Fig. 25, assuming that $32 \times 32$ px$^2$ interrogation windows are applied for the evaluation. Due to the small displacements inside the laminar separation bubble, located at $x \approx 0 \dots 600$, $y \approx 500 \dots 680$, the product $F_I F_O F_\Delta$ is close to 1.0 in that region. The minimum of $F_I F_O F_\Delta \approx 0.5$ can be found near the position x $\approx 1,100$, y $\approx 480$. Here, large gradients and out-of-plane displacements are present.

The evaluation of Case B consists of two parts, called B1 and B2, which are outlined in detail in the following. In this paper the analysis of these cases is restricted to the displacements $\Delta x$ in x-direction. The analysis of the displacements in y-direction nearly leads to the same conclusions.

### 5.1 Evaluation of case B1

The evaluation of B1 was done at time-steps 10, 30, 50, 70, 90, and 110. To determine the displacements, image $n - 1$ and image $n + 1$ were considered. At time-step 10 for example, the algorithms have estimated the displacements

from image 9 to image 11. The contributors which participated in that test case and the parameter for their analysis, are given in Table 15.

The exact locations of the grid points are:

$X = 24 \dots 1416$   88   Nodes
  (grid distance   $x = 16$ pixel)

$Y = 24 \dots 664$   41   Nodes
  (grid distance   $y = 16$ pixel)

The PIV teams were forced to use interrogation windows with a size of $32 \times 32$ px$^2$. This is necessary to ensure that the same information is used for the estimation of the displacements. The deviations of the displacements in x-direction $\Delta x' = \Delta x_{contributor} - \Delta x_{exact}$ in comparison with the exact solution are shown in Fig. 26 for time-step $t = 10$.

Some teams such as CORIA, FOI or GPIV reveal a noisy field of the deviations in the region $x \approx 200 \dots 450$. The main reason is the gradient $d\Delta x/dy$. Looking at the deviations from CEMAGREF-INRIA, some significant

**Table 12** Mean, RMS velocities, bias and RMS error for case A3

| | Participant | | Border[a] correction | Velocity | | | | Error | | | | | |
|---|---|---|---|---|---|---|---|---|---|---|---|---|---|
| | | | | Mean | | RMS | | Bias | | RMS | | | |
| | No. | Acronym | | U | V | U | V | U | V | U | | V | |
| | | | | | | | | | | Absolute | Relative | Absolute | Relative |
| Ref | | | | −0.0375 | −0.0003 | 0.6414 | 0.5527 | | | | | | |
| 1 | 15 | CEM-IN | None | −0.0319 | −0.0010 | 0.6483 | 0.5582 | 0.0039 | −0.0003 | 0.0940 | 0.15 | 0.0926 | 0.17 |
| 1 | 14 | CLI-LI | None | −0.0364 | −0.0007 | 0.6401 | 0.5487 | −0.0007 | 0.0000 | 0.0620 | 0.10 | 0.0615 | 0.11 |
| 1 | 4 | CORIA | None | −0.0376 | 0.0000 | 0.6418 | 0.5547 | 0.0005 | 0.0003 | 0.0360 | 0.06 | 0.0365 | 0.07 |
| 1 | 12 | DLR | None | −0.0353 | 0.0007 | 0.6463 | 0.5599 | 0.0022 | 0.0011 | 0.0350 | 0.05 | 0.0353 | 0.06 |
| 1 | 2 | DUTAE | X:3–250 | −0.0386 | −0.0003 | 0.6400 | 0.5528 | −0.0004 | 0.0000 | 0.0350 | 0.05 | 0.0347 | 0.06 |
| 2 | 1 | FOI | None | −0.0394 | −0.0035 | 0.5746 | 0.4929 | −0.0018 | −0.0021 | 0.1420 | 0.22 | 0.1306 | 0.24 |
| 2 | 17 | GPIV | X:0–246 | −0.0397 | 0.0011 | 0.6294 | 0.5428 | −0.0001 | 0.0021 | 0.0990 | 0.15 | 1.0922 | 1.98 |
| 2 | 18 | ILA | X:3–125 | −0.0389 | 0.0000 | 0.6391 | 0.5533 | 0.0002 | 0.0000 | 0.0330 | 0.05 | 0.0334 | 0.06 |
| 2 | 11 | IOT | None | −0.0384 | −0.0001 | 0.6307 | 0.5399 | −0.0015 | −0.0008 | 0.0380 | 0.06 | 0.0381 | 0.07 |
| 2 | 13 | KMU1 | X:3–77 | −0.0405 | −0.0011 | 0.6379 | 0.5474 | −0.0012 | −0.0001 | 0.0560 | 0.09 | 0.0510 | 0.09 |
| 2 | 7 | LAVIS | X:3–252 | −0.0379 | −0.0002 | 0.6407 | 0.5526 | 0.0000 | 0.0000 | 0.0320 | 0.05 | 0.0320 | 0.06 |
| 3 | 3 | PURDUE | None | −0.0310 | 0.0020 | 0.6554 | 0.5724 | 0.0064 | 0.0026 | 0.0570 | 0.09 | 0.0574 | 0.10 |
| 3 | 21 | TSI | X:2–122 | −0.0277 | 0.0126 | 0.6374 | 0.5539 | 0.0133 | 0.0128 | 0.0780 | 0.12 | 0.0446 | 0.08 |
| 3 | 16 | TUDr | None | −0.0375 | −0.0004 | 0.6442 | 0.5556 | −0.0002 | 0.0000 | 0.0710 | 0.11 | 0.0713 | 0.13 |
| 3 | 10 | UDN | None | −0.0381 | −0.0002 | 0.6412 | 0.5538 | 0.0000 | 0.0001 | 0.0340 | 0.05 | 0.0344 | 0.06 |
| 3 | 5 | URS1 | None | −0.0412 | −0.0288 | 0.6264 | 0.5295 | −0.0052 | −0.0024 | 0.0580 | 0.09 | 0.0559 | 0.10 |
| 4 | 19 | ESI | None | −0.0431 | 0.0019 | 0.6716 | 0.5669 | −0.0064 | 0.0021 | 0.2831 | 0.44 | 0.1791 | 0.32 |
| 4 | 9 | OSAK | None | −0.0344 | 0.0005 | 0.6447 | 0.5567 | 0.0023 | 0.0007 | 0.0850 | 0.13 | 0.0807 | 0.15 |
| 4 | 22 | TAMU | X:4–124 | −0.0406 | 0.0006 | 0.6530 | 0.5724 | −0.0002 | 0.0005 | 0.6444 | 1.00 | 0.3614 | 0.65 |
| 4 | 6 | URS2 | None | −0.0381 | −0.0001 | 0.6399 | 0.5548 | 0.0006 | −0.0002 | 0.0406 | 0.06 | 0.0591 | 0.11 |
| 4 | 8 | VKI | None | −0.0369 | 0.0003 | 0.6491 | 0.5604 | −0.0003 | 0.0007 | 0.1027 | 0.16 | 1.1073 | 2.00 |
| 4 | 20 | YA-IN | None | −0.0360 | −0.0005 | 0.6396 | 0.5502 | 0.0006 | 0.0000 | 0.0410 | 0.06 | 0.0399 | 0.07 |

[a] Border correction: for some contributors, it was necessary to remove one line or column near the border to get correct statistics

red structures are visible, where the displacement in x-direction is calculated too large. These structures can also be observed in the fields of ILA, TSI and UDN. If we recall Fig. 25, these structures appear at positions, where the product $F_I F_O F_\Delta$ changes significantly. The deviation fields of IOT and URS1 show a clear peak locking. Here, an area of underestimated displacements is followed by an area of overestimated displacements. With the exception of YATS and URS2, the PTV teams have provided noisy fields with singular very large deviations to the exact solution.

These results can be found quantitatively in Fig. 27, where the RMS values of the displacement in x-direction calculated by means of all valid vectors are shown.

The effect of the decreasing signal to noise ratio can clearly be seen in these graphs. While the RMS increases only slightly for some of the teams (e.g. DLR, LAVIS), a strong increase can be observed for some of the PTV teams (consider the different axis scaling for group 4). The main

reason for the large RMS of these PTV teams was found to be the large number of spurious vectors. It must be mentioned here that for UDN, the first three images of case B where processed with the THMA approach while the last three with the local approach (the inverse would have been better).

This is shown in Fig. 28, where the valid vector rates stated by the teams (left hand side) and calculated by the criteria $|\Delta x'| < 0.5$ px and $|\Delta y'| < 0.5$ px are shown. This threshold is feasible because the main peak of the PDF of $\Delta x'$ and $\Delta y'$ is covered by this permitted deviation.

The vectors determined by the shown PTV teams are specified to be valid. Applying the mentioned criteria, it can clearly be seen that the number of spurious vectors is, even for a good SNR, large for the evaluations from ESI and OSAK. With decreasing SNR, the number of spurious vectors increases significantly for most of the PTV teams.

In Fig. 29 on the left hand side the PDF of $\Delta x'$ of three teams are shown for the time-steps 30 (solid lines) and 90
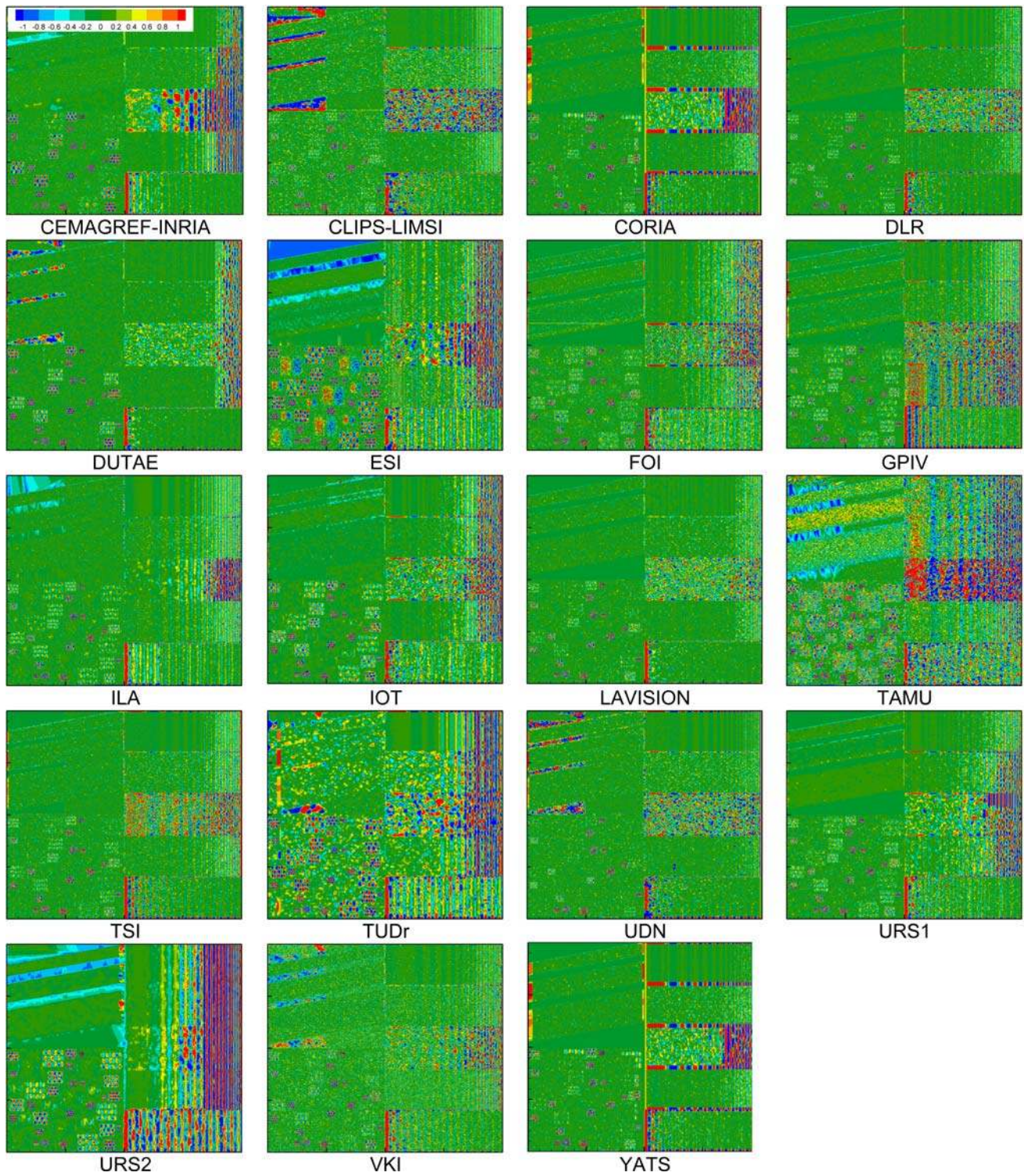
**Fig. 19** Difference (in pixels) between the measured value and the exact value of the *V*-component

(dashed lines). The growing peak width with increasing noise can be observed clearly. For all teams, the curves are nearly symmetric and they decay with increasing $|\Delta x'|$. At $|\Delta x'| = 0.2$ px the values are quite small which confirms the choice of the threshold value of 0.5 px deviation. In Fig. 29, on the right hand side, the total RMS value of the displacement $\Delta x$ has been re-calculated by only considering vectors with a deviation to the exact solution of $|\Delta x'| < 0.5$ px and $|\Delta y'| < 0.5$ px. By comparison with Fig. 27 a strong increase in accuracy can be observed.
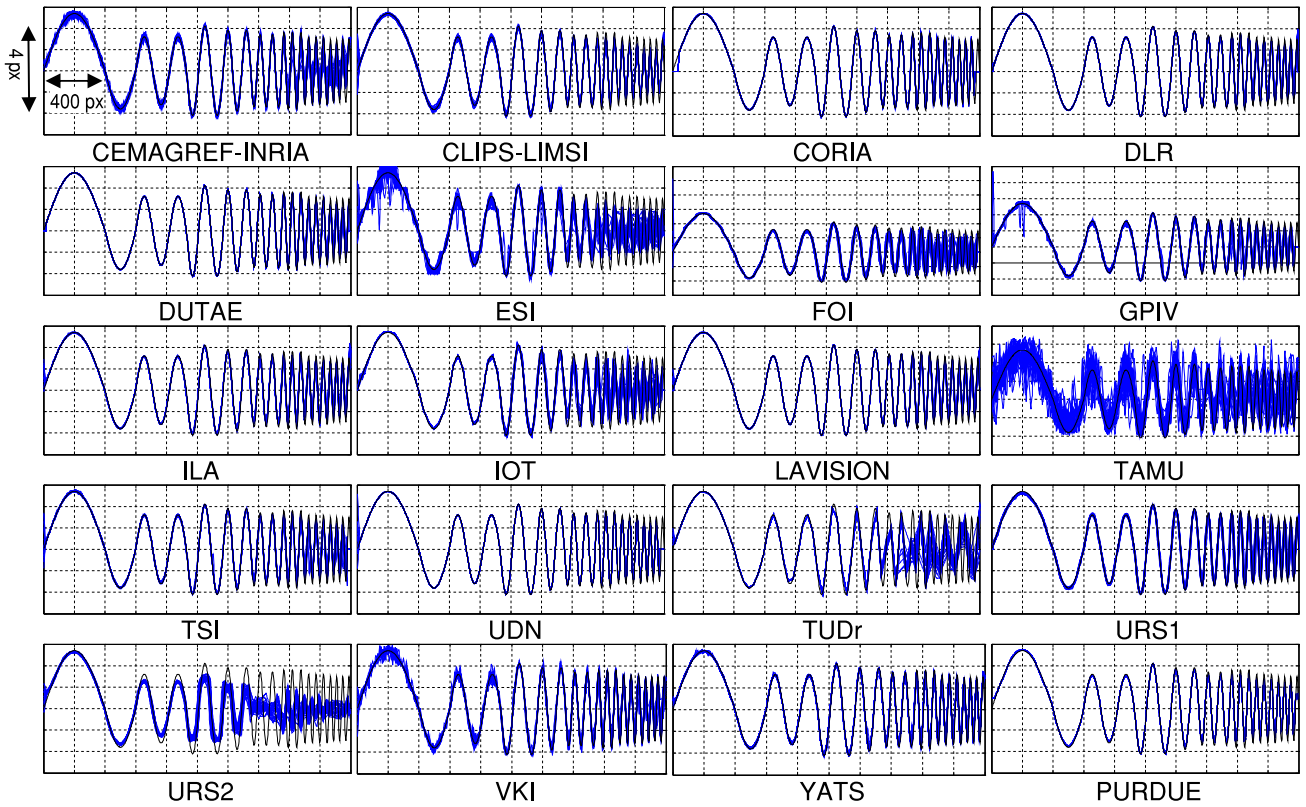
**Fig. 20** Exact (*solid black*) and measured vertical displacement (*solid blue*). *Vertical axis* ticks spacing: 1 px. *Horizontal axis* ticks spacing: 200 px
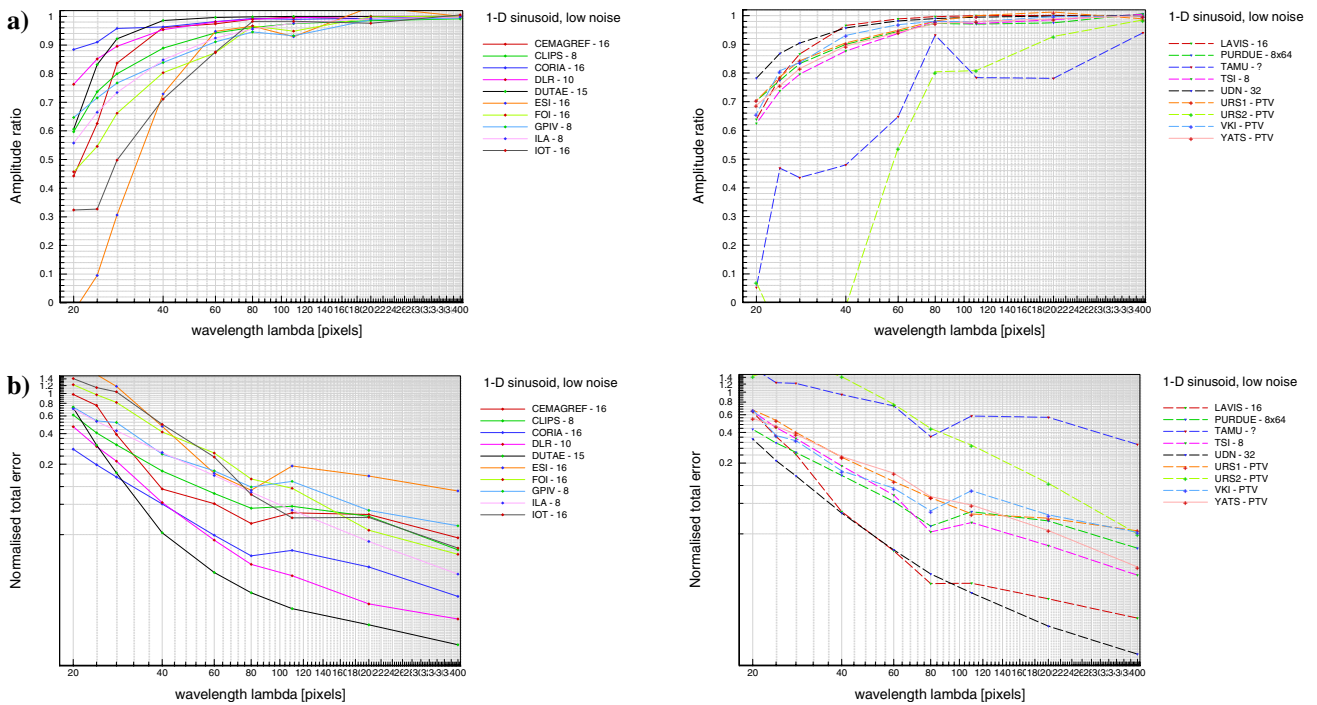


**Fig. 21 a** Normalized amplitude response to a 1-D sinusoidal displacement (low noise), **b** normalized total error (amplitude modulation + rms error)

**Table 13** One-dimensional sinusoid (no noise)

| Modulation error cut-off | | Total error cut off | |
|---|---|---|---|
| Group | $\Lambda_{co-10\%}$ (px) | Group | $\Lambda_{ERR-20\%}$ |
| CORIA | 22 | CORIA | 24 |
| DUTAE | 27 | UDN | 25 |
| UDN | 28 | DUTAE | 27 |
| DLR | 29 | DLR | 29 |
| LAVIS | 32 | LAVIS | 30 |
| CEMAGREF | 34 | PURDUE | 33 |
| VKI | 36 | CEMAGREF | 34 |
| URS1 | 39 | CLIPS | 36 |
| PURDUE | 40 | VKI | 36 |
| YATS | 42 | TSI | 39 |
| CLIPS | 44 | URS1 | 44 |
| TSI | 47 | YATS | 47 |
| ILA | 53 | ILA | 49 |
| ESI | 55 | GPIV | 52 |
| GPIV | 56 | ESI | 56 |
| IOT | 64 | IOT | 64 |
| FOI | 65 | FOI | 68 |
| TAMU | >100 | TAMU | >100 |
| URS2 | >100 | URS2 | >100 |

**Table 14** Two-dimensional sinusoid (20% noise)

| Modulation error cut-off | | Total error cut off | |
|---|---|---|---|
| Group | $\Lambda_{co-10\%}$ (px) | Group | $\Lambda_{ERR-20\%}$ |
| UDN | 33 | UDN | 28 |
| DUTAE | 36 | DUTAE | 32 |
| CORIA | 38 | DLR | 33 |
| LAVIS | 39 | LAVIS | 34 |
| DLR | 41 | PURDUE | 36 |
| CLIPS | 48 | CORIA | 36 |
| VKI | 52 | TSI | 48 |
| PURDUE | 52 | ILA | 48 |
| TSI | 52 | CLIPS | 48 |
| ILA | 52 | VKI | 50 |
| URS1 | 52 | YATS | 50 |
| FOI | 52 | CEMAGREF | 56 |
| CEMAGREF | 54 | URS1 | 57 |
| YATS | 54 | IOT | 68 |
| IOT | 68 | GPIV | 70 |
| TAMU | 68 | FOI | 80 |
| GPIV | 80 | URS2 | 96 |
| URS2 | 100 | ESI | >100 |
| ESI | >100 | URS2 | >100 |

Nevertheless, many teams with cross-correlation analysis achieve better results without the post-processing applied by the authors.

## 5.2 Evaluation of case B2

The evaluation of B2 was also done at time-steps 10, 30, 50, 70, 90 and 110. In opposition to B1, the images $n - 9 \ldots n + 9$ could be considered to increase the accuracy. The motivation of this approach can be found in (Hain and Kähler 2007 or Kähler and Kompenhans 2000). The contributors, which participated in this test case, are given in Table 16.

The exact locations of the grid points are:

$X = 24 \ldots 1416$   88   Nodes
  (grid distance   $x = 16$ pixel)

$Y = 24 \ldots 664$   41   Nodes
  (grid distance   $y = 16$ pixel)

Three teams could increase the accuracy significantly by using the images around time-step $n$. In Fig. 30 the deviations of the displacements in $x$-direction to the exact solution are shown. On the left hand side evaluation B1 is shown and on the right hand side evaluation B2 is given accordingly (both for time-step $t = 110$).

The deviations to the exact solution can strongly be reduced by the advanced evaluation algorithms of DUTAE and DLR. The algorithm of LAVIS leads to a field with a very low level of the noise.

DLR applies an algorithm which calculates at first intermediate vector fields $v_i$ by means of cross correlation of the given images $n_i$ after the following equation: $v_{t+i} = n_{t+i-2} \otimes n_{t+i+2}$ with $t$ being the time-step for which the vector field is determined and $i$ being a variable with values $i = -2 \ldots + 2$. A weighted averaging of the vector fields $v_{t-2} \ldots v_{t+2}$ leads to the final vector field at time-step $t$. DUTAE performs a correlation between the image $n$ and $n + 5$ for the observation interval $n - 10 \ldots n + 10$. The time data regression is done by means of a 2nd order least squares fit of the local velocity vector. LAVISION developed an algorithm to determine the optimum temporal distance between the correlated images at each vector position. Therefore the following correlations are done at first: $n - 9 \otimes n - 8, n - 8 \otimes n - 7, \ldots, n + 8 \otimes n + 9$. In this case the temporal separation between the images is d$n = 1$. The determined displacements $\Delta x$ and $\Delta y$ are plotted versus the time and for both $\Delta x$ and $\Delta y$ a straight line is fitted. The deviations of the vector components to the lines are calculated and combined to one residual. In addition, the displacements for image $n$ are determined from the fits. d$n$ is now increased by 1 so that the correlations are done as follows:   $n - 9 \otimes n - 7, n - 8 \otimes n - 6, \ldots, n + 7 \otimes n + 9$. Straight lines are fitted again, the residual is determined, and the displacements are calculated. If the residual at d$n = 2$ is smaller than that at d$n = 1$, d$n$ is increased by 1. Otherwise the old d$n$ is the optimum and the velocity
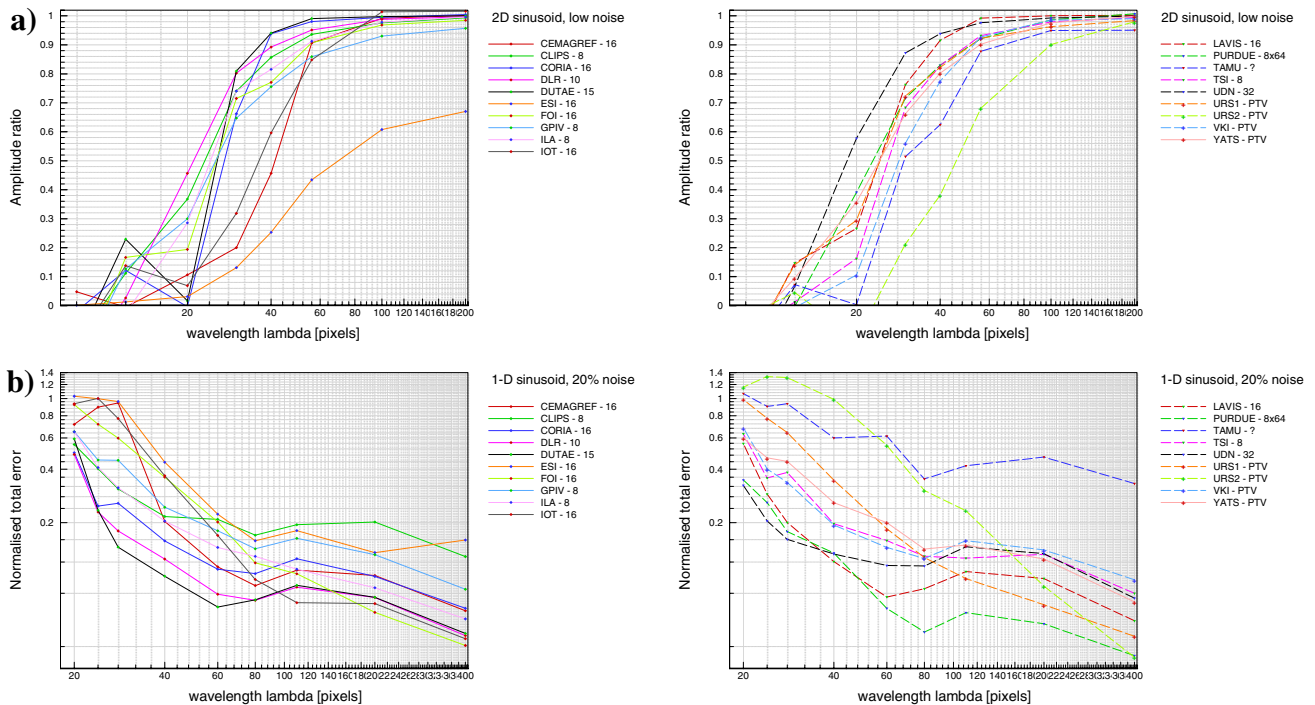
**a)**



**b)**



**Fig. 22 a** Normalized amplitude response to a 2-D sinusoidal displacement, **b** normalized total error (modulation + rms uncertainty)



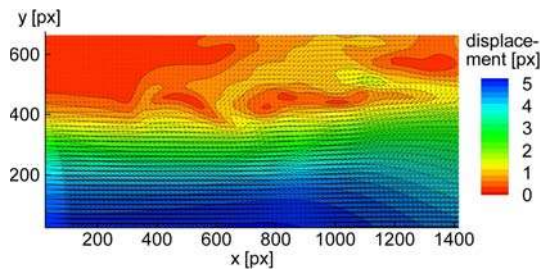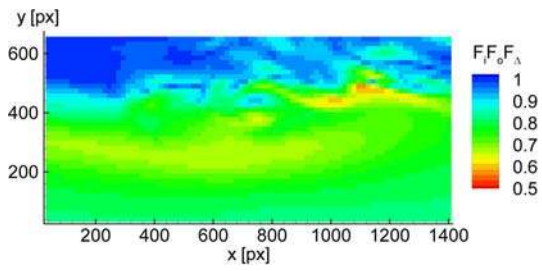**Fig. 23** Instantaneous velocity vector field of case B



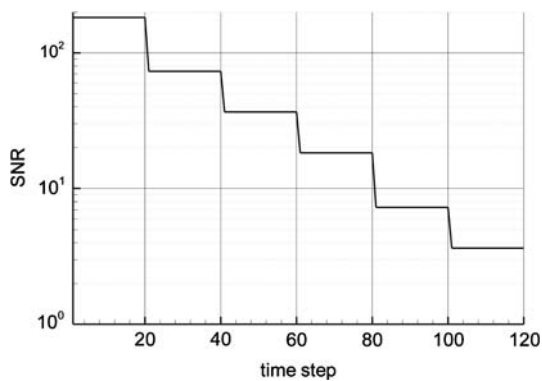**Fig. 25** Visualization of the product $F_I F_O F_\Delta$

Figure 31 on the right hand side shows by comparing with Fig. 27 that many teams cannot at all or only slightly reduce the RMS by taking the surrounding images into account. However, the algorithm from LAVIS leads to a RMS which is nearly independent from the SNR which demonstrates the potential of this approach.

### 5.3 Conclusions for Case B

Case B gives information about the precision of the evaluation algorithms in dependency on the signal to noise ratio. The effect of the SNR on the accuracy can clearly be seen in the analysis. On average, the PIV and OF algorithms lead to more accurate evaluations compared to the PTV algorithms. However, one problem of the PTV algorithm was found to be the large number of spurious vectors which can be reduced by applying better post-processing



**Fig. 24** Dependence of the signal to noise ratio on the time-step

components at a given vector position are determined based on this d$n$. The method is continued to a maximum d$n = 9$. A comparison between evaluations B1 and B2 is done for the discussed three teams in Fig. 31 on the left hand side.

**Table 15** Contributors of case B1 and parameter for the displacement estimation

| Team | Method | IW-size | Fit | Iterations |
|---|---|---|---|---|
| CORIA | PIV | 32 | 3 Point Gauss | 2 |
| DLR | PIV | 32 | 2D least-square | 6 |
| DUTAE | PIV | – | | |
| FOI | PIV | 32 | 3 Point Gauss | 2 |
| GPIV | PIV | 32 | 3 Point Gauss | 3 |
| ILA | PIV | 32 | Whittaker | 8 |
| IOT | PIV | 32 | 3 Point Gauss | 3 |
| LAVIS | PIV | 32 | 3 Point Gauss | 4 |
| TSI | PIV | 32 | 3 Point Gauss | 4 |
| TUDr | PIV | 16 | 2D least-square | 10 |
| UDN | PIV | 32 | 3 Point Gauss | 52 |
| URS1 | PIV | 32 | 3 Point Gauss | 7 |
| ESI | PTV | 10 | Laplacian centroid location | |
| YATS | PTV | 31 | | 13 |
| OSAK | PTV | 32 | Gauss | |
| TAMU | PTV | 15 × 4 | 3 Point Gauss | |
| URS2 | PTV | 16 | 3 Point Gauss | 12 |
| VKI | PTV | 12 | Gauss | |
| CEM-IN | OF | 16 | | 6 |
| CLI-LI | OF | 8 | Sub-pixel max | 24 |
| CORIA | PIV | 32 | 3 Point Gauss | 2 |

methods. The evaluation B2 showed the possibility of using the whole image sequence to increase the accuracy. As a result of Case B, the teams can be arranged into three groups:

1. DLR, DUTAE, YATS, LAVIS
2. CORIA, FOI, ILA, IOT, TSI, URS1, URS2
3. CEMAGREF-INRIA, CLIPS-LIMSI, ESI, GPIV, OSAK, TAMU, TUDr, UDN, VKI

## 6 Case C

This test case was designed to evaluate the performances of the algorithms on real images from a high speed PIV experiment. The flow was a nitrogen at a velocity of the order of 30 m/s. The nozzle diameter was 5 mm. The tracers used were oil-mist particles with an average size of the order of 5μm. A New Wave Pegasus laser was used for illumination (Nd:YLF, 527 nm, ~1 mJ@2 × 5 kHz), and a Photron APX-RS camera (512 × 512 px @10 kfps, 8 bits) for recording. The viewing area was 29 × 29 mm$^2$. The Frame Straddling technique was used by means of a Digital Delay Generator. The odd/even time separation was 10 μs, the even/odd: 190μs. A set of

100 contiguous image pairs were provided, corresponding to 20 ms of recording. Figure 32 gives an example of PIV image obtained. The interpretation of this test case was fairly limited as the particle concentration was relatively low, the particle images were small and the contributors did not make benefit of the time series in their analysis. The results are thus not discussed here but can be found on the challenge website (http://www.pivchallenge.org).

## 7 Case D

Four sets of synthetic images were provided as case D to assess the accuracy and robustness of the stereo PIV algorithms. These images were generated using the EuroPIV2 SIG as in case A, but in a stereoscopic configuration. As this was the first assessment of stereo PIV algorithms in the challenge, it was decided to investigate here the robustness of these algorithms to misalignment of the recording set-up. Consequently, Case D1 is a reference case with ideal working conditions. Cases D2 to D4 were designed to test different misalignments: in D2, the light sheet does not coincide with a calibration target position, in D3, the optical axis is on the border of the field of view and in D4, the two optical axis do not intersect and are not exactly in a plane. As the results from these last three test cases bring more ore less to the same conclusions, only the most severe one: case D4 will be discussed here, together with the reference case D1. The optical set-up is described in Fig. 33 and the values of the parameters are given in Tables 17 and 18, respectively for cases D1 and D4. Table 19 gives the misalignments between the two test cases. Both cameras are set in Scheimpflug conditions, on the same side of the laser sheet, with a symmetric angle of the order of 45° with respect to the normal to the laser sheet plane. The difference in light scattering between the two directions of observation is not taken into account.

In the configuration of Fig. 33, optical axes and laser sheet plane intersect at the origin (0,0,0). On the left image, a small right part is only viewed by left camera (and vice versa on the right image). In order to have both fields that overlap ideally, laser sheet is shifted in the z direction by a positive amount. This amount for the present reference configuration is 0.003527 m. The common field of view is 0.120 mm in width (along $X$ axis) and 0.090 mm in height (along $Y$ axis).

The calibration grid is a rigid plane with markers [either crosses (e.g. Fig. 34) or gaussian dots]. The markers are laid on a regular grid with a spacing of 5 mm in $X$ and $Y$ directions. A few markers differ by their brightness (darker or brighter), in order to locate both the origin of the axes (at
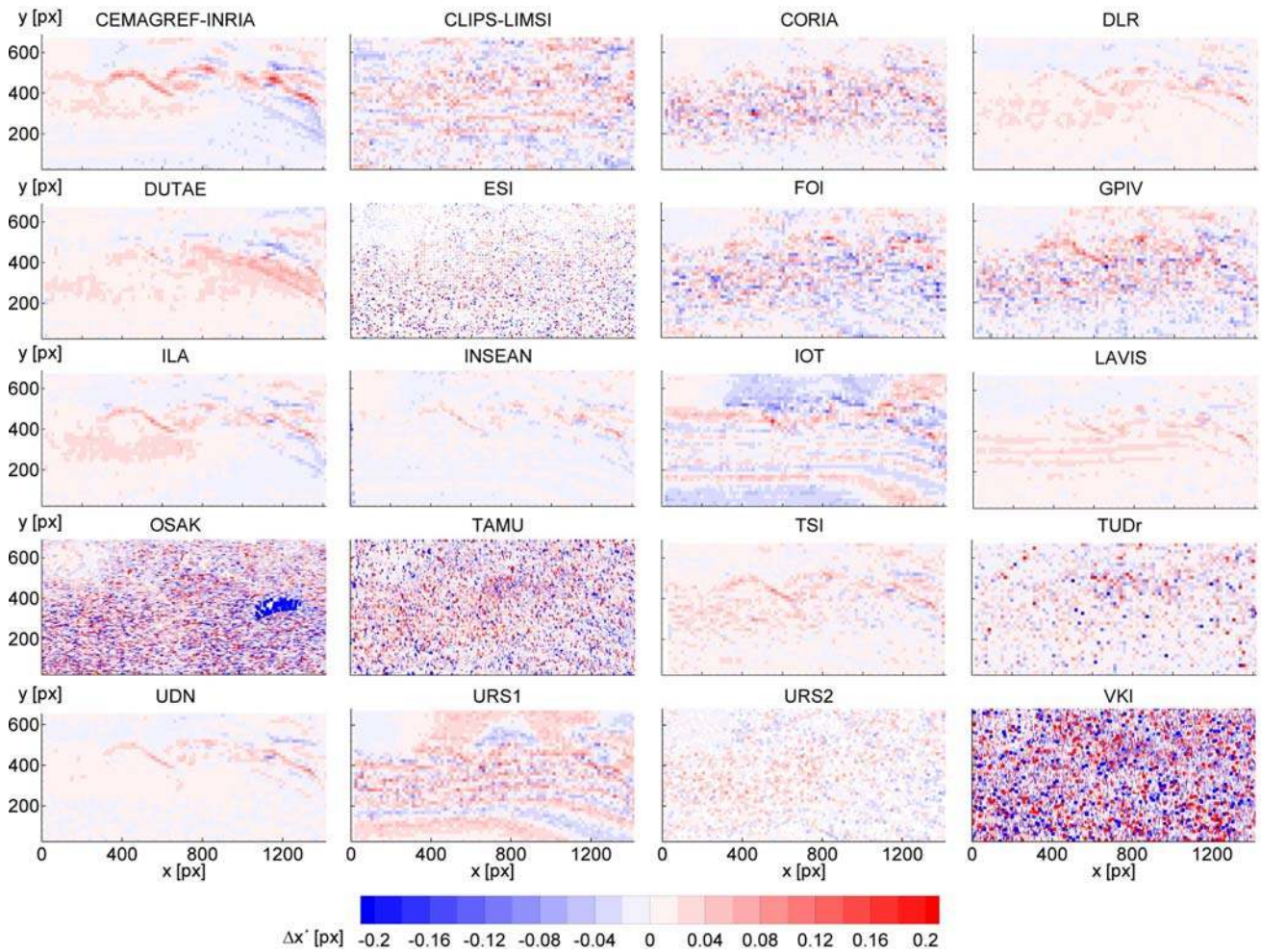
**Fig. 26** Deviations of the displacements in x-direction $\Delta x' = \Delta x_{\text{contributor}} - \Delta x_{\text{exact}}$ for time-step $t = 10$
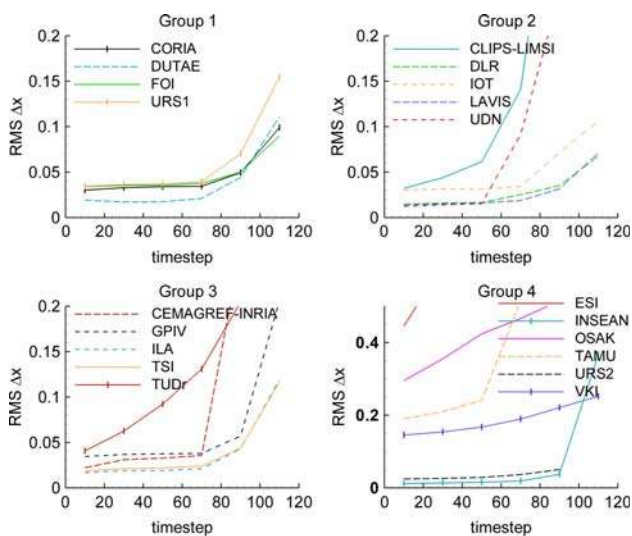


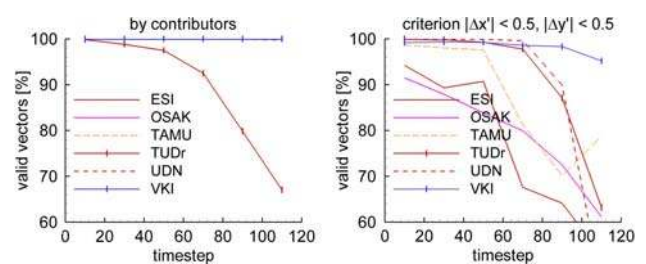**Fig. 27** Dependence of the RMS of the x-displacement on the time-step (SNR)



**Fig. 28** Valid vector rate stated by the contributors (*left hand side*) and calculated by the criteria $|\Delta x'| < 0.5$ px and $\Delta y'| < 0.5$ px (only for some selected teams)

the center of the plate) and the approximate limits of the common field of view.

Displacement components are named $U, V$ and $W$ along $X, Y$ and $Z$ axes, respectively. The displacement field is given as:
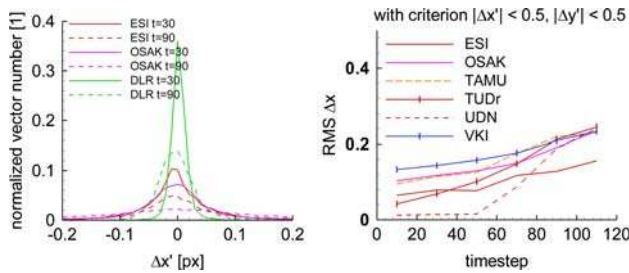
**Fig. 29** Comparison of the PDF of $\Delta x'$ for three teams for the time-steps 30 and 90 (*left hand side*) and the total RMS after removing spurious vectors (*right hand side*)



**Fig. 31** Dependence of the RMS of the *x*-displacement on the time-step (SNR). *Left hand side*: Comparison between evaluation B1 and B2 for DLR, DUTAE and LAVIS. *Right hand side*: evaluation B2 of the other teams
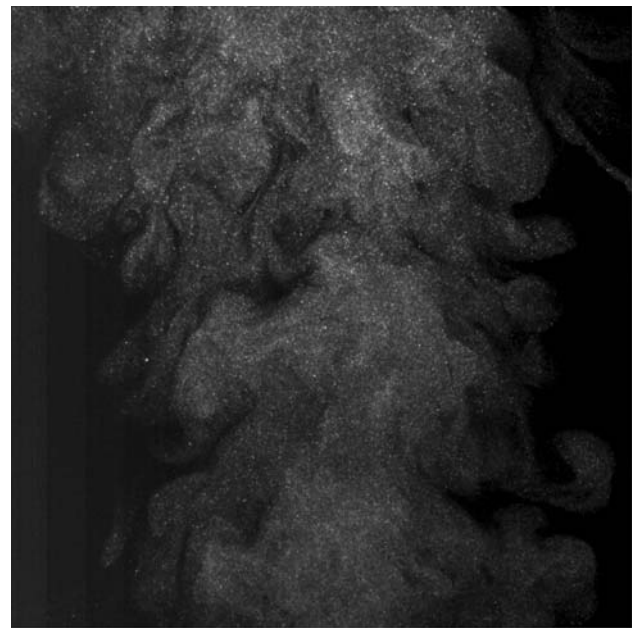
**Table 16** Contributors of case B2 and parameter for the displacement estimation

| Team | Method | IW-size | Fit | Iterations |
|------|--------|---------|-----|------------|
| CORIA | PIV | 32 | 3 Point Gauss | 20 |
| DLR | PIV | 32 | 2D least-square | 8 |
| DUTAE | PIV | 31 | 3 Point Gauss | 6 |
| ILA | PIV | 32 | Whittaker | 8 |
| IOT | PIV | 32 | 3 Point Gauss | 3 |
| LAVIS | PIV | 32 | 3 Point Gauss | 4 |
| URS1 | PIV | 64 | 3 Point Gauss | 7 |
| YATS | PTV | 31 | | 7 |
| CLI-LI | OF | 8 | Sub-pixel max | 24 |



**Fig. 32** Sample $512 \times 512$ px image from case C (HSPIV). Upward jet flow at 30 m/s, field of view $29 \times 29$ mm$^2$, framing rate 10,000 fps



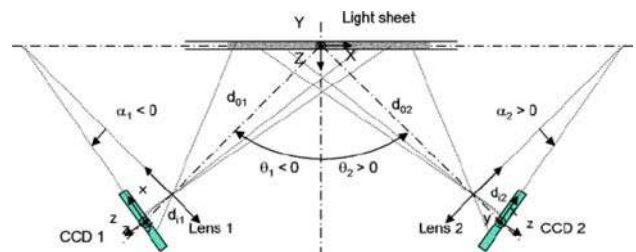**Fig. 33** Recording set-up for the generation of the synthetic images for case D



**Fig. 30** Comparison between evaluations B1 and B2 for the deviations of the displacements in *x*-direction (time-step $\tau = 110$)

**Table 17** Recording parameters for case D1

| Camera | $\theta(°)$ | $\alpha(°)$ | do(m) | di(m) | Pixel size (μm) |
|--------|-------------|-------------|-------|-------|------------------|
| Left | −45 | −5.71 | 1 | 0.1 | 10 |
| Right | +45 | 5.71 | 1 | 0.1 | 10 |

**Table 18** Recording parameters for case D4

| Camera | $\theta(°)$ | $\alpha(°)$ | do(m) | di(m) | Pixel size (μm) |
|--------|-------------|-------------|-------|-------|-----------------|
| Left   | −47.46      | −5.71       | 1     | 0.1   | 10              |
| Right  | +47.46      | 5.71        | 1     | 0.1   | 10              |

**Table 19** Recording configuration misalignment between D4 and D1

| Axis | $x$ | $y$ | $z$ |
|------|-----|-----|-----|
| Translation (m) | 0.001 | 0.001 | 0.0008 |
| Rotation (°) | 1.123 | 2.456 | 0.789 |

$$\vec{V} = U.\vec{i} + V.\vec{j} + W.\vec{k},$$

with

$$U = c + u_1,$$

$$V = s.x + g + u_2,$$

$$W = a.\sin(2\pi.w.x + p) + u_3,$$

and

$$u_i = a_i \left( \sum_{j=1}^{n} \sin(2\pi.w_j.x + p_{ix}) + \sum_{j=1}^{n} \sin(2\pi.w_j.y + p_{iy}) \right)$$



**Fig. 34** Calibration target used for case D

$c$, $s$, $g$, $a$, $a_i$ and $n$ are constants given in Table 20 for cases D1 and D4. The wavelength $w$ is also given in Table 20. The wavelengths $w_j$ are given as $L/j$ where $L$ is the field height (along the $Y$ axis). The phases $p$, $p_{ix}$ and $p_{iy}$ are given in Table 20. Figure 35 gives as an example the velocity components generated with these equations for case D1. This velocity field does not satisfy the Navier–Stokes equations but it is analytic and complex enough not to be guessed.

For each case, 3 sets of images are provided:

- 11 image pairs for calibration (Table 21). These are images of the target of Fig. 34 with crosses or dots.
- 60 image pairs for misalignment correction. These are first exposure SPIV images from both cameras.
- 1 set of double image pairs for the measurement.

The images from each camera are 1,024 × 1,024 $px^2$ × 8 bit, in TIF format. The particle image diameter is of the order of 3 px. The particle image density is of the order of 0.06 particle/$px^2$ (that is about 15 particles in a window of 16 × 16 px). Figure 36 gives a representative example of particle image for this case.

Only 7 teams among the 22 contributors did analyse case D. Table 22 gives the main characteristics of the reconstruction algorithms used by these teams. Image mapping projects the images from the two cameras in the object space and performs the PIV analysis on these projected images. Vector warping performs the PIV analysis in the camera image plane and projects the displacements in the object space. In both cases, the stereo reconstruction is performed in the object space, based on displacement fields from the two cameras and using a stereo model. The Soloff method (Soloff et al. 1997) performs the PIV analysis in the camera image planes and the projection and stereo reconstruction at the same time. As can be seen from Table 22, all these methods are represented. As the PIV processing is now iterative, the stereo reconstruction can be integrated in this iterative procedure (simultaneous) or not (separate). As 11 positions of the calibration grid were provided, the contributors could use as much as they want
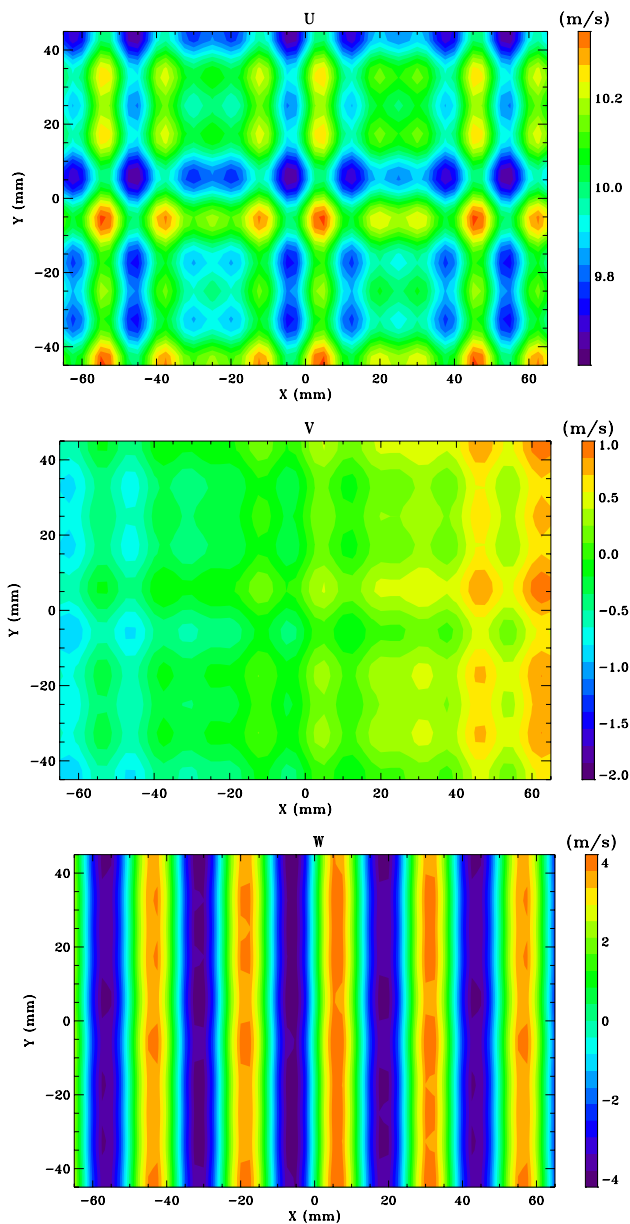
**Table 20** Displacement parameters for case D

| Case | $c$(m) | $s$ | $g$(m) | $a$(m) | $w$(m) | $p$(rad) | $L$ | $n$ | $a_i$(m) | $p_{ix}$(rad) | $p_{iy}$(rad) |
|------|--------|-----|--------|--------|--------|----------|-----|-----|----------|---------------|---------------|
| D1 | 0.001 | 0.001 | 0.000 | 0.0004 | 0.025 | 0.000 | 0.100 | 4 | 0.00001 | 0.000 | 0.000 |
| D2 | 0.001 | 0.001 | 7.89E-5 | 0.0004 | 0.025 | 0.987 | 0.100 | 4 | 0.00001 | 0.789 | 0.987 |

**Table 21** Calibration target position for case D

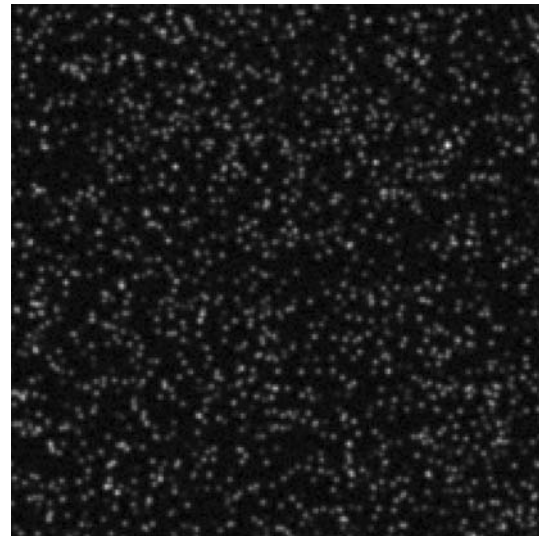| Index | 000 | 001 | 002 | 003 | 004 | 005 | 006 | 007 | 008 | 009 | 010 |
|-------|-----|-----|-----|-----|-----|-----|-----|-----|-----|-----|-----|
| z position (mm) | −2.5 | −2.0 | −1.5 | −1.0 | −0.5 | 0.0 | 0.5 | 1.0 | 1.5 | 2.0 | 2.5 |

**Fig. 35** Velocity field for case D1



**Fig. 36** Sample of PIV image from case D1, $200 \times 200$ px$^2$

details were obtained by plotting maps of the error for each contributor. They are not reproduced here. Only a few samples will be given with case D4 to explain the results obtained. To illustrate the results of Table 23, Figs. 37 and 38 give the bias and the RMS error on the three velocity components for the different contributing teams. A first remark is that the mean values of the three components of the displacement are fairly well retrieved, with several teams within 1% of the modulus of the mean velocity (10 m/s) for each of them (only DUTAE is within 1% for all components and Lavision nearly). The situation is not the same for the RMS values. The RMS of $U$ is poorly assessed, while that of $V$ and $W$ are more reasonable. This can be attributed to two facts: the dynamics of $U$ is much larger than that of the two other components. As the sample is small (one record averaged along $X$ and $Y$), the convergence is probably not so good, the $V$ component is the component which is not reconstructed in this set-up so reconstruction errors do not add up.

Looking at the bias and RMS error, the bias confirm the previous remarks on the mean velocity, several teams are below 1%. The RMS error clearly shows the difference between the two reconstructed components ($U$ & $W$) and the direct one ($V$). Globally, it can be said that at least 3 teams with different algorithms (CORIA, DUTAE & IOT) perform very well both on bias and RMS. This means that the stereo algorithm used does not make a difference if it is calibrated properly.

Table 24 and Figs. 39 and 40 give the same results for case D4. Globally, the conclusions are comparable to case D1 (and D2–3). Several teams perform very well, both on the mean and RMS (CORIA, DUTAE, IOT, Lavision), which means that the stereo algorithms are able to cope with a certain degree of misalignment at recording, if

to calibrate their mapping function. They could also use different polynomial orders for this mapping or different models (pin hole). Finally, as 60 first exposure image pairs were provided, they could use as much as they needed (up to 60) to compute the disparity maps allowing to correct the mapping.

Table 23 gives the mean and RMS values of the three velocity components, averaged over the whole velocity field for case D1. Also, in this table are given the bias and RMS errors. As these are stereo reconstructed data, they are given in m/s (the magnification is not constant over the field of view so it is difficult to convert in pixels). This gives a global indication of the quality of the results. More

**Table 22** Main characteristics of the algorithms used by the contributors for case D

| Contributor | Image mapping | Vector warping | Soloff | Simul/sep | No. of calb. grids | Poly. order | Disparity map |
|---|---|---|---|---|---|---|---|
| CLIPS LIMSI | | x | | Simul. | 1 + focal length + px size | Pin hole | x |
| CORIA | | x + proj. grid | | Sep. | 5 | pin hole | 50 |
| DLR | x | | | Sep. | 5 | 1st/1st | 1 |
| DUTAE | x + 1 step | | | Simul. | 2 | 3rd &1st | x |
| ILA | | | x | Sep. | 3 | 2nd & 1st | 1 |
| IOT | | | x + resampl. | Sep. | 3 | 3 | 100 |
| LAVIS | x + 1 step | | | Simul. | 5 | Pin hole | 100 (1) |
| TSI | | | x | Sep. | 11 | 3rd&1st | 100 |



**Fig. 37** Bias error for case D1
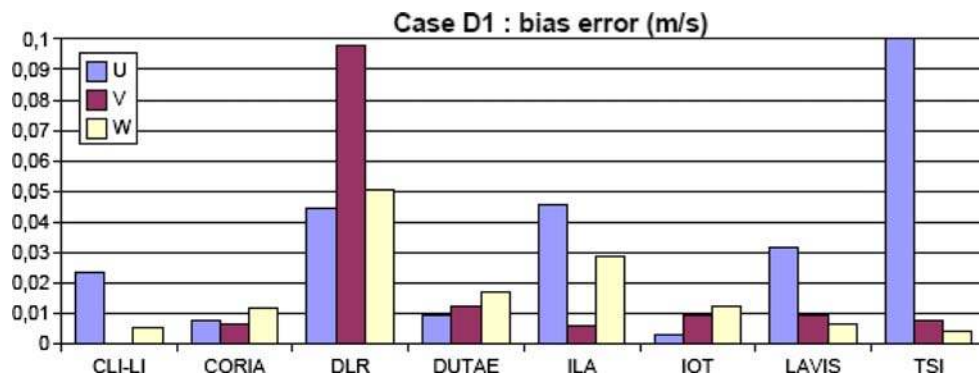


**Fig. 38** RMS error for case D1
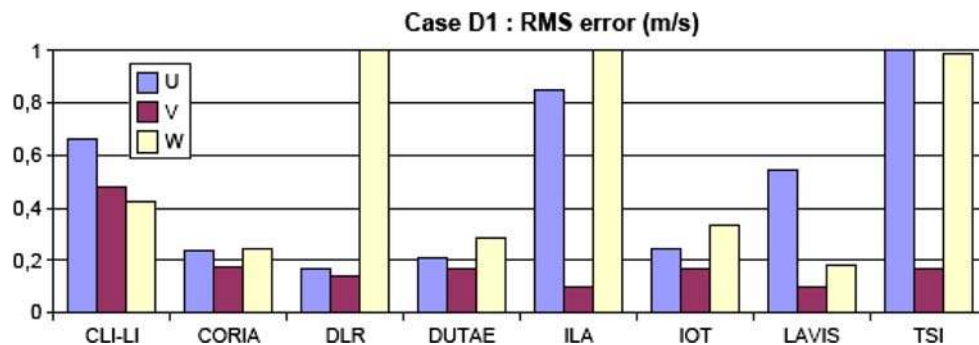
calibration is performed properly (notably by recording several calibration target positions). This again is independent of the stereo reconstruction method used. This result is confirmed by Fig. 41 which gives, as an example, the RMS error on the $U$ component for the four D cases and for the different teams.

As mentioned above, in order to push further the investigation, maps of the error were plotted for the three velocity components and for each contributing team. For space reason, they are not reproduced here but are available on the challenge web site. Figure 42 gives some examples of such maps for the W (out of plane) component for case D4. It can be observed that CLIPS-LI shows mostly a random error due to the PIV processing. IOT results exhibit a more coherent error linked to the shape of the W component and which was identified as due to a stereo reconstruction error. TSI, evidence both types of error, while DLR was able to properly process and calibrate in this case. As can be seen, it was thus fairly easy to identify the origin of the error for each contributor and the conclusion is that to obtain good results, both the PIV processing and the stereo calibration and reconstruction have to be performed carefully. If this is the case, and whatever the stereo algorithm used, the accuracy obtained is that of the PIV processing. The stereo reconstruction does not bring errors larger than that for the moment. Additionally, a careful analysis of the results did show that the use of advanced algorithms with image deformation is bringing a slight improvement. The fact that both PIV processing and stereo reconstruction are performed simultaneously does not bring evident improvement on the accuracy point of view.

**Table 23** Mean and RMS velocity, bias and RMS error for case D1

| Contributors | Velocity U Mean | U RMS | V Mean | V RMS | W Mean | W RMS | Error U Bias | U RMS Absolute | U RMS Relative (%) | V Bias | V RMS Absolute | V RMS Relative (%) | W Bias | W RMS Absolute | W RMS Relative (%) |
|---|---|---|---|---|---|---|---|---|---|---|---|---|---|---|---|
| Reference | 10.0000 | 0.1457 | 0.0000 | 0.4162 | 0.0000 | 2.7723 | | | | | | | | | |
| CLI-LI | 10.0236 | 0.6528 | 0.0000 | 0.6417 | 0.0054 | 2.9121 | 0.0236 | 0.6616 | 6.6 | 0.0000 | 0.4810 | 48.1 | 0.0054 | 0.4277 | 10.7 |
| CORIA | 9.9918 | 0.2752 | −0.0014 | 0.4503 | 0.0355 | 2.7656 | −0.0079 | 0.2349 | 2.3 | −0.0066 | 0.1764 | 17.6 | 0.0118 | 0.2446 | 6.1 |
| DLR | 9.9979 | 0.1739 | −0.0024 | 0.4457 | 0.0030 | 2.6999 | −0.0018 | 0.1061 | 1.1 | −0.0026 | 0.0687 | 6.9 | 0.0033 | 0.2563 | 6.4 |
| DUTAE | 10.0114 | 0.2463 | −0.0087 | 0.3373 | 0.0031 | 2.8997 | 0.0097 | 0.2065 | 2.1 | −0.0123 | 0.1652 | 16.5 | 0.0173 | 0.2886 | 7.2 |
| ILA | 10.0409 | 0.8494 | −0.0063 | 0.3929 | −0.0341 | 2.4408 | 0.0459 | 0.8511 | 8.5 | −0.0063 | 0.0945 | 9.4 | −0.0291 | 1.1844 | 29.6 |
| IOT | 9.9970 | 0.2786 | −0.0098 | 0.4724 | 0.0123 | 2.6143 | −0.0029 | 0.2447 | 2.4 | −0.0097 | 0.1657 | 16.6 | 0.0123 | 0.3349 | 8.4 |
| LAVIS | 9.9963 | 0.1948 | −0.0103 | 0.3601 | −0.0110 | 2.7540 | −0.0320 | 0.5452 | 5.4 | −0.0095 | 0.1008 | 10.1 | −0.0069 | 0.1824 | 4.6 |
| TSI | 9.2944 | 2.6060 | 0.0072 | 0.4145 | 0.0156 | 2.4002 | −0.7076 | 2.6016 | 26.0 | 0.0076 | 0.1679 | 16.8 | 0.0043 | 0.9903 | 24.8 |

## 8 Case E

The last test case provided corresponds to a real experiment of Stereo PIV. This experiment was performed at TU Delft, in the laboratory for Aero & Hydrodynamics. Measurements were done in a pipe flow facility with an inner diameter of 40 mm and a total length of 28 m. A detailed description of the flow facility is given by Draad and Nieuwstadt (1998). The working fluid is water, and the flow can be kept laminar up to $Re = 60 \times 10^3$. All measurements were carried out at 26 m from the inlet. A detailed description of the flow facility and of PIV measurements in laminar and turbulent pipe flow is given by van Doorne and Westerweel (2007).

A sketch and a photograph of the experiment are given in Fig. 43. The PIV images were recorded with two Kodak ES 1.0 cross-correlation cameras, which operate at 15 Hz and give 8-bit images of 1,008 × 1,008 px. Both cameras look at an angle of 45° to the object plane and satisfy the Scheimpflug condition. The flow was seeded with neutrally buoyant 10 μm-diameter hollow glass spheres (SpheriCell). The cameras are placed in the forward scattering configuration. The flow is illuminated by a dual-cavity Spectra Physics PIV-200 Nd:YAG laser with a maximum energy of 200 mJ/pulse. To minimise optical distortion of the image, the pipe inside the test section is replaced by a 1.6 mm thick glass tube and two water prisms are placed in front of the test section. The light sheet is perpendicular to the mean flow direction in order to measure the flow patterns associated with streamwise vortices. The light sheet thickness is approximately 1.5 mm. Particle displacements up to 8 px (0.45 mm) return a good correlation signal. The data acquisition system is a commercial system from LaVision.

For the present challenge, a set of 100 records was selected from an experiment in a laminar flow at $Re = 4,600$. This test case is challenging as the laminar flow is not exactly parabolic due to the effect of the Earth's rotation (Draad and Nieuwstadt 1998), so the velocity distribution cannot be fitted by a simple analytical law. Given that the flow is laminar and that the in-plane components (i.e. corresponding with the cross-stream velocity components) are zero, the rms value of the velocity components is a direct indication of the PIV noise, and the deviation of the measured mean cross-stream velocity components are a direct indication of any bias errors in the reconstruction of the three components of the velocity in the measurement plane. A set of images for 5 calibration target positions was provided for positions at $z = -0.50$, $-0.25$, 0.00, 0.25 and 0.50 mm. An example of calibration target image is given in Fig. 44 and a sample of PIV image in Fig. 45.

The first five columns of Table 25 give the list of contributors which did evaluate this test case, together with their main evaluation parameters. The following columns
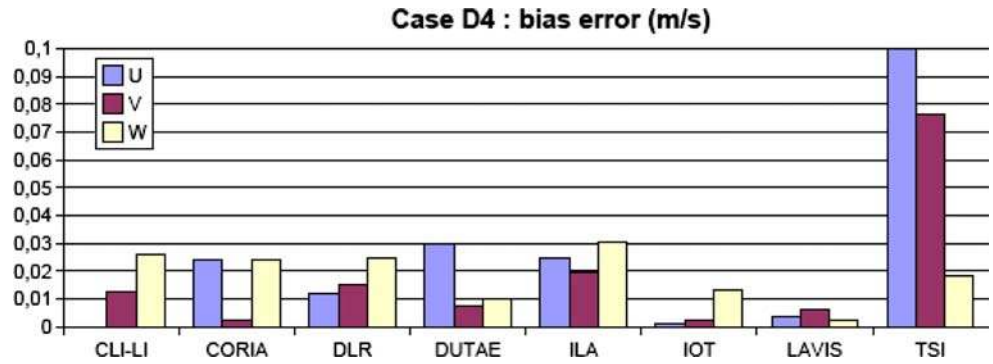
**Fig. 39** Bias error for case D4



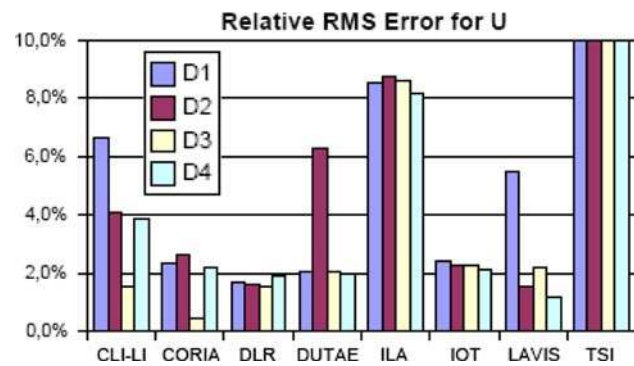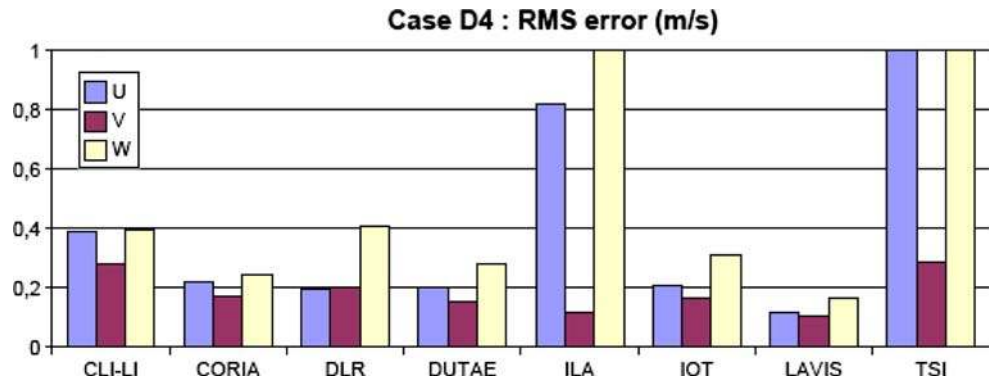**Fig. 40** RMS error for case D4





**Fig. 41** Relative RMS error on the *U* velocity component

give respectively the bulk velocity averaged on the 100 records, the percentage of variation of this bulk velocity through the 100 frames, the maximum velocity and the RMS of the three velocity components as a percentage of the bulk velocity.

As far as the bulk is concerned, the expected value, from the flow rate measurements during the experiment is 0.12 m/s. This complies with most results obtained by the contributors, except for CORIA and KMU. The deviation of their results from the other contributors is most likely due to an erroneous calibration. Figure 46 gives the evolution of the bulk velocity as a function of the record number (i.e. time) as found by the different contributors. The results occur in two groups, i.e. LAVISION, LIMSI,

and IOT find a somewhat higher flow rate than DLR and TSI. The difference between the results from the two groups is about 2%. A clear correlation with the interrogation characteristics given in Table 23 is not present. A plausible explanation seems that these differences occur as a result of using different combinations for the position of the calibration target. Another plausible explanation lies in the measurement of the flow near the pipe wall, as is explained below.

Figures 47 and 48 give the mean streamwise and radial velocity profiles respectively along the vertical axis. It is clear from these figures that the CORIA and KMU results deviate as a consequence of an erroneous calibration. For the other results, the global shape of the streamwise velocity and the zero value of the radial velocity are fairly well retrieved. Note that close to the pipe wall, LAVISION and DLR appear to obtain incorrect results (i.e. to the left the LAVISION data drops to zero before the location of the pipe wall whereas to the right the DLR data appears to show a change in slope when the data approach the wall). Since the near wall data make a significant contribution to the total flow rate, it is possible that small errors cause part of the deviations shown in Fig. 46. However, this does not seem consistent with the other data.

Figure 49 compares the mean secondary velocity components obtained by DLR and Lavision. First, a clear peak locking is visible in both results, despite the fact that these two contributors use advanced window deformation
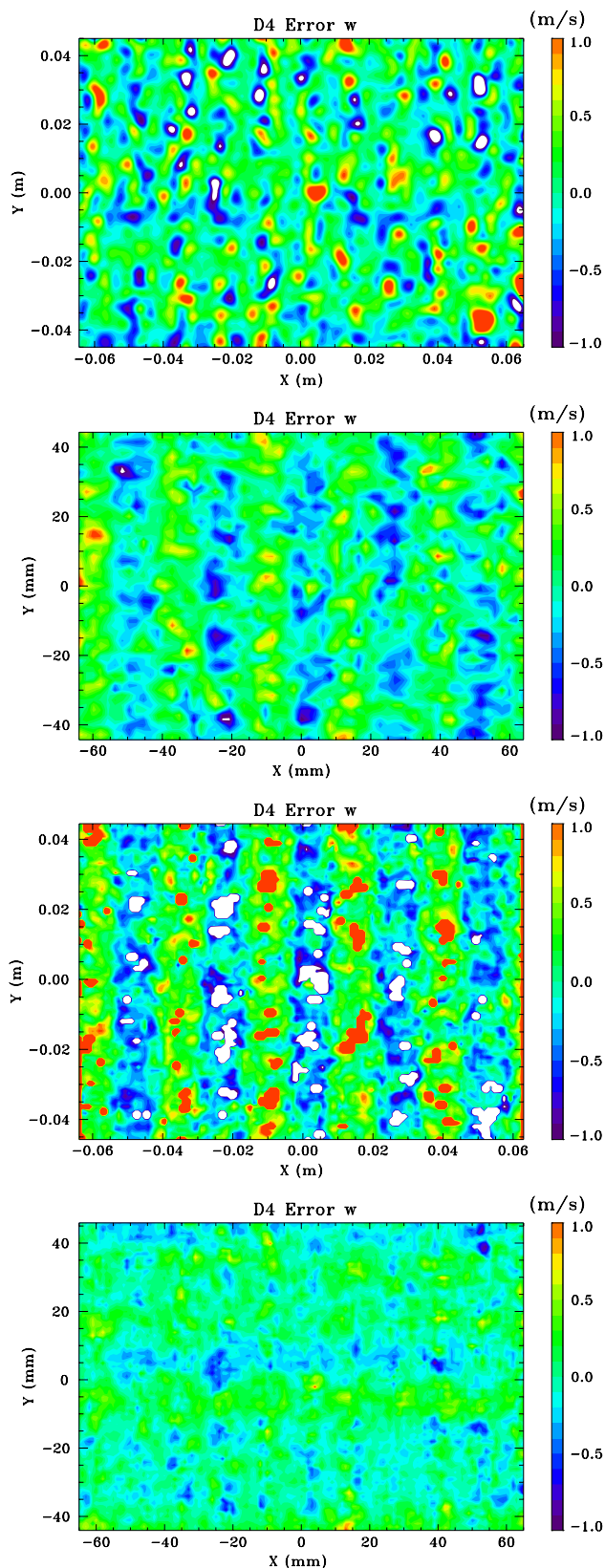
Fig. 42 Reconstructed out of plane component w for case D4, by 4 contributors: **a** CLIPS/LIMSI , **b** IOT, **c** TSI, **d** DLR

multigrid and multipass algorithms. Both results clearly show that the position of the maximum velocity is off-center as a result of a Coriolis force acting on the pipe flow. The position of this maximum is consistent between these two results.

Given that the flow is laminar, the expected value for the rms velocity fluctuations is zero for all three velocity components. Hence, the value of the measured rms fluctuations is a measure for the rms random noise in the PIV results. In Fig. 50 is plotted the profile of rms fluctuation for the measured streamwise component Uz along the vertical axis. The average over all data is given in Table 23. Figure 50 confirms that the deviation of the CORIA data is linked to the stereo calibration as the noise level is comparable to that of the others. Lavision appears to have a higher noise level on the right side of the field, while DLR obtains a good overall result. This is most likely thanks to the image preprocessing applied by DLR. Table 23 shows that most contributors show rms noise amplitudes in the range between 2 and 3% of the bulk velocity, with a good homogeneity over the three components, with the component that is redundant in the stereoscopic reconstruction (here the vertical component, i.e. V) showing a slightly smaller rms noise error. This is in good agreement with the results of case D, see Tables 23 and 24 for comparison.

As a conclusion for this case, it appears that only two contributors were not able to obtain a proper calibration, which may have been due to the fact that some of the information on the position of the calibration target or orientation of the light sheet in relation to the camera positions was unclear. For the others, the small but significant differences can be attributed to problems in resolving the fluid motion close to the pipe wall, where reflections and fixed particle images that are not located in the light sheet compromise the interrogation. It appears that a properly applied image pre-processing can reduce these problems. This probably explains too low values for the rms noise in the results obtained by DLR. Overall, the results for the rms noise error appear in agreement with the results obtained for the synthetic PIV images of case D. The RMS error of 2% of the mean absolute velocity corresponds more or less to an absolute error of 0.1 px in the PIV evaluation. This means that the stereoscopic calibration and reconstruction, if done properly, does not significantly increase the RMS error (for a stereoscopic PIV system with a 90-degree angle between the optical axes of the cameras).

## 9 Conclusion

Following the conclusions from the first two editions, this third PIV challenge had three main objectives:
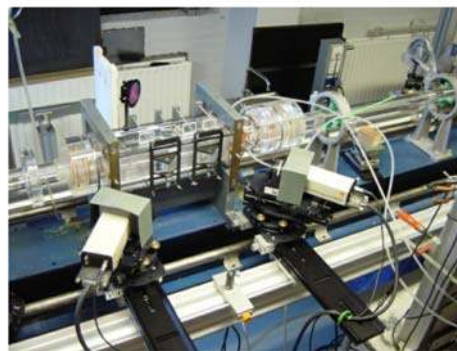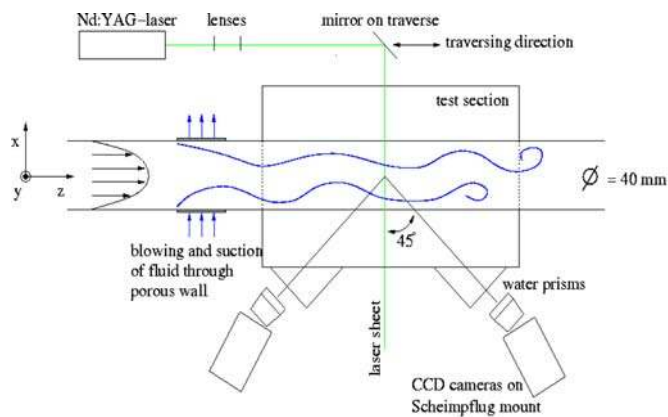
**Fig. 43** Scheme and photograph of the experimental set-up used to record Stereo PIV images for case D. The flow is inside a transparent circular pipe. The light sheet is normal to the pipe axis. A

parallelepipedic casing and prisms are used to limit image aberrations. The two cameras are set in Sheimpflug conditions, in forward scatter, on both sides of the light sheet
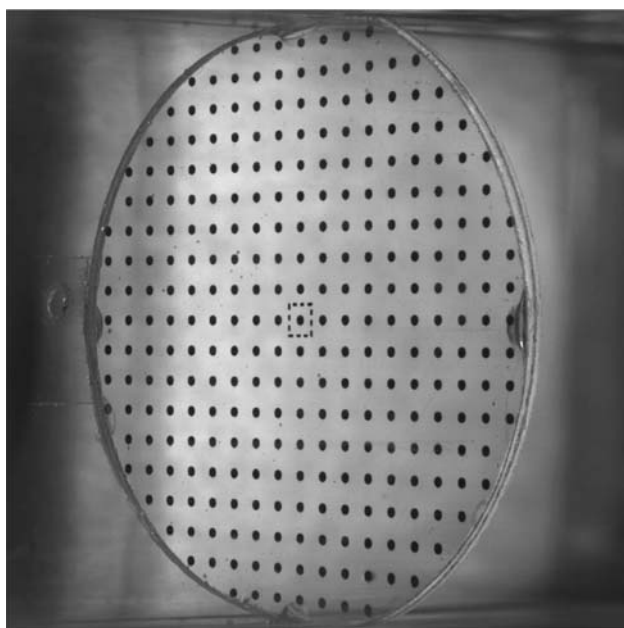


**Fig. 44** Image of the calibration target recorded by the left camera



**Fig. 45** Representative sample of PIV image recorded by the left camera

- to assess the spatial resolution reached by the different PIV and PTV algorithms available,
- to evaluate the improvements brought by advanced algorithms for time resolved PIV in terms of dynamic range,
- to characterize the accuracy of stereo PIV algorithms.

For that purpose, five different test cases were set-up and proposed to a total of 23 different contributors from all around the world. It should be emphasized, that all these contributors, who did participate on a voluntary basis, did bring most of the existing approaches to PIV image processing, together with the major PIV providers software.

As far as the spatial resolution is concerned, four different test cases where proposed to the contributors. Cases
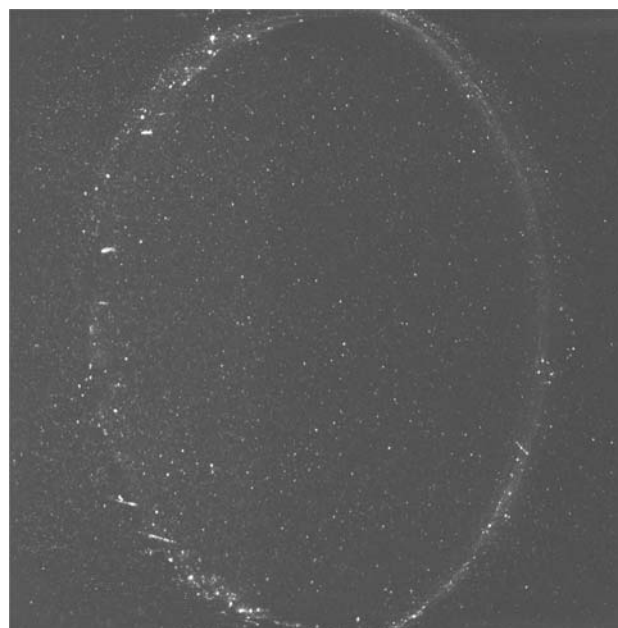
A1 to A3 allowed to characterize the spatial spectral response of the algorithms, while case A4 was designed as a single image spatial resolution test by Scarano and Wieneke.

Case A1, with a flat spectrum, did evidence the robustness of the PIV algorithms for the extraction of the mean velocity. It also did show the limits as far as the fluctuations inside the interrogation window are concerned. Case A2, with a strong slope (−3) was a real challenge. The amplitude of the signal decreasing very rapidly with increasing wave number, small differences in the noise level introduced by the algorithms affected directly the spatial resolution. About one order of magnitude difference
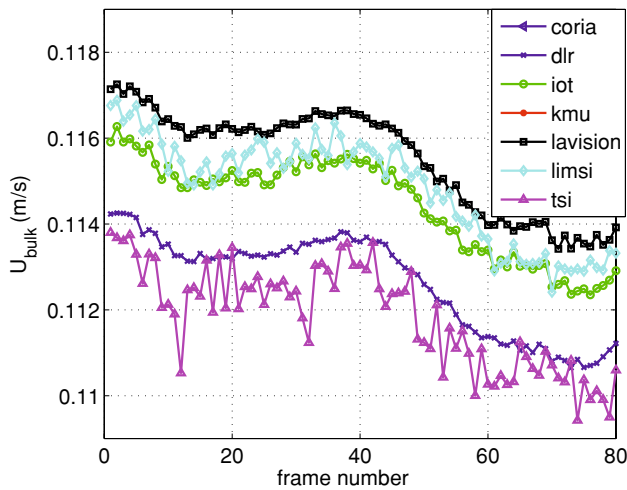
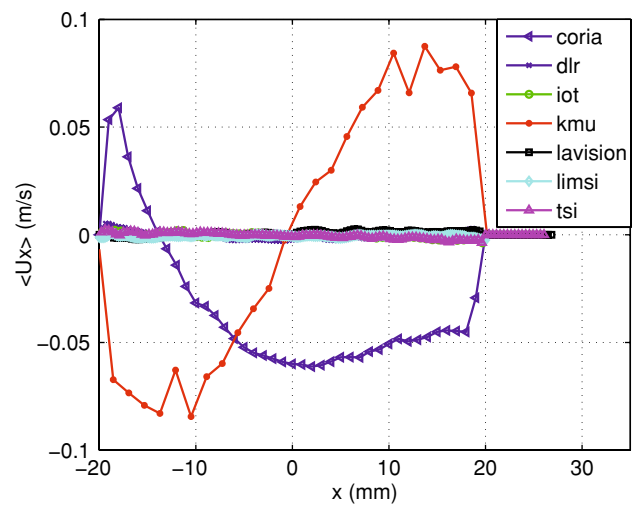**Fig. 46** Flow rate velocity as a function of time obtained by the different contributors



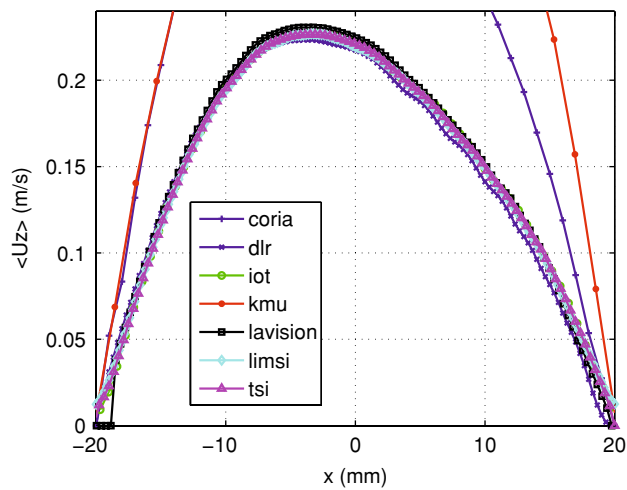**Fig. 48** Mean radial velocity profile $Ux(x)$ along the vertical axis



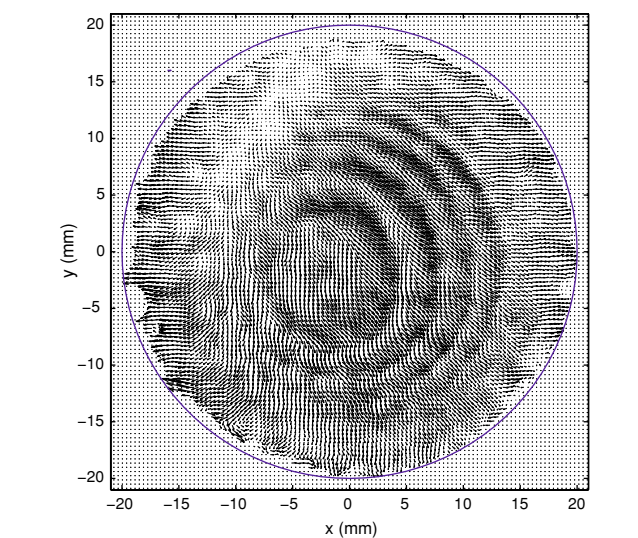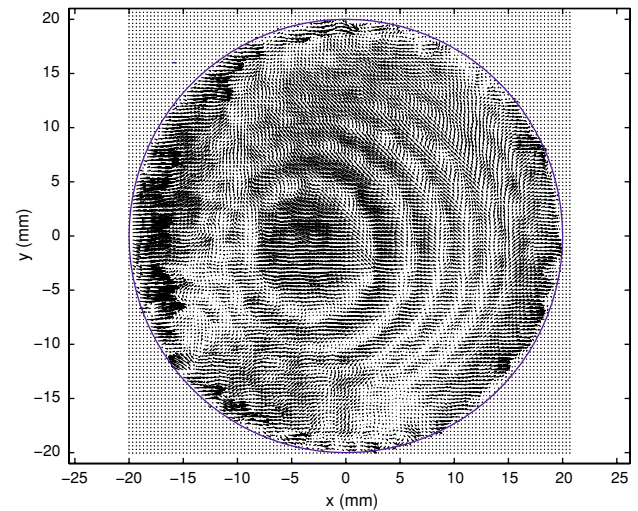**Fig. 47** Mean streamwise velocity profile $Uz(x)$ along the vertical axis



is observed on the scales resolved between the extreme contributions, corresponding to about three orders of magnitude in energy. Case A3 was aimed at testing the algorithms near the limit of the present spatial resolution of PIV. A clear advantage is given to the advanced algorithms using multi-pass, multi-grid and image deformation strategies. An important point which came out is that most of the teams using these algorithms apply some filtering of high frequency noise. Obviously, further investigation is needed to define the best strategy in that matter.

Case A4 has shown the interest of having a single image synthetic test allowing to evaluate the performances of interrogation techniques in terms of spatial resolution and accuracy. The spatial resolution of the different interrogation methods has been evidenced both qualitatively and quantitatively. Again, the algorithms performing iterative
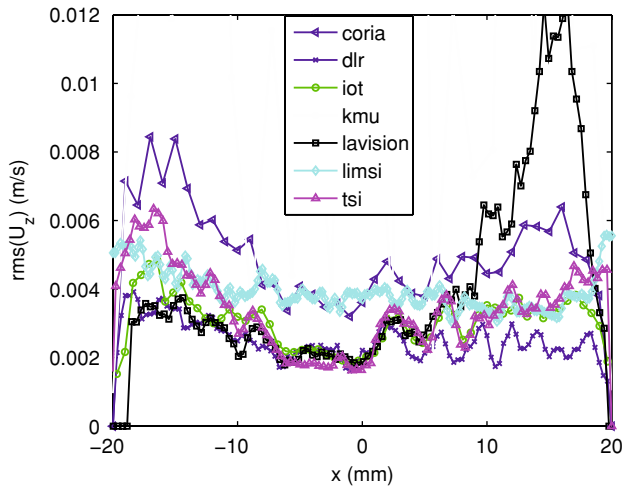
**Fig. 49** Mean secondary velocity components $Ux(x,y)$ and $Uy(x,y)$ obtained by DLR (*top*) and Lavision (*bottom*)

**Fig. 50** Profile of the rms value of the streamwise velocity $Uz$ along the vertical axis

image deformation did show the highest performances (CORIA, DLR, DUTAE, LAVIS, PURDUE, UDN). Spatial resolution was down to about 25 px for 1D fluctuations and about 30 px for 2D fluctuations.

A clear conclusion could be made concerning the different types of approaches.

Different groups around the world are working with correlation PIV for many years now and the theory is fairly established. This leads the advanced multigrid, multipass, image deformation software to provide the best results in this challenge. But, obviously, not one algorithm does yet the best on all test cases. The skill of the user, the pre-processing selected, the filters applied in the course of the iterations play a significant role, which vary, depending on the test case.

For optical flow, which is a more recent approach to PIV image analysis, it is still difficult to make a theoretical link between the algorithm and its accuracy. On a pure theoretical basis it is conjectured that this method should be able to do better than correlation in terms of spatial resolution. The present results show that this is not the case. At best, the optical flow results compare with an intermediate correlation algorithm. Some further theoretical work is obviously needed on this approach to clearly link the values of its parameters to the image characteristics.

Finally, on all the A test cases, the results of PTV are fairly disappointing. Although care was taken to make the comparison as good and as fair as possible, the noise level is higher and the spatial resolution is less than provided by the best correlation tools. For the sake of equity, it should be noted that the test cases were optimised for correlation PIV in terms of particle image size and concentration. This is surely not favourable for PTV. Decreasing the seeding and increasing the particle image size would probably

**Table 24** Mean and RMS velocity, bias and RMS error for case D4

| Contributors | Velocity | | | | | | Error | | | | | | | | |
| | U | | V | | W | | U | | | V | | | W | | |
| | Mean | RMS | Mean | RMS | Mean | RMS | Bias | RMS Absolute | Relative (%) | Bias | RMS Absolute | Relative (%) | Bias | RMS Absolute | Relative (%) |
| --- | --- | --- | --- | --- | --- | --- | --- | --- | --- | --- | --- | --- | --- | --- | --- |
| Reference | 10.0047 | 0.1450 | −0.1277 | 0.4159 | −0.0577 | 2.7807 | | | | | | | | | |
| CLI-LI | 10.0004 | 0.4388 | 0.1002 | 0.5223 | −0.0303 | 2.8640 | −0.0030 | 0.4077 | 4.1 | −0.0260 | 0.3062 | 30.6 | 0.0236 | 0.4338 | 10.8 |
| CORIA | 10.0046 | 0.3100 | −0.0920 | 0.4420 | −0.0566 | 2.9080 | 0.0000 | 0.2625 | 2.6 | 0.0307 | 0.1637 | 16.4 | −0.0240 | 0.2769 | 6.9 |
| DLR | 10.0466 | 0.2203 | −0.0982 | 0.4342 | −0.0503 | 2.7808 | 0.0424 | 0.1613 | 1.6 | 0.0290 | 0.1382 | 13.8 | −0.0019 | 0.3324 | 8.3 |
| DUTAE | 10.0020 | 0.6510 | −0.1323 | 0.3370 | 0.0662 | 2.8120 | −0.0010 | 0.6258 | 6.3 | 0.0006 | 0.1651 | 16.5 | 0.0006 | 0.1651 | 4.1 |
| ILA | 10.0428 | 0.8733 | −0.1087 | 0.3853 | −0.1079 | 2.5181 | 0.0418 | 0.8754 | 8.8 | 0.0208 | 0.1218 | 12.2 | −0.0841 | 1.6872 | 42.2 |
| IOT | 9.9970 | 0.2655 | −0.1016 | 0.4613 | −0.0839 | 2.5990 | −0.0060 | 0.2265 | 2.3 | 0.0245 | 0.1540 | 15.4 | −0.0154 | 0.3335 | 8.3 |
| LAVIS | 10.0020 | 0.2154 | −0.1172 | 0.4299 | −0.0547 | 2.7722 | −0.0004 | 0.1538 | 1.5 | 0.0027 | 0.1805 | 18.0 | −0.0006 | 0.1530 | 3.8 |
| TSI | 9.2554 | 2.6960 | −0.0708 | 0.4238 | −0.0234 | 2.4200 | −0.5926 | 2.4304 | 24.3 | 0.0589 | 0.1731 | 17.3 | 0.0247 | 0.9415 | 23.5 |

D2

**Table 25** Result of the analysis of case E by the different contributors

|  | M × N | IA (px) | Ovrlp (%) | Outl (%) | Ub (m/s) | Fluct (%) | 'U' max (m/s) | rmsU (%Ub) | rmsV (%Ub) | rmsW (%Ub) |
|---|---|---|---|---|---|---|---|---|---|---|
| CORIA | 41 × 41 | 16 | 75 | 0.5 | 0.1980 | 4.30 | 0.3943 | 2.7 | 1.6 | 2.4[a] |
| DLR | 123 × 123 | 32 | 75 | 0.06 | 0.1126 | 1.00 | 0.2245 | 2.0 | 1.7 | 2.2 |
| IOT | 62 × 62 | 32 | 50 | 1.4 | 0.1145 | 1.00 | 0.2282 | 2.4 | 1.2 | 2.6 |
| KMU | 32 × 32 | – | – | – | 0.2207 | 0.60 | 0.4200 | 8.3 | 3.9 | 8.3[b] |
| LAV | 146 × 146 | 32 | 75 | 8.5 | 0.1155 | 1.00 | 0.2321 | 2.0 | 1.7 | 3.2 |
| LIMSI | 201 × 201 | 8 | 50 | 0.0 | 0.1149 | 1.06 | 0.2286 | 3.4 | 2.9 | 3.4 |
| TSI | 138 × 91 | 32 | 75 | 1.6 | 0.1119 | 1.06 | 0.2279 | 2.7 | 1.3 | 3.1 |
| ILA[c] | | | | | | | | | | |

[a] Uz factor 2 wrong/large cross-flow

[b] Uz factor 2 wrong/misregistration/spurious vectors not detected

[c] Only 1 file provided; not taken into consideration

improve the PTV results. This would imply a specific study as there is no theory providing the optimal parameters as in correlation PIV.

As a global conclusion in terms of a compromise on spatial resolution and accuracy, the following recommendations can be formulated:

- Pre-processing of PIV images to remove as much background noise as possible is recommended. This is case dependent, but can usually be done by computing a mean or a minimum image from a few hundreds of real records and subtracting it from the instantaneous images.
- Advanced multipass, multigrid algorithms with image deformation such as those used by DUTAE, UDN, DLR, CORIA and Lavision are recommended, but, care should be taken to the internal filters used and preliminary calibration of the procedure on synthetic images or equivalent images with known output is recommended (see for example http://www.pivchallenge.org).
- It is at present useless to go lower than 16 × 16 interrogation windows and this should be done only on high quality PIV images.

Case B1 did show the sensitivity of the different algorithms to the signal to noise ratio. The effect on the accuracy is quite strong. On average, the PIV and OF algorithms lead to more accurate evaluations compared to the PTV algorithms for all SNR. However, one problem of the PTV algorithm was found to be the large number of spurious vectors which can be reduced by applying better post-processing methods. The best results could be achieved by means of the evaluation approaches of DLR, DUTAE, YATS and LAVIS.

Concerning the time resolved algorithms, test case B2 did clearly evidence a benefit in using the time information provided by time resolved PIV records. A clever use of this information, as done for example by DLR, DUTAE and

Lavision, allows a significant improvement in dynamic range of the method. Nevertheless, one should keep in mind that this conclusion is drawn from synthetic PIV images. A confirmation with some real images is outlined in Hain and Kähler (2007). This was not possible with test case C.

Test Cases D and E were designed to assess the stereo PIV accuracy and sensitivity to misalignments. The conclusions are quite positive. They agree well between synthetic images from case D and real images from case E. They stand for standard recording conditions, that is a symmetric set-up with angles of the order of 45°, scheimpflug conditions and a magnification of the order of 1/10, corresponding to fields of view of the order of 10 × 10 cm². In these conditions, an accuracy of the order of 2% of the modulus of the velocity can be reached. This accuracy is comparable on the three velocity component. This result is independent of the PIV algorithm used but also of the stereo-reconstruction method employed (image mapping, vector warping, Soloff or pin hole). Again, advanced algorithms, using image deformation seem to bring a slight improvement in the quality of the results. The reconstruction, if properly calibrated does not appear sensitive to slight misalignments of the recording set-up.

Here again, some recommendations can be done for the best use of stereo PIV data:

- The optimisation of both the PIV processing algorithm and the stereo calibration are mandatory.
- The use of advanced PIV processing algorithms is recommended.
- Calibration corrections based on disparity maps are mandatory.

Based on these recommendations, the stereo reconstruction does not bring visible additional errors and the accuracy of the PIV processing algorithm can be retrieved on the three components of the velocity vector.

As can be seen from the above, several interesting and constructive conclusions could be drawn from the present challenge. This is mostly due to the strong involvement of the contributing teams which accepted to spend some time processing the proposed test cases. These contributors should be warmly acknowledged here. At the end of the workshop, in Pasadena, it was concluded that, although a few tracks of improvement were seen, the PIV processing in the present state of the art was fairly well characterised and that a few years have to be waited before setting up a new challenge. Significant improvements and/or break-through had to appear to justify the time and money spent. It was thus decided to suspend the Challenge for some years. Again the organisers would like to thank all the contributors who did participate, in a very fair way to the three Challenges, contributing definitely to their success.

## References

Astarita T (2006) Analysis of interpolation schemes for image deformation methods in PIV: effect of noise on the accuracy and spatial resolution. Exp Fluids 40:977–987

Astarita T, Cardone G (2005) Analysis of interpolation schemes for image deformation methods in PIV. Exp Fluids 38:233–243

Corpetti T, Ménin E, Pérez P (2002) Dense estimation of fluid flows. IEEE Trans Pattern Anal Mach Intel24(3):365–380

Corpetti T, Heitz D, Arroyo G, Ménin E, Santa-Cruz A (2006) Fluid experimental flow estimation based on an optical flow scheme. Exp Fluids 40:80–97

David L, Dupré JC, Valle V, Robin E, Koudeir M, Brochard J, Jarny S, Calluaud D (2005) Comparison of three techniques to localize and to measure 3D surfaces. In: 6th International symposium on particle image velocimetry, Pasadena (USA)

Di Florio D, Di Felice F, Romano (2002) G. P. Windowing, re-shaping and re-orientation interrogation windows in particle image velocimetry for the investigation of shear flows. Meas Sci Technol 13:953–962

Doh DH, Kim DH, Cho KR, Cho YB, Saga T, Kobayashi SK (2002) Development of genetic algorithm based 3D-PTV technique. J Vis 5(3):243–254

van Doorne CWH, Westerweel J (2007) Measurement of laminar, transitional and turbulent pipe flow using stereoscopic-PIV. Exp Fluids 42:259–279

Draad AA, Nieuwstadt FTM (1998) The Earth's rotation and laminar pipe flow. J Fluid Mech 361:297–308

Hain R, Kähler CJ (2007) Fundamentals of multiframe particle image velocimetry (PIV). Exp Fluids 42:575–587

Hain R, Kähler CJ, Tropea C (2007) Comparison of CCD, CMOS and intensified cameras. Exp Fluids 42:403–411

Horn B, Schunck B (1981) Determining optical flow. Artif Intel 17:185–203

Kähler CJ, Kompenhans J (2000) Fundamentals of multiple plane stereo particle image velocimetry. Exp Fluids 29:S70–S77

Kähler CJ, Sammler B, Kompenhans J (2002) Generation and control of particle size distributions for optical velocity measurement techniques in fluid mechanics. Exp Fluids 33:736–742

Keane RD, Adrian RJ (1992) Theory of cross-correlation analysis of PIV images. Appl Sci Res 49:191–215

Laval J-P, McWilliams J-C, Dubrulle B (2003) Forced stratified turbulence: successive transitions with Reynolds number. Phys Rev E 68:036308

Lecordier B, Trinité M (2004) Advanced PIV algorithms with image distortion for velocity measurements in turbulent flows. In: Stanislas M, Westerweel J, Kompenhans J (eds) Proceedings of the EUROPIV 2 workshop held in Zaragoza, Spain, March 31– April 1, 2003. Springer, Heidelberg, ISBN 3-540-21423-2

Lecordier B, Westerweel J (2004) The EUROPIV synthetic image generator. In: Stanislas M, Westerweel J, Kompenhans J (eds) Particle image velocimetry: recent improvements. Springer, Heidelberg

Lucas BD, Kanade T (1981) An iterative image registration technique with an application to stereo vision. From Proceedings of imaging understanding workshop, pp 121–130

Lugni C, Brocchini M, Faltinsen OM (2006) Wave impact loads: the role of flip-through. Phys Fluids 18(1) (in press)

Marrazzo M, De Gregorio F, Romano GP (2004) The use of a deformable weight function and of advanced validation proce-dures in PIV. In: 12th International symposium on applications of laser techniques to fluid mechanics, Lisbon

Marxen O, Rist U, Wagner S (2004) The effect of spanwise-modulated disturbances on transition in a 2-D separated bound-ary layer. AIAA J 42:937–944

Miozzi M (2004) Particle Image Velocimetry using feature tracking and Delaunay tessellation. In: Proceedings of the 12th int. symp. on appl. laser tech. to fluid mech., Lisbon

Miozzi M (2005) Direct measurement of velocity gradients in digital images and vorticity evaluation. In: 6th International symposium on particle image velocimetry, Pasadena, September 21–23

Nogueira J, Lecuona A, Rodriguez PA (1997) Data validation, false vectors correction and derived magnitudes calculation on PIV data. Meas Sci Technol 8:1493–1501

Ohmi K, Hang Yu L (2000) Particle tracking velocity with new algorithms. Meas Sci Technol 11:603–616

Okamoto K, Nishio S, Kobayashi T, Saga T, Takehara K (2000a) Evaluation of the 3D-PIV standard images (PIV-STD Project). J Vis 3–2:115–124

Okamoto K, Nishio S, Saga T, Kobayashi T (2000b) Standard images for particle-image velocimetry. Meas Sci Technol 11:685–691

Quénot GM, Pakleza J, Kowalewski TA (1998) Particle image velocimetry with optical flow. Exp Fluids 25–3:177–189

Raffel M, Willert C, Wereley S, Kompenhans J (2007) Particle image velocimetry—a practical guide, 2nd edn. Springer, Heidelberg

Scarano F (2002) Iterative image deformation methods in PIV. Meas Sci Technol 13:R1–R19

Scarano F, Riethmuller M (2000) Advances in Iterative multigrid PIV image processing. Exp Fluids Suppl 29:S51–S60

Scarano F, David L, Bsibsi M, Calluaud D (2005) S-PIV comparative assessment: image dewarping+misalignment correction and pinhole+geometric back projection. Exp Fluids 39:257–266

Schrijer FFJ, Scarano F (2006) On the stabilization and spatial resolution of iterative PIV interrogation. 13th International Symposium on Application of Laser Techniques to Fluid Mechanics, Lisbon, Portugal, 26–29 June, 2006

Soloff SM, Adrian RJ, Liu Z-C (1997) Distortion compensation for generalized stereoscopic particle image velocimetry. Meas Sci Technol 8:1441–1454

Stanislas M, Okamoto K, Kaehler C (2003) Main results of the first international PIV Challenge. Meas Sci Technol 14:R63–R89

Stanislas M, Okamoto K, Kaehler CJ, Westerweel J (2005) Main results of the second international PIV Challenge. Exp Fluids 39:170–191

Stitou A, Riethmuller ML (2001) Extension of PIV to Super Resolution using PTV. Meas Sci Technol 12(9):1398–1403

Wereley ST, Gui LC (2002) Advanced algorithms for microscale Particle Image Velocimetry. AIAA J 40(6):1047–1055

Wernet M (2005) Symmetric phase only filtering: a new paradigm for DPIV data processing. Meas Sci Technol 16:601–618

Westerweel J, Scarano F (2005) A universal detection criterion for the median test. Exp Fluids 39:1096–1100

Willert C (2004) Application potential of advanced PIV algorithms for industrial applications. Pivnet/ERCOFTAC workshop on Particle Image Velocimetry, Lisbon, July 9–10

Willert C (2006) Assessment of camera models for use in planar velocimetry calibration. Exp Fluids 41:135–143